Modeling of Impact Properties of Auxetic Materials – Phase 2

Lei Jiang, Dustin Pearson, Tim Dunbar
Martec Limited

Prepared By:
Martec Limited
400-1800 Brunswick Street
Halifax, Nova Scotia B3J 3J8 Canada

Contractor's Document Number: TR-14-38
Martec Control Number: 13.21007.1102
Contract Project Manager: Lei Jiang, 902-425-5101
PWGSC Contract Number: W7707-135609/001/HAL
CSA: Dr. Jeff Szabo, Defence Scientist, 902-427-3427

Contract Report
DRDC-RDDC-2014-C174
March 2014

Abstract

This report presented work performed in phase 2 of a recent numerical investigation on impact properties of auxetic materials. In this phase of study, efforts were first taken to verify the results of the previous parametric studies. Through these verifications, a set of desired solution control parameters were established and demonstrated to produce reliable numerical solutions. These optimized solution control parameters were then applied in four different parametric studies to characterize the impact properties of the auxetic foam materials in different deformation ranges and under different impacter geometries. Upon completion of the parametric runs, the numerical solutions were first verified to ensure their numerical stability and then post-processed to generate the time histories of the desired physical variables, such as the impact force, the polymer internal energy and the total force transmitted to the substrates. These numerical solutions were found to be consistent with the previous analytical and experimental solutions and provided a good picture of the mechanical responses of these materials to impact loads. By examining these numerical results, some trends were discovered on the impact properties of the auxetic materials as a function of the material type, the unit cell geometry, the void fraction and the impact orientation. These trends provided useful guidelines for selecting auxetic foam materials to achieve optimal protective performance in different applications.

This page intentionally left blank.

Executive summary

Modeling of Impact Properties of Auxetic Materials: Phase 2

L. Jiang; D. Pearson; T. Dunbar; March 2014.

Introduction: Auxetic materials have recently been demonstrated to exhibit some unique characteristics due to their negative Poisson's ratio and provide advantages over conventional engineering materials for certain applications. The objective of the present study was to investigate the impact properties of the auxetic polymer materials and determine the influence of the geometric parameters associated with the auxetic materials on their protective performance against impact loadings.

Results: The present work was an extension of the phase 1 study for this contract. In the present phase, the results of the parametric study performed in the earlier phase were first verified. These verification efforts led to optimal solution control parameters suitable for impact simulations of auxetic materials. These solution control parameters were then successfully applied to perform four different parametric studies to characterize the impact properties of a wide variety of auxetic materials subject to different impact speed and impacter geometry. The numerical solutions were very stable and the predicted material behaviours were consistent with available analytical and experimental solutions. Examination of the results of the parametric studies led to some trends on the performance of the auxetic materials which are useful for selecting materials to achieve optimal protective performance under certain applications.

Significance: A reliable finite element procedure for impact simulations of auxetic polymer foam materials has been developed in this study and verified through extensive numerical calculations. The results of the parametric studies provided a good understanding of the mechanical behaviours of auxetic foam materials under impact loads involving different deformation ranges and patterns. The results also permitted development of trends on the mechanical performance of the materials which will be useful in future structural and/or material optimizations to provide maximum protection to the substrates from impact damages.

Future plans: Although 3D shell elements were utilized throughout the numerical analyses in the present study, the finite element model is 2D in nature because it contains a thin slice of the auxetic material and constraints are applied in the depth direction to enforce a plane-strain like condition. For more accurate analyses, a true 3D model should be utilized.

This page intentionally left blank.

Table of contents

List of figures

List of tables

1 Introduction

Auxetic materials are special materials that have a negative Poisson's ratio. These materials have generated considerable interest in recent years because of their unique mechanical properties and have been demonstrated to provide a number of advantages over the more conventional engineering materials, such as higher indentation resistance, higher fracture toughness and greater resistance to impact damage. These unique features of the auxetic materials make them potential candidates for a variety of applications.

The objective of the present work is to investigate the impact properties of the auxetic materials through finite element-based numerical simulations and thus explore the possibility for using them to provide protection to military structures and personnel. In the first phase of the project completed a year ago [1], an extensive parametric study was performed to investigate the influence of regular and re-entrant honeycomb geometry on the impact properties of the materials. The numerical simulations were performed using LS-DYNA using both shell and solid elements. However, examination of the results suggested that they contained some unanswered questions and further validations of the numerical model were still required.

In the present phase of the contract, a comprehensive verification exercise was first conducted to identify the potential problems in the previous numerical analyses and then determine how these problems could be resolved. The investigations were focused on two areas, namely the contact algorithms and the element formulations. The former required repeated impact simulations of auxetic material samples using different contact options, whereas the latter required solutions of various test problems, ranging from simple beams to single unit cell models taken from a piece of an auxetic material. The goal of these verifications was to identify a set of desired solution control parameters that could produce reliable numerical solutions. The details of these verifications are presented in the next chapter.

These optimized solution control parameters were subsequently utilized in four parametric studies to characterize the impact properties of the conventional and re-entrant polymer foams over different deformation ranges and under different impacter geometries. The first parametric study was a rerun of the parametric study performed on the previous phase, which dealt with material responses up to and beyond the fully compact state under high speed impact from a rigid plate. The second parametric study was focused on the material behaviour under partial compression under rigid planar impacter at a reduced impact speed. The third and fourth parametric studies were concerned with the impact properties of the auxetic materials subjected to local impact from a cylindrical impacter without and with substrates. The results from these parametric studies are presented and discussed in Chapters 3, 4, 5 and 6, respectively.

Conclusions from the present phase of study are presented in Chapter 7.

2 Verifications of the Results of Previous Parametric Study

2.1 Design of parametric study

As described in the previous contract report [1], a parametric study was carried out in Phase I of the present work to investigate the influences of various factors on the impact properties of auxetic materials. The problem setup for this parametric study is shown in Figure 1 which involved a piece of auxetic material resting on a frictionless rigid surface and impacted by a planar impacter with an initial downward velocity of 10 m/s. The top and bottom surfaces of the material specimen were assumed to be in sliding contact with the impacter and the rigid surface, respectively. The vertical edges of the specimen were not constrained, so free expansion or contraction of the sample materials was permitted. To maintain the finite element model size to be manageable, only a thin slice of the sample material, with a depth of 0.1 mm, was included in the analyses and the out-of-plane displacements, u_Y, and rotations, θ_X and θ_Z were constrained at all nodes. These treatments turned the test cases into plane-strain problems.

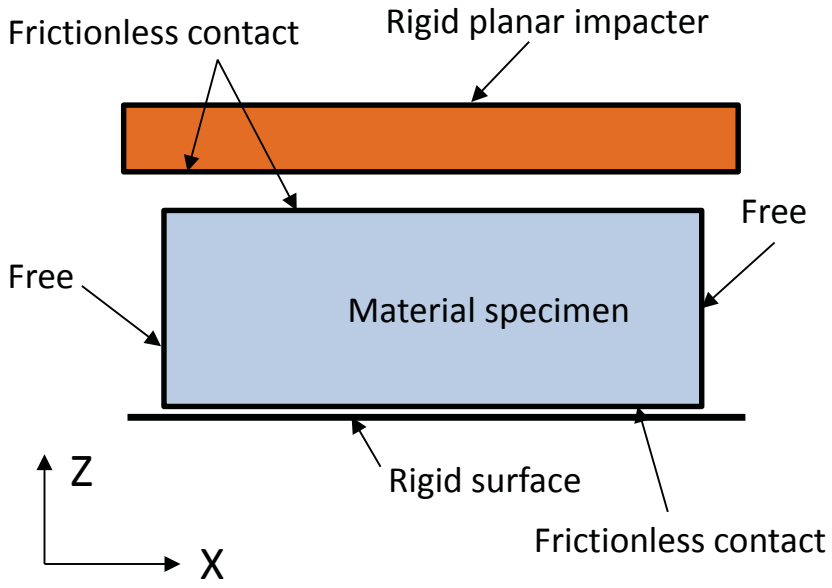

Figure 1: Problem setup for parametric study involving full compression of auxetic materials.

The factors that were considered in the parametric study included angle θ that characterizes the unit cell geometry in re-entrant or conventional honeycomb materials as indicated in Figure 2, the void fraction and the direction of impact. The values taken for these factors for the parametric study are summarized in Table 1. The test matrix contained total of 66 test cases.

Table 1: Test matrix for parametric study

Variables	Values	# of Cases
Angle θ	0^o, $\pm10^o$, $\pm20^o$, $\pm30^o$, $\pm40^o$, $\pm50^o$	11
Void fraction	0.85, 0.70, 0.50	3
Direction of impact	Vertical, Horizontal	2

The outer dimensions of the unit cell in both conventional and re-entrant materials were fixed at L=H=1.0 mm from which the rib lengths and thickness for each test case could be calculated using Equations (5) and (6) given in Reference [1]. In order to make the areal densities of all models similar, different numbers of unit cells were utilized in models for different void fractions. For instance, for models with void fractions of 0.85, 0.7 and 0.5, 16, 8 and 5 unit cells were used in the Z-direction, respectively, resulting in approximately the same areal density of around 2.64 g/cm^2. The number of cells in the X-direction was maintained as 32 for all models, so the width of all the models was approximately 32 mm. The mass of the rigid impacter was taken as about 100 times of the mass of the specimen. In all finite element models, the horizontal ($2h$) and diagonal (l) ribs shown in Figure 2 were idealized by ten and five shell elements, respectively. One element was utilized in the depth direction.

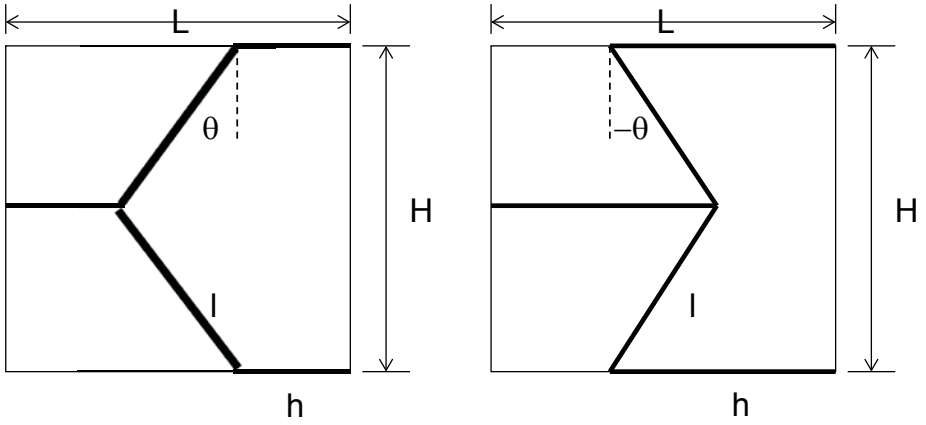

Figure 2: Periodic cells of conventional and re-entrant honeycomb structures.

2.2 Summary of the Previous Results of Parametric Study

The previously predicted deformation processes of a representative honeycomb structure with θ=40^o and void faction of 0.5 under vertical impact are depicted in Figure 3. These results were found to be questionable. This was because if an auxetic material had a void fraction of 0.5, 50% of its original volume was taken by the polymer material. When the material was compressed to half of its original volume, all the voids in the material should have been eliminated and the material became a piece of solid polymer. At this state, the material property should be nearly

incompressible and no significant further volumetric deformations should be expected. However, in the results shown in Figure 3, the deformed volume of the auxetic material sample was clearly less than 50% of the volume of the original configuration. Figures 4 and 5 give representative results on impact force time histories obtained from the parametric study. All these results showed peaks of impact force at the very beginning of the transient followed by nearly zero resistance to the impacter when it moved downward to crush the material. This behavior was not expected either.

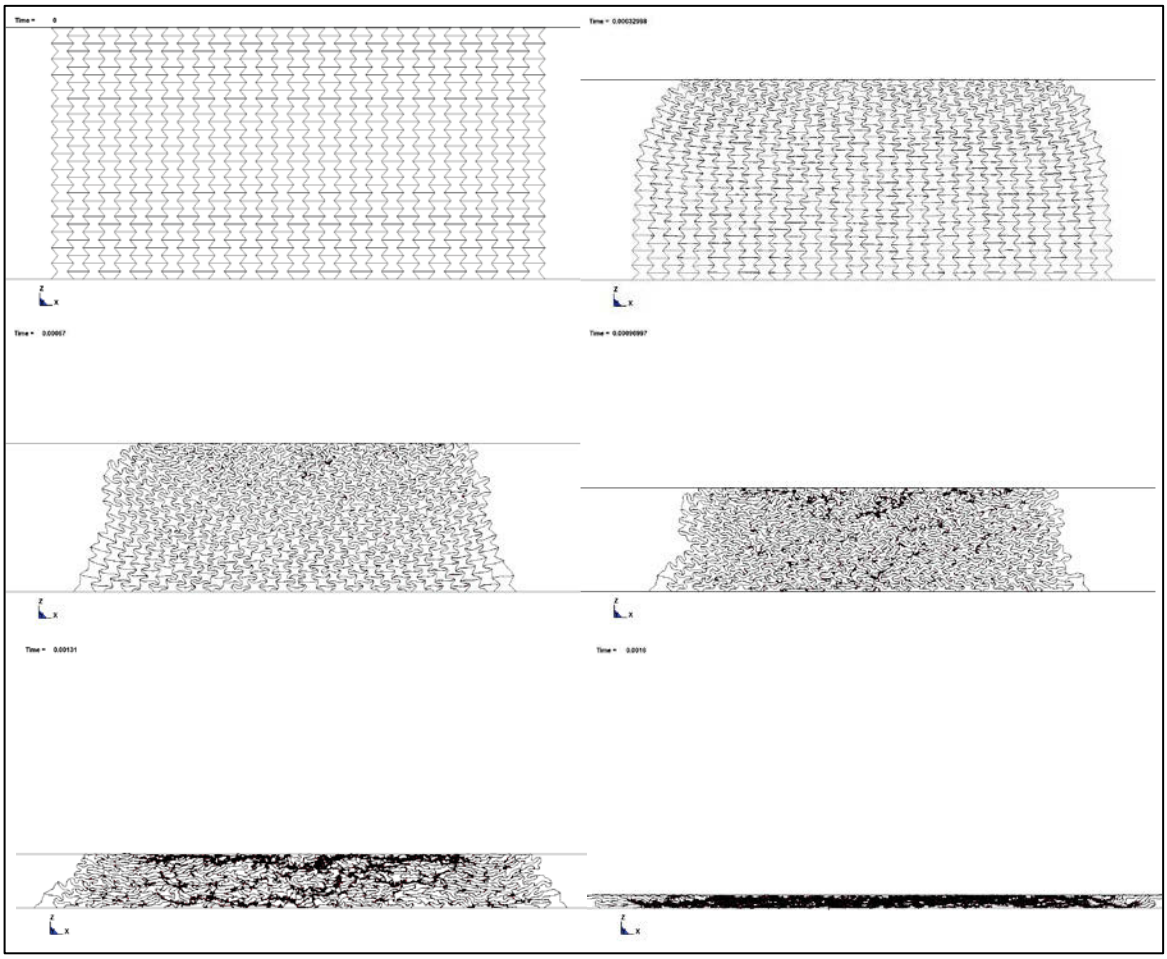

Figure 3: Original and deformed configurations of a re-entrant honeycomb specimen (VF=0.5, $\theta=40^o$) for vertical impact of a planar impacter of 10m/s obtained in Phase I [1].

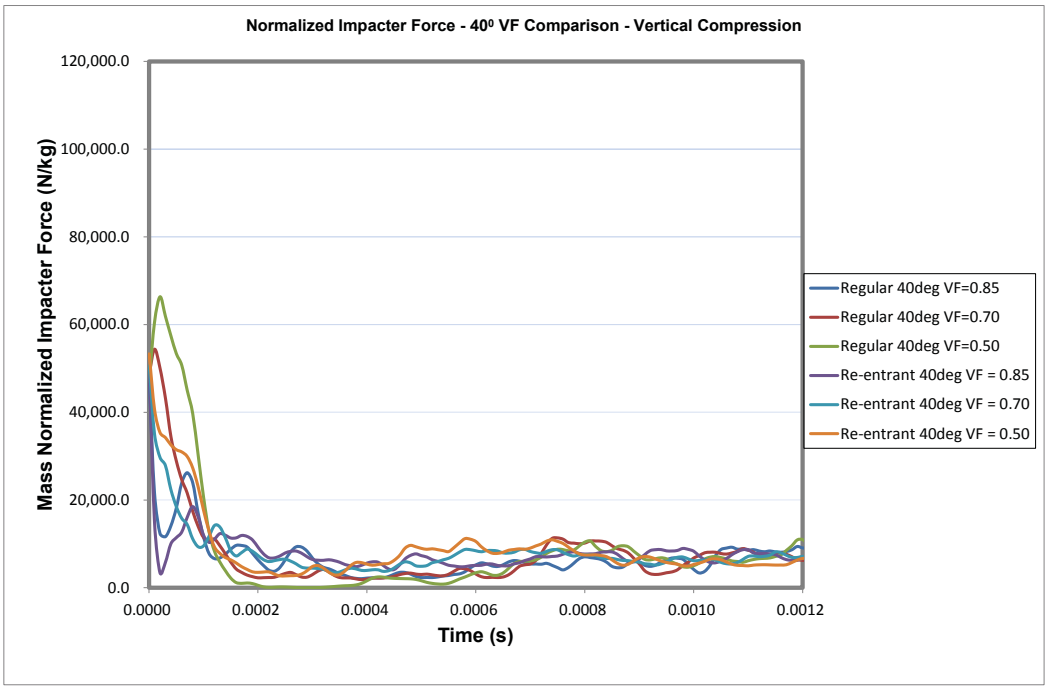

Figure 4: Representative impact force time histories for regular and re-entrant specimens under vertical impact of a planar impacter of 10m/s obtained in Phase I [1].

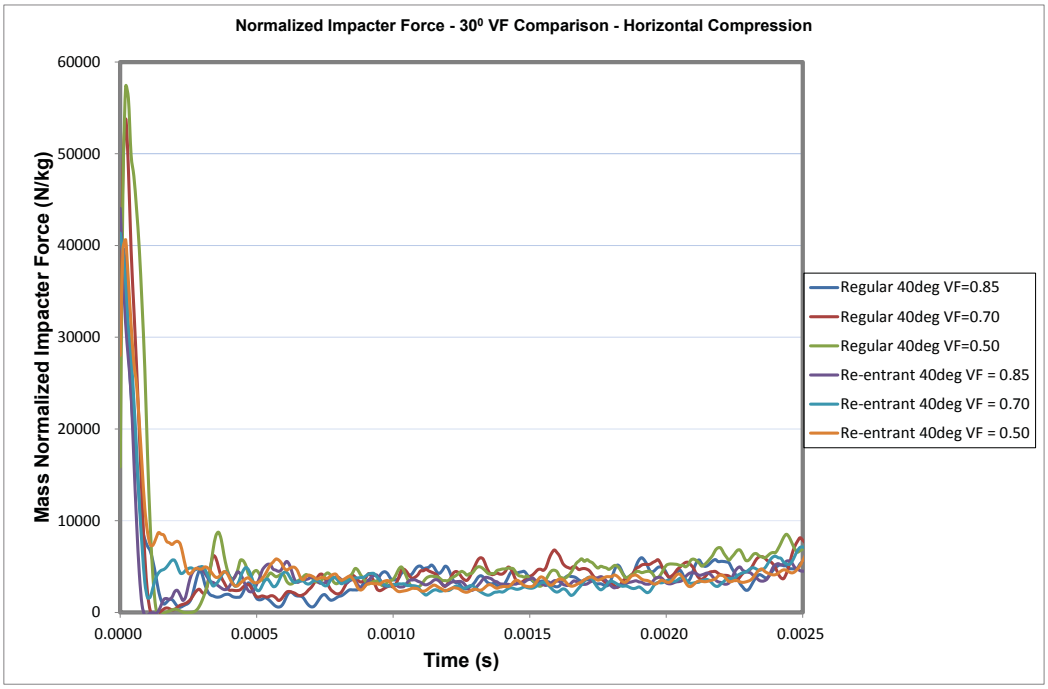

Figure 5: Representative impact force time histories for regular and re-entrant specimens under horizontal impact of a planar impacter of 10m/s obtained in Phase I [1].

2.3 Results of Parametric Study Using Improved Contact Conditions

A close examination of the results indicated that in these impact simulations, very complicated contact conditions occurred in the interior of the auxetic structures when they experienced large deformations. As indicated in Figure 3, under the impact loads, the ribs in honeycomb structures underwent extremely large deformations and the interactions between these highly deformed ribs generated some very difficult contact situations. The doubt on the correctness of the numerical solutions was raised because the volume of the structure was found not to be correctly preserved and in some cases, the impacter and the bottom rigid surface were even in contact at the later stage of simulations. This was obviously non-physical and indicated that the contact conditions between the ribs were not treated properly.

A large number of contact algorithms are provided in LS-DYNA. In the earlier parametric study, option *CONTACT_SINGLE_SURFACE was utilized with SSTHK=1. This combination of contact solution control parameters was supposed to be able to automatically search for the contact surfaces between deformed ribs and the effect of shell thickness should be taken into account. Unfortunately, use of them resulted in highly questionable solutions as mentioned before. To eliminate these defects in the numerical solutions, an alternative contact option, namely *CONTACT_AUTOMATIC_SINGLE_SURFACE, was experimented with. Results from the numerical experiments confirmed that if used along with reduced penalty stiffness, this contact modelling algorithm produced considerably improved solutions.

Using these improved contact options, the contact constraints between the highly deformed ribs were represented more satisfactorily and the overall numerical results looked more reasonable. At this time, the previous parametric study was repeated using the improved contact parameters. Figures were generated from these new results showing time histories of the impact force and internal energy absorption for each case considered in the parametric study. These figures are presented in Figures 6-29.

By reviewing these results, we realized that for all the cases considered, the impact forces were consistently low at the beginning of the transient until the auxetic material became almost fully compact. These results seemed to suggest that the auxetic material provides very little resistance to the impacter before it is compressed into a piece of solid polymer. In order to verify these results, an extensive numerical study was carried out as described in the next section of the report.

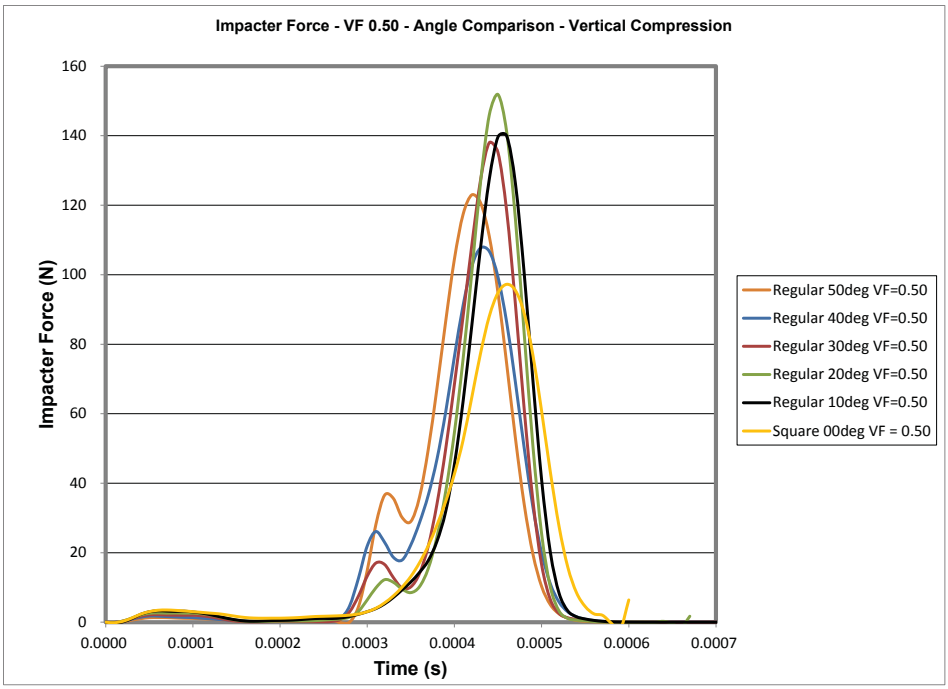

Figure 6: Impact force time histories obtained using the improved contact parameters for vertical impact on regular honeycomb specimens with void fraction of 0.5 and different angles.

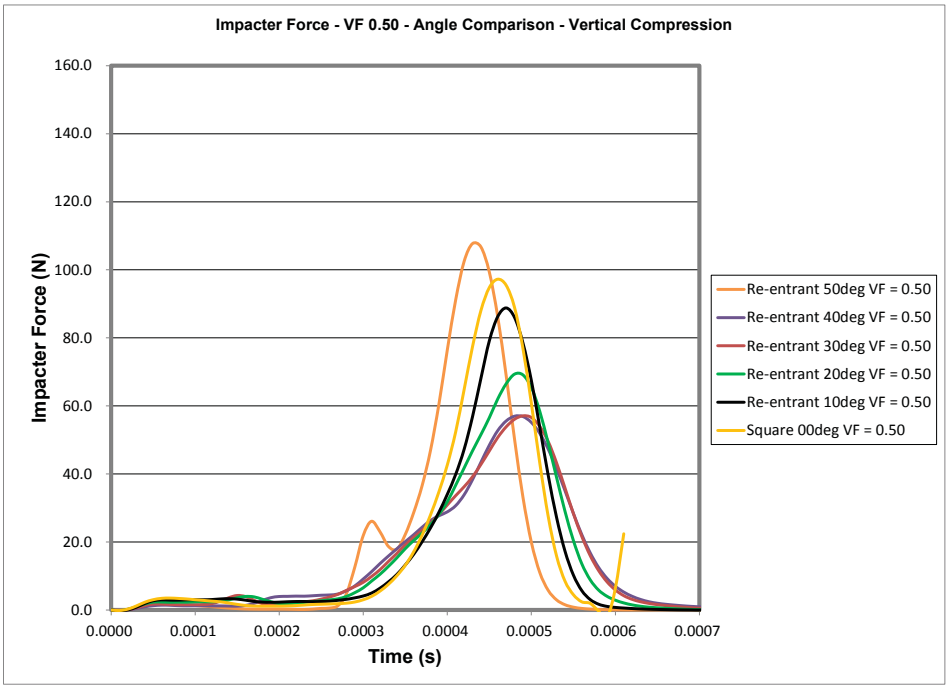

Figure 7: Impact force time histories obtained using the improved contact parameters for vertical impact on re-entrant honeycomb specimens with void fraction of 0.5 and different angles.

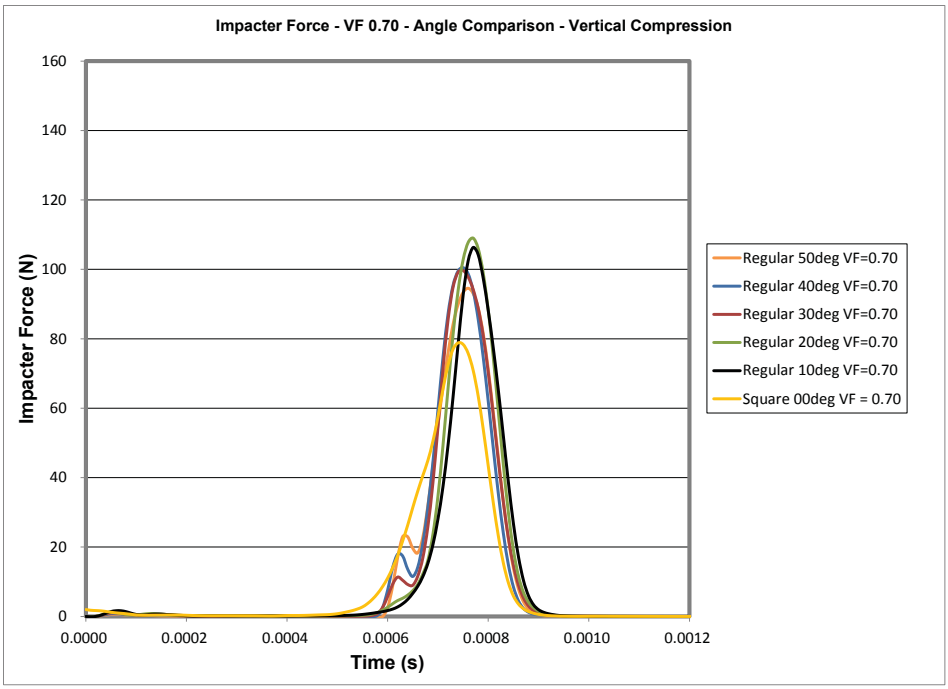

Figure 8: Impact force time histories obtained using the improved contact parameters for vertical impact on regular honeycomb specimens with void fraction of 0.7 and different angles.

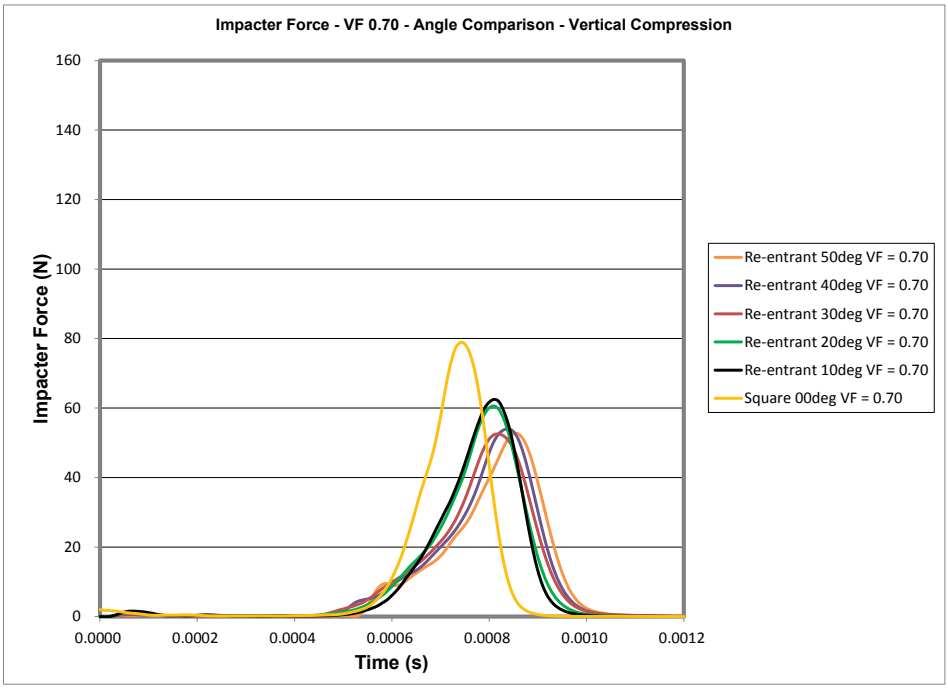

Figure 9: Impact force time histories obtained using the improved contact parameters for vertical impact on re-entrant honeycomb specimens with void fraction of 0.7 and different angles.

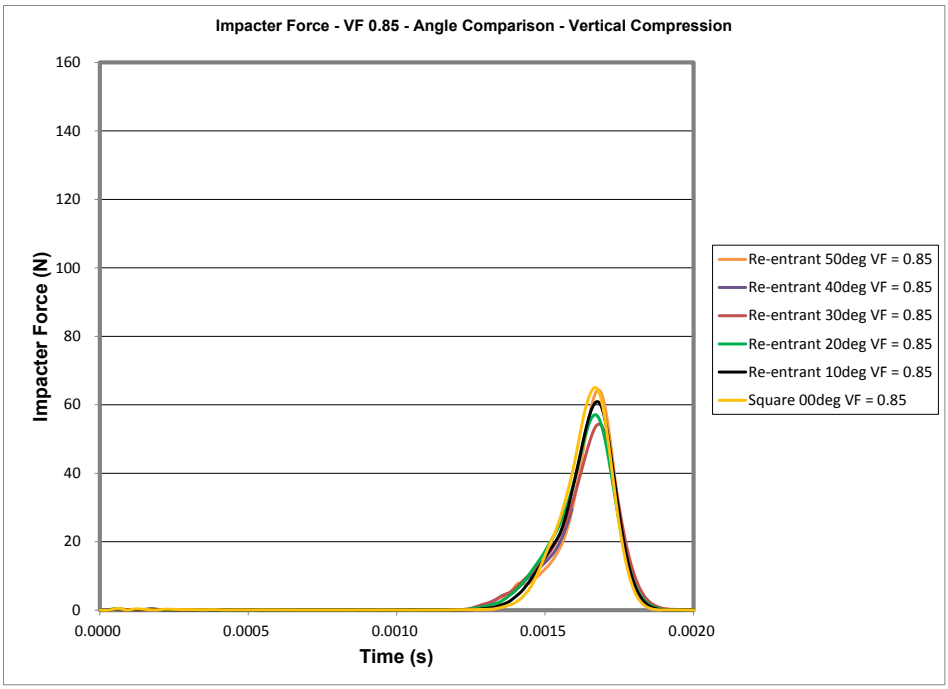

Figure 10: Impact force time histories obtained using the improved contact parameters for vertical impact on regular honeycomb specimens with void fraction of 0.85 and different angles.

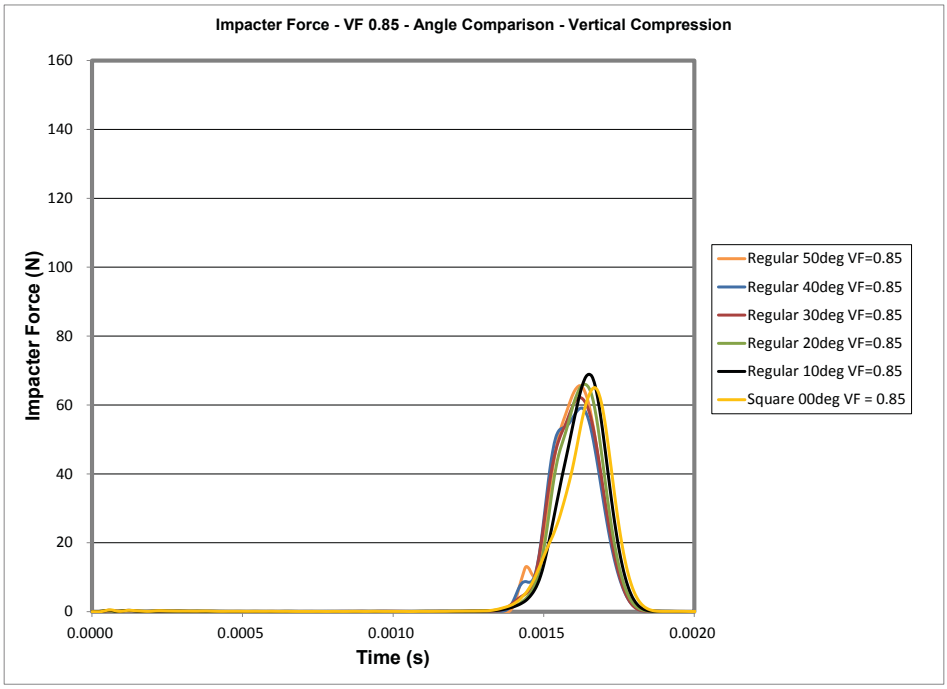

Figure 11: Impact force time histories obtained using the improved contact parameters for vertical impact on re-entrant honeycomb specimens with void fraction of 0.85 and different angles.

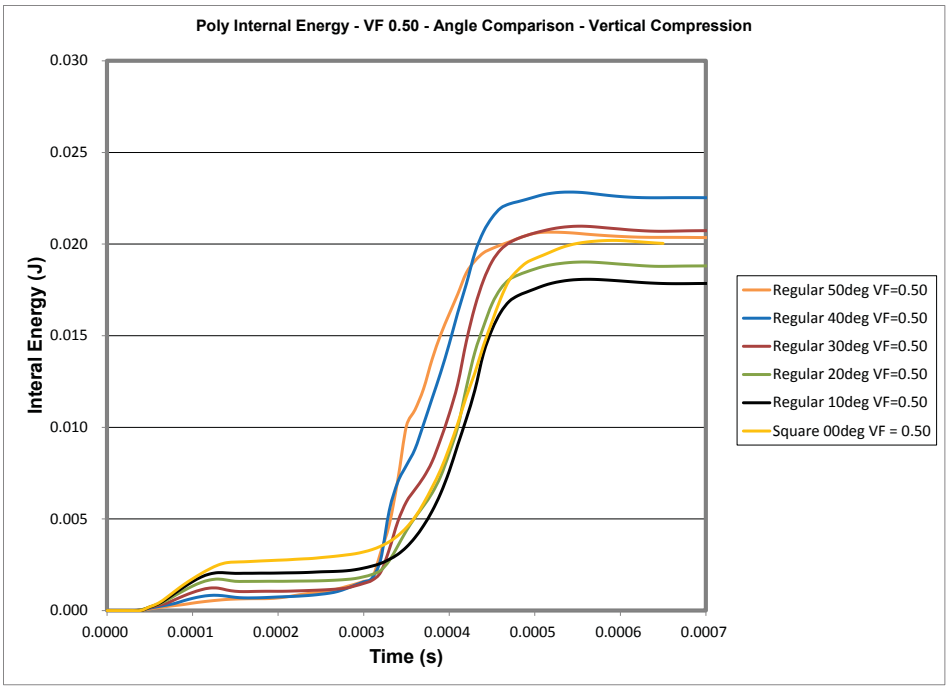

Figure 12: Internal energy time histories obtained using the improved contact parameters for vertical impact on regular honeycomb specimens with void fraction of 0.5 and different angles.

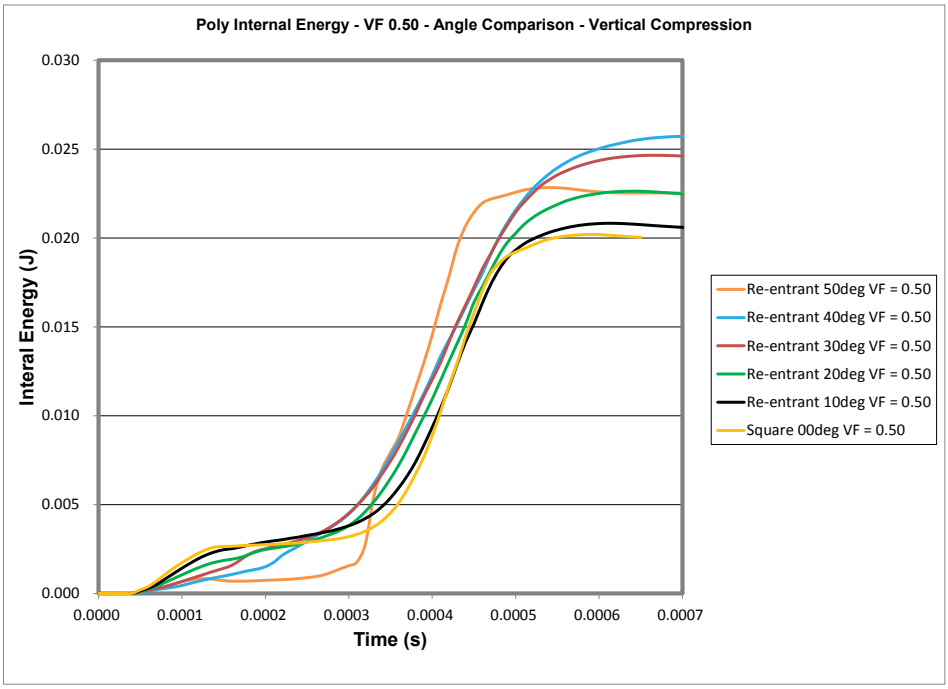

Figure 13: Internal energy time histories obtained using the improved contact parameters for vertical impact on re-entrant honeycomb specimens with void fraction of 0.5 and different angles.

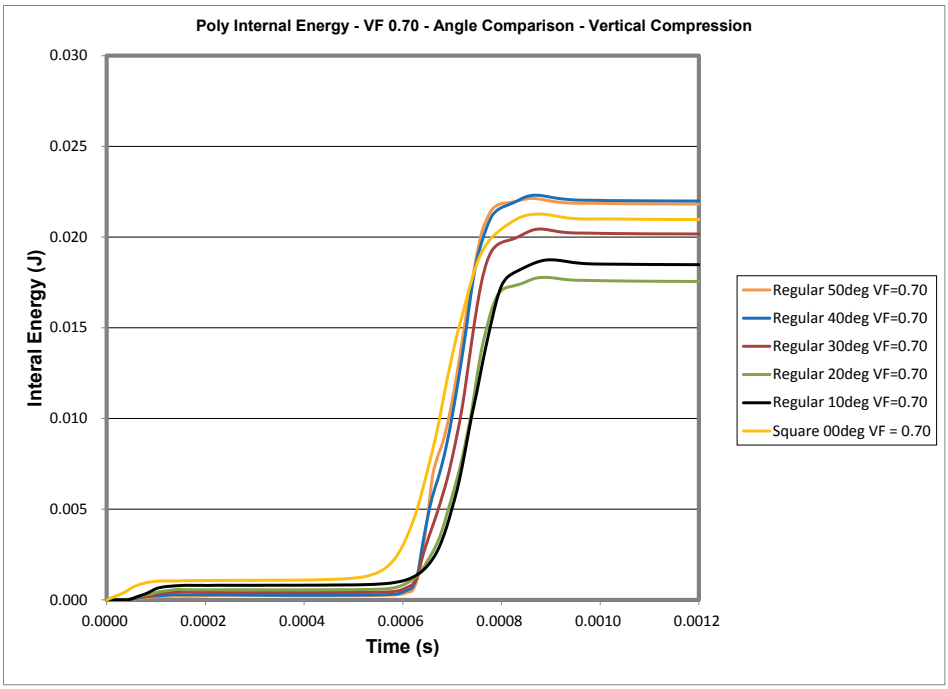

Figure 14: Internal energy time histories obtained using the improved contact parameters for vertical impact on regular honeycomb specimens with void fraction of 0.7 and different angles.

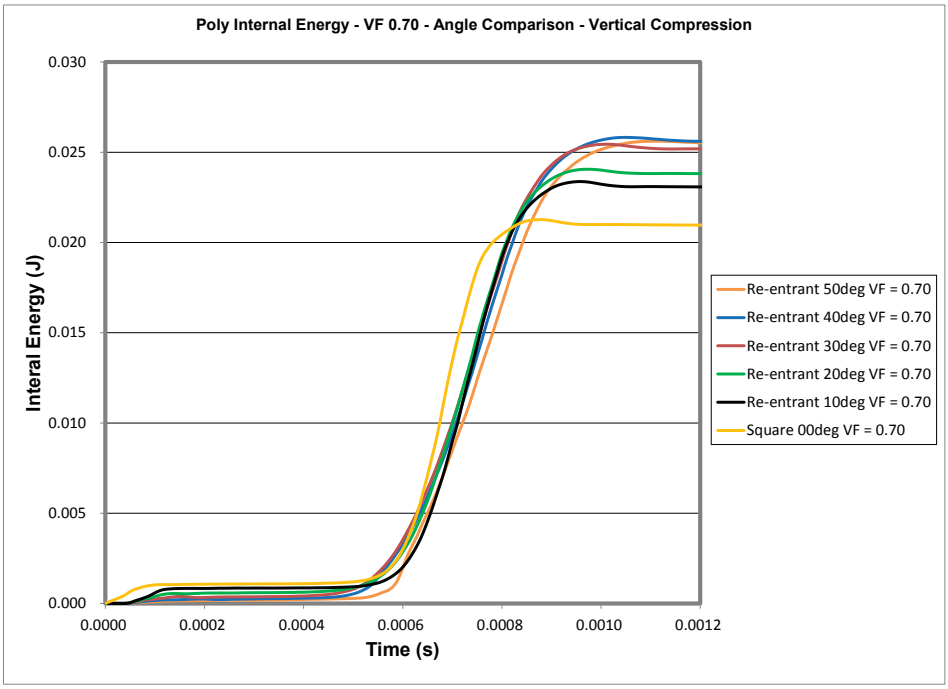

Figure 15: Internal energy time histories obtained using the improved contact parameters for vertical impact on re-entrant honeycomb specimens with void fraction of 0.7 and different angles.

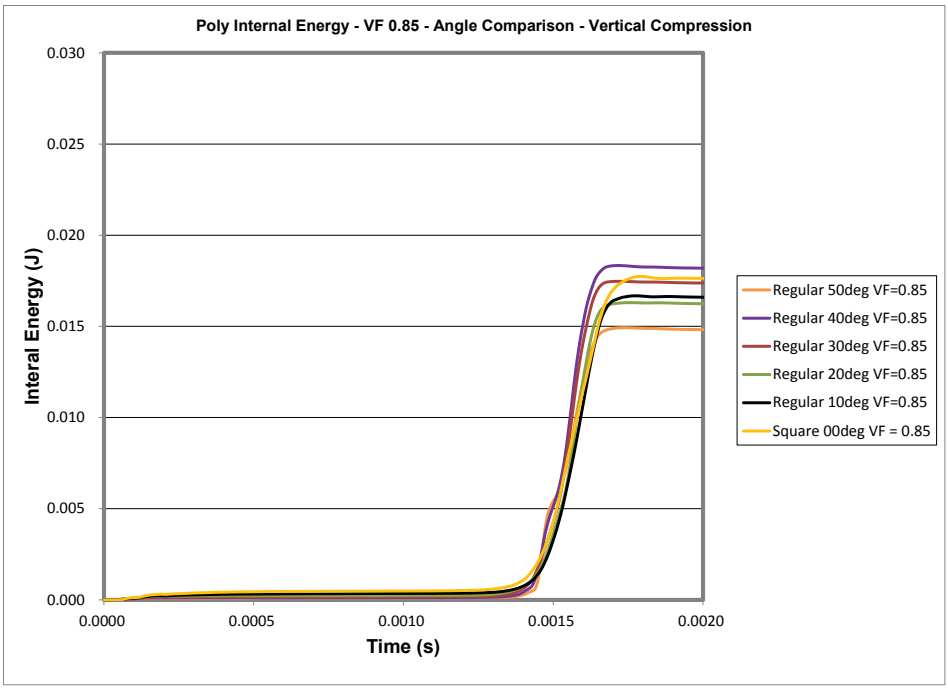

Figure 16: Internal energy time histories obtained using the improved contact parameters for vertical impact on regular honeycomb specimens with void fraction of 0.85 and different angles.

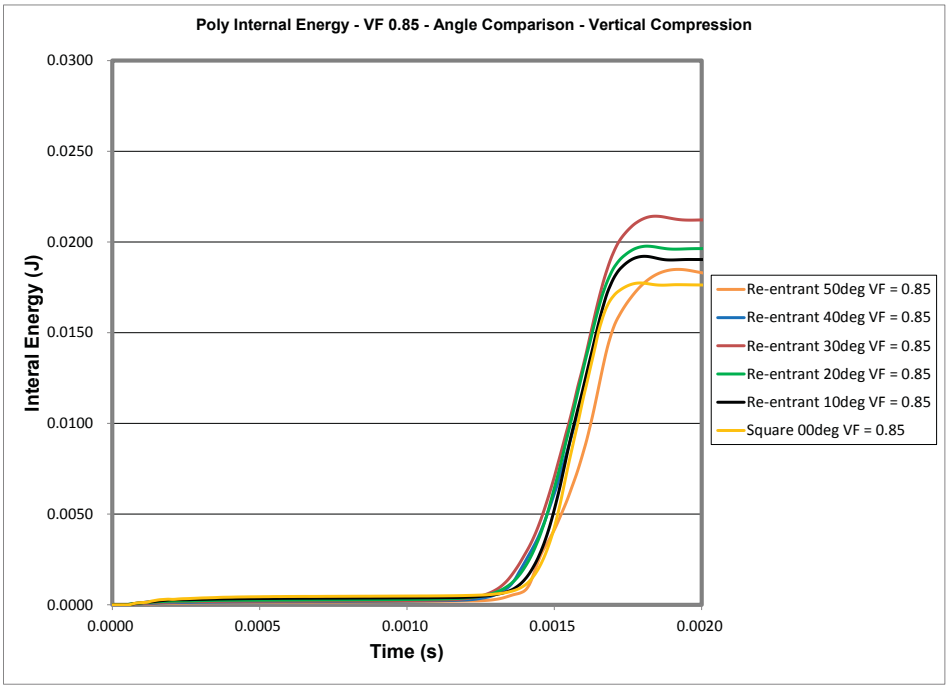

Figure 17: Internal energy time histories obtained using the improved contact parameters for vertical impact on re-entrant specimens with void fraction of 0.85 and different angles.

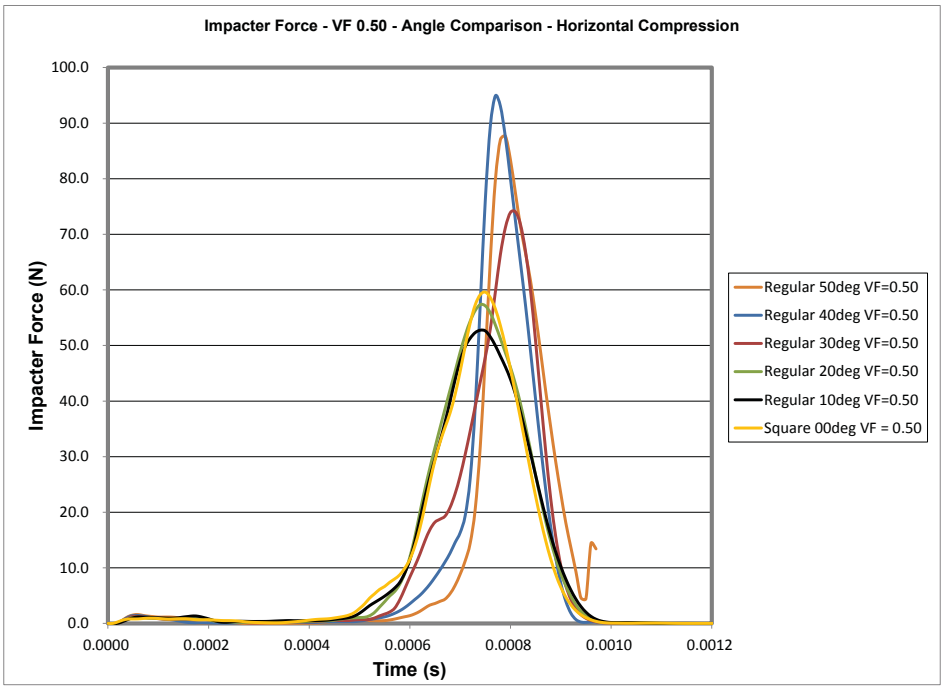

Figure 18: Impact force time histories obtained using the improved contact parameters for horizontal impact on regular specimens with void fraction of 0.5 and different angles.

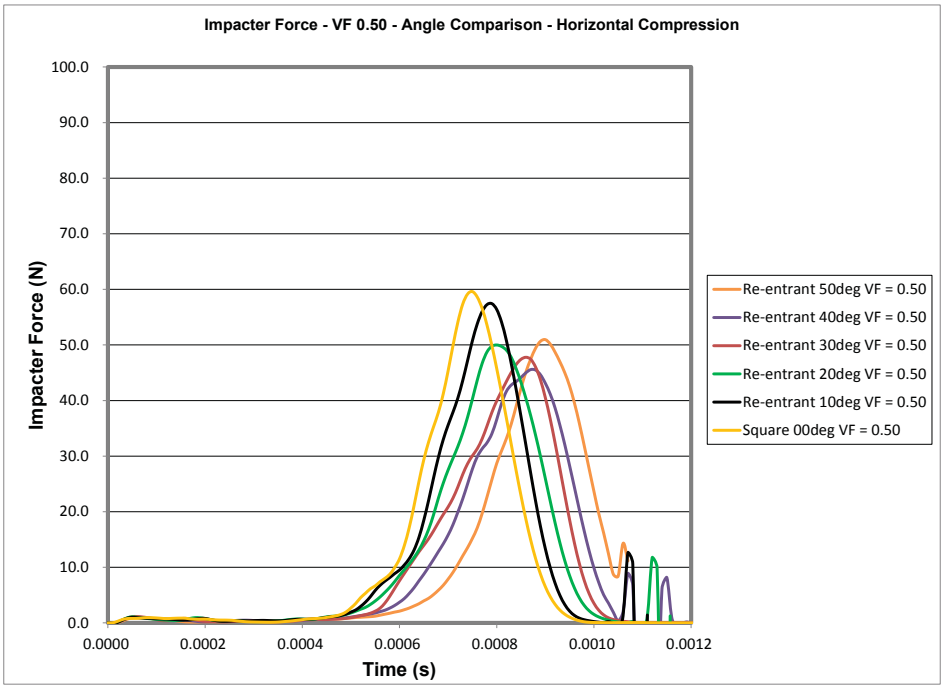

Figure 19: Impact force time histories obtained using the improved contact parameters for horizontal impact on re-entrant specimens with void fraction of 0.5 and different angles.

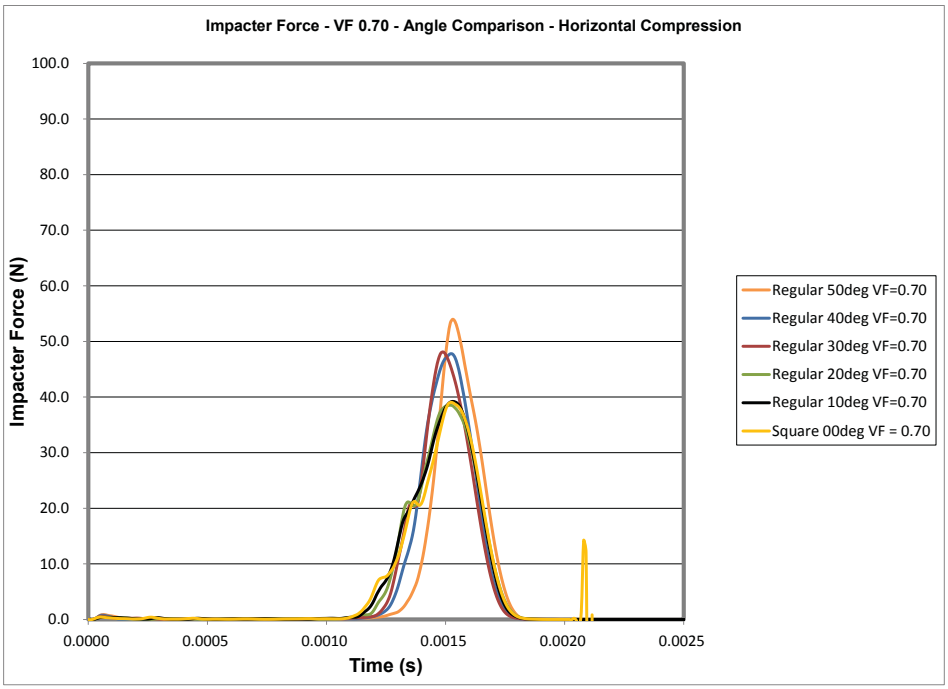

Figure 20: Impact force time histories obtained using the improved contact parameters for horizontal impact on regular specimens with void fraction of 0.7 and different angles.

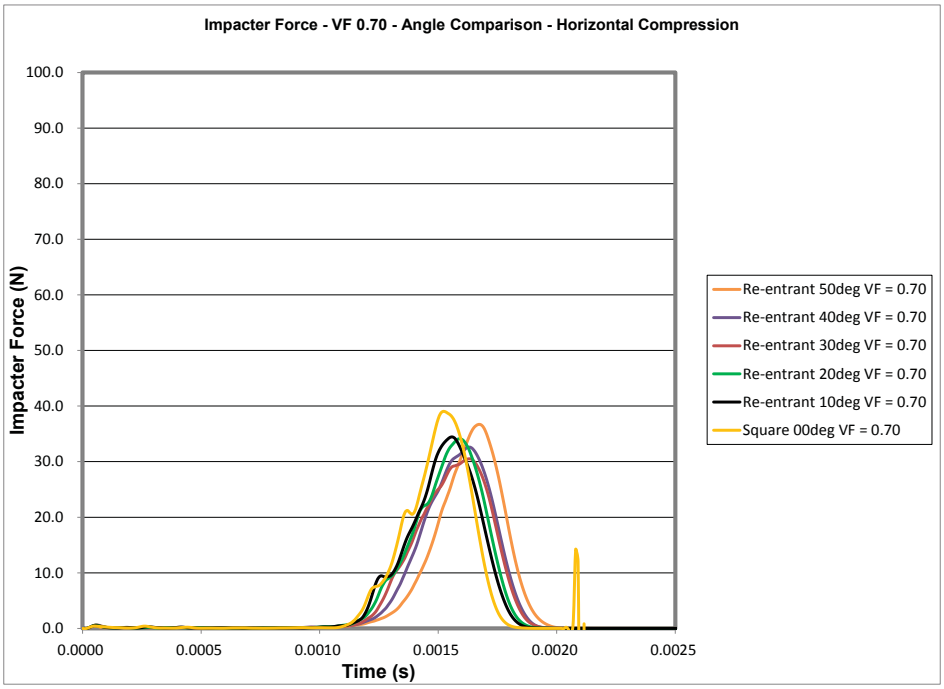

Figure 21: Impact force time histories obtained using the improved contact parameters for horizontal impact on re-entrant specimens with void fraction of 0.7 and different angles.

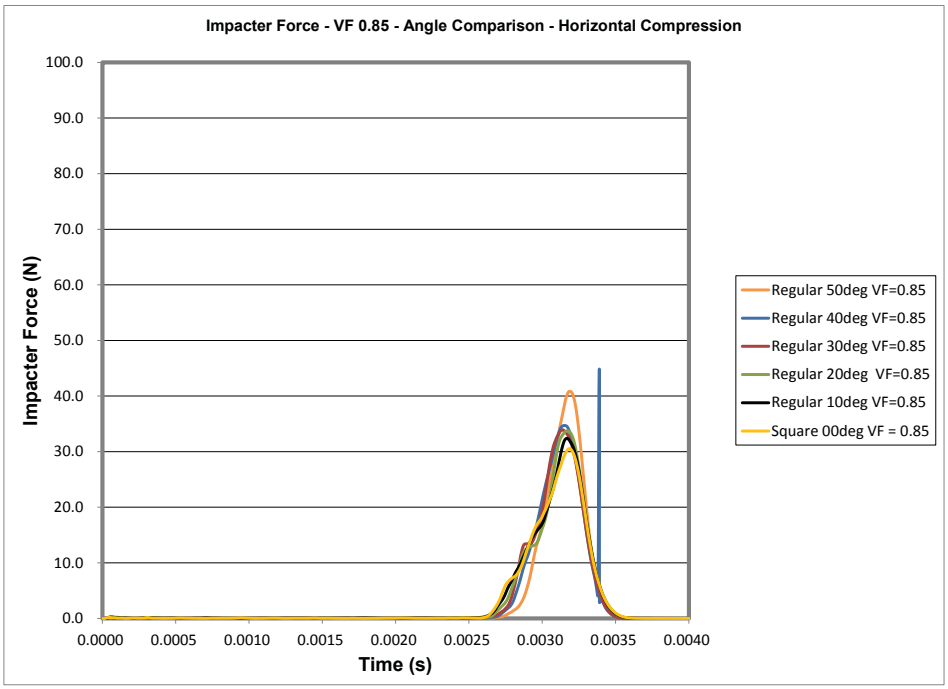

Figure 22: Impact force time histories obtained using the improved contact parameters for horizontal impact on regular specimens with void fraction of 0.85 and different angles.

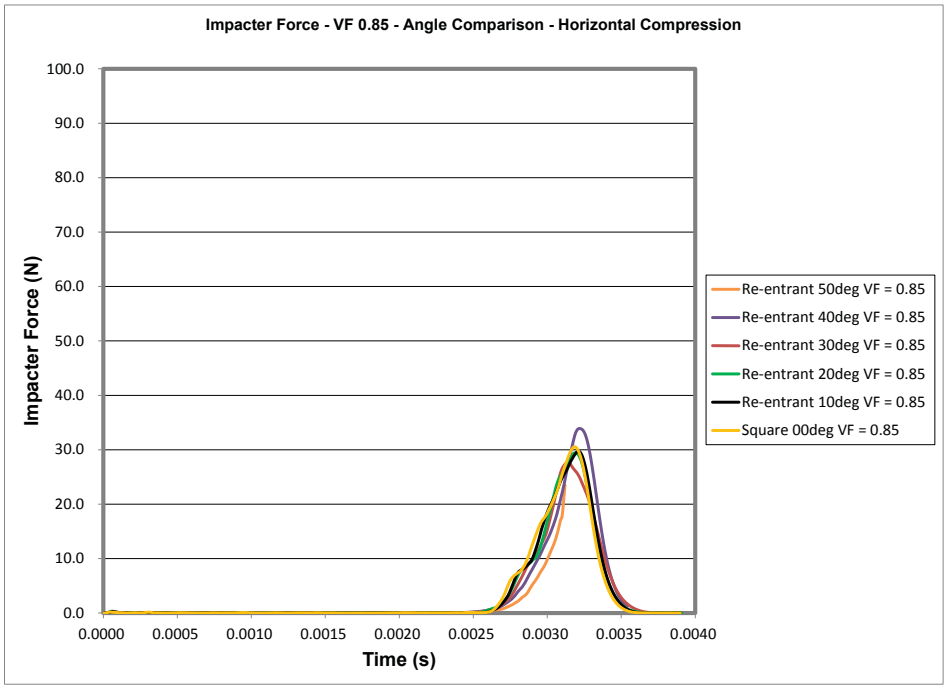

Figure 23: Impact force time histories obtained using the improved contact parameters for horizontal impact on re-entrant specimens with void fraction of 0.85 and different angles.

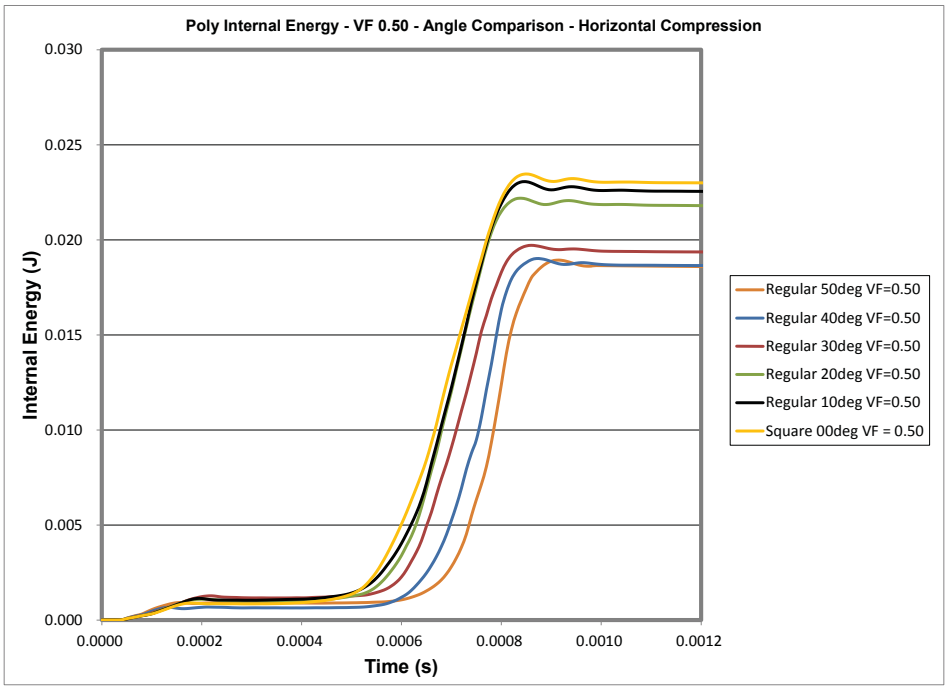

Figure 24: Internal energy time histories obtained using the improved contact parameters for horizontal impact on regular specimens with void fraction of 0.5 and different angles.

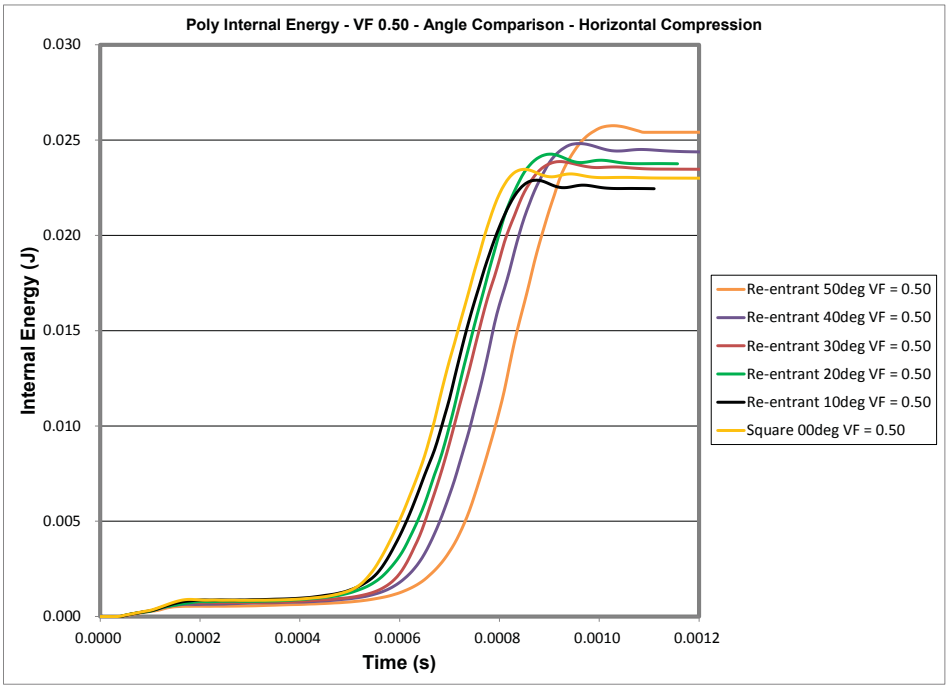

Figure 25: Internal energy time histories obtained using the improved contact parameters for horizontal impact on re-entrant specimens with void fraction of 0.5 and different angles.

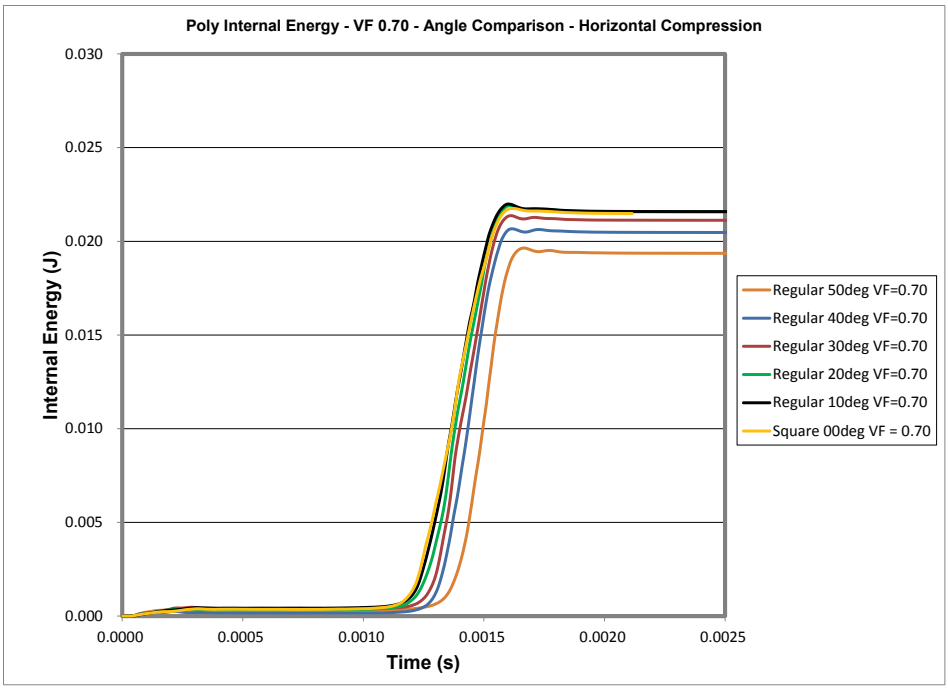

Figure 26: Internal energy time histories obtained using the improved contact parameters for horizontal impact on regular specimens with void fraction of 0.7 and different angles.

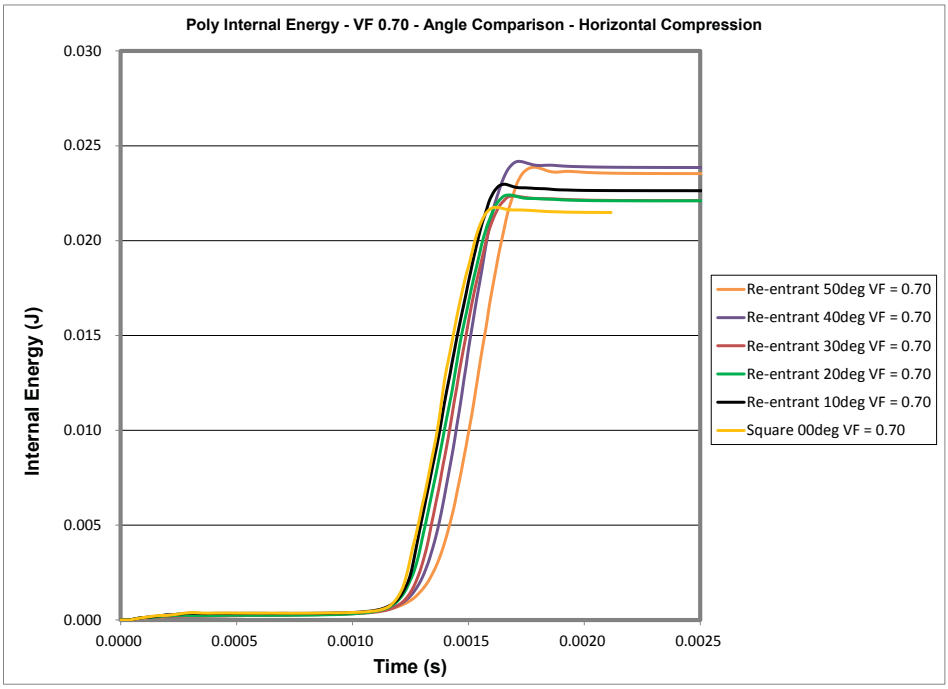

Figure 27: Internal energy time histories obtained using the improved contact parameters for horizontal impact on re-entrant specimens with void fraction of 0.7 and different angles.

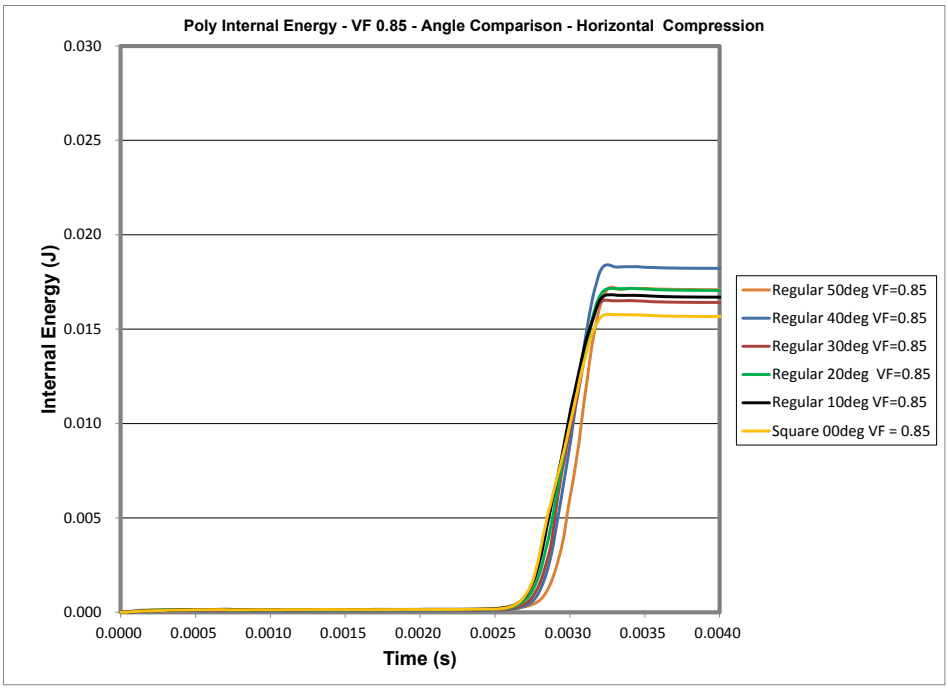

Figure 28: Internal energy time histories obtained using the improved contact parameters for horizontal impact on regular specimens with void fraction of 0.85 and different angles.

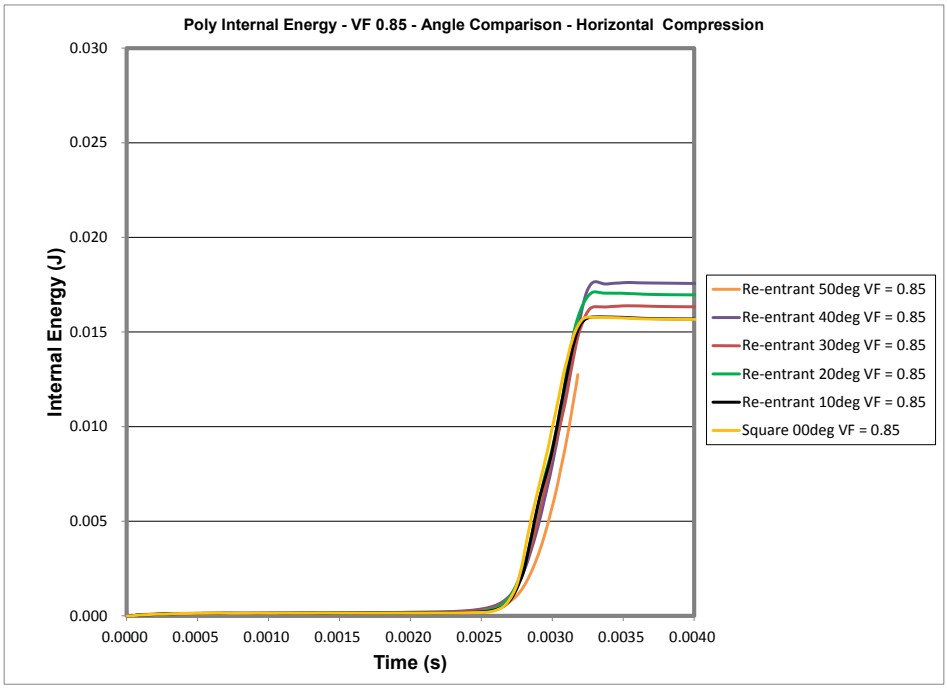

Figure 29: Internal energy time histories obtained using the improved contact parameters for horizontal impact on re-entrant specimens with void fraction of 0.85 and different angles.

2.4 Further Verifications of the Element Formulations for Simulating Auxetic Materials

Because no experimental results on the impact properties of auxetic materials were available, an extensive numerical study was conducted to gain a better understanding of the results of the parametric studies and to verify the behaviors of the shell and solid elements in LS-DYNA. During this verification process, VAST was used to provide reference solutions for comparison.

2.4.1 Solid Polymer Model

The parametric study mentioned above was performed using the 4-noded shell element. Although the shell element represented bending deformations in the ribs very well, some questions were raised regarding its accuracy for modeling fully compact auxetic materials due to the ignorance of through-the-thickness deformations in the shell element. On the other hand, suggestions were made to use the solid element which involved full sets of stress and strain components. However, some preliminary analyses using solid elements yielded quite different results from those of the shell elements as described in Reference [1]. In addition, in order to compare the impact properties of the auxetic materials and solid polymers, impact simulations of solid polymer blocks with equivalent areal density were also performed. Results from these analyses suggested that solid polymer might be more effective on protecting structures than the fully compressed auxetic material, because the solid polymer produced lower peak impact force and absorbed more internal energy. In order to confirm the correctness of the solid element results, verifications on solid elements were first conducted.

The finite element model used in this verification is shown in Figure 30. This polymer block was loaded by uniform pressure on its top surface. The bottom was constrained against motion in the vertical (Z) direction, but permitted to slide frictionless along the horizontal (X) direction. The side surfaces were left free. Two boundary conditions were considered in the Y-direction: fixed and free. The former boundary condition resulted in zero strain in the Y-direction, which was consistent with the plane strain assumption used in the parametric study, and the latter resulted in zero stress in the Y-direction, which represented a plane stress condition. In both cases, LS-DYNA produced deformed shapes as shown in Figure 30. Due to the lack of friction at the bottom of the block, the numerical solution predicted a uniform stress field. This agreed with our expectations.

In order to verify the numerical results, we calculated the effective Young's modulus of the block in the vertical direction using the applied loads and predicted displacements. For the case without constraints in the Y-direction, the effective Young's modulus E' should equal to the Young's modulus of the material. However, in the case of Y-constraints, a consideration of the Hooke's law leads to

$$E' = \frac{E}{1-\nu^2} \tag{1}$$

where E' indicates the effective Young's modulus, E is the Young's modulus of the polymer and ν is the Poisson's ratio. In the present study, we took E=84.7 MPa and ν=0.4 to represent material

properties of a typical polymer. The analytical and numerical values of the effective Young's modulus are compared in Table 2. They are in very close agreement.

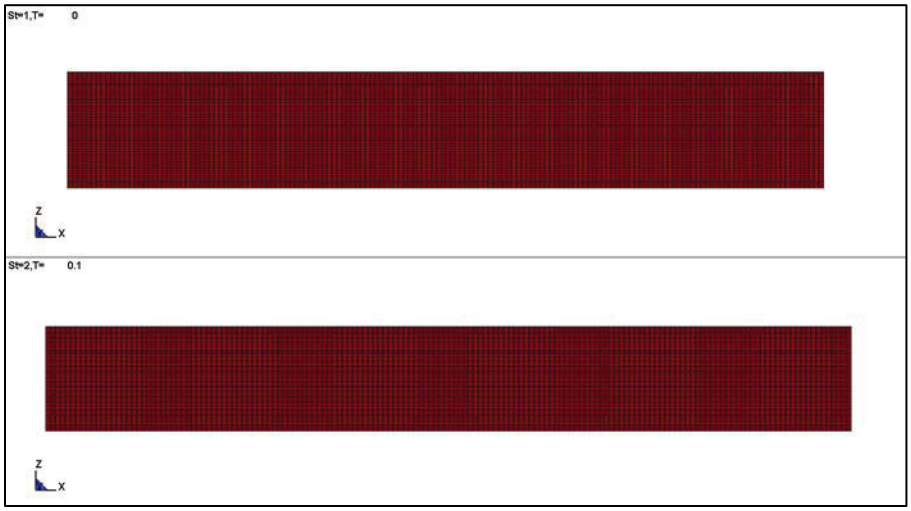

Figure 30: Initial (top) and deformed (bottom) meshes of a solid polymer block subjected to static compression by uniform pressure applied to the top surface.

Table 2: Comparison of analytical and computed values of effective Young's modulus of a polymer block with different boundary conditions

Y-constraint	Effective Young's Modulus *E'* (MPa)	
	Analytical	LS-DYNA
No	84.700000	84.726342
Yes	100.83333	100.83294

2.4.2 Beam Model for Static Analyses

The second verification case involved a beam with square cross-section subjected to uniformly distributed load on its upper surface. The geometry and the global coordinate system are shown in Figure 31. If the beam length is indicated by L, the cross-section by $B \times W$ and the distributed load per unit length by p, the linear static solutions of the maximum vertical deflection at the middle of the beam can be expressed as [2]

$$\delta_Z = \frac{5pL^4}{384EI} = \frac{60pL^4}{384EBW^3} \qquad (2)$$

for simply-support boundary conditions and

$$\delta_Z = \frac{pL^4}{384EI} = \frac{12pL^4}{384EBW^3} \tag{3}$$

for clamped boundary conditions, respectively. Taking L=10 mm, B=W=1 mm, E=200000 MPa, p=128N/mm, we obtained δ_Z =1.0 mm for simply supported beam and δ_Z =0.2 mm for beam with clamped boundary conditions.

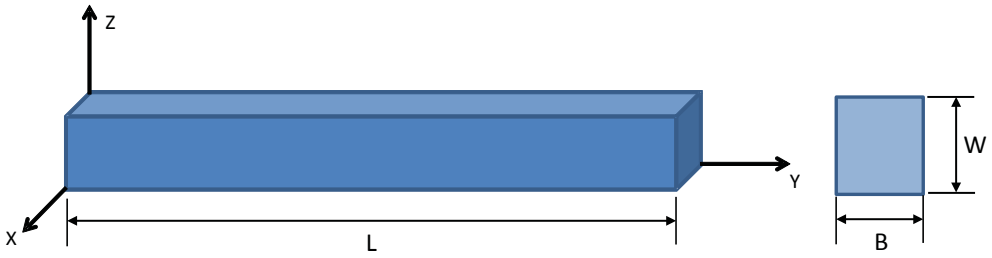

Figure 31: Problem definition of the beam verification case

The beam test problems were solved by using both VAST and LS-DYNA. The purpose of these tests was to verify the accuracy of the 4-noded shell and 8-noded solid elements for representing bending deformations in beam-like structures because similar deformations were experienced by the ribs in auxetic materials. The shell and solid element meshes used in these tests are shown in Figure 32 and 33 as the blue lines, respectively.

In these finite element models, the simply supported and clamped boundary conditions were applied to the end nodes. However, there was a remaining constraint condition that needed to be considered. This was the expansion in the width (X) direction. As explained earlier in this chapter, in LS-DYNA simulations of the auxetic materials, a thin slice of the material specimen was included in the finite element model and the out-of-plane deformation of the model was constrained to ensure numerical stability. These boundary conditions were equivalent to constraining expansion in the X-direction in this test model. The influence of this constraint was investigated.

The linear static cases were first considered and the VAST predicted deformed configurations are depicted in Figures 32 and 33. The maximum centre deflections predicted by VAST and LS-DYNA are compared with the analytical solutions in Tables 3 and 4 for different boundary conditions. These results indicated that both the shell and solid elements in VAST and LS-DYNA performed well in this test and produced results consistent with the analytical solutions. The shell solution was insensitive to the constraint in the X-direction. However, for solid elements, the X-constraint resulted in an increase in the overall stiffness, leading to a reduction in the deflection. Regarding the accuracy of the numerical solutions, it was noticed that the shell elements in both VAST and LS-DYNA produced identical results, but the solid element in LS-DYNA had a tendency to overestimate the deflections.

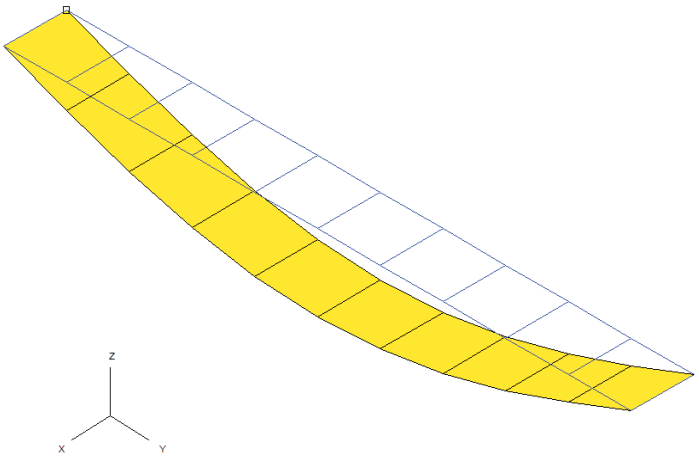

Figure 32: Original and deformed configurations of simply supported beam modelled using shell elements in VAST.

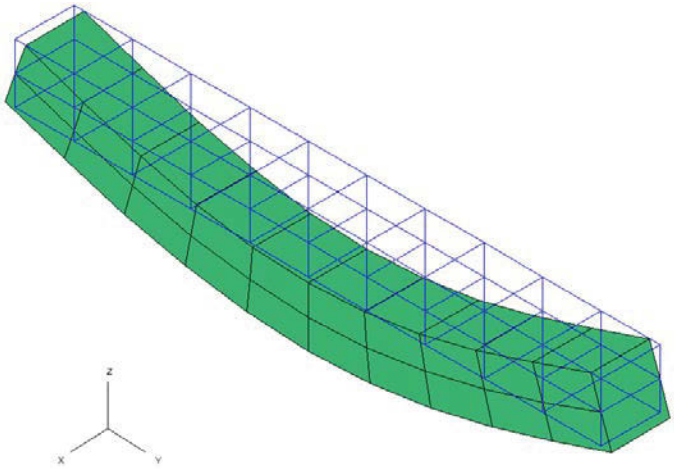

Figure 33: Original and deformed configurations of clamped beam modelled using shell elements in VAST.

Geometrically nonlinear static analyses of the beam were then performed and the results are presented in Figures 34-35 for different constraint conditions in the X-direction. The influences of the element type and boundary condition on nonlinear results seemed to be consistent to those on linear static solution, namely, the shell solutions are in good agreement with the solid element results obtained without the X-constraint. The application of the X-constraint increased the overall stiffness of the beam. The LS-DYNA results are in general agreement with the VAST solutions. It should be pointed out that these LS-DYNA analyses were performed using the implicit version of the program, and the element formulation utilized in the analyses may not be identical to that used in its explicit counterpart.

Analytical solutions for nonlinear deformations are not identified. However, the initial slopes of all curves are consistent with the analytical solutions given in Tables 3 and 4.

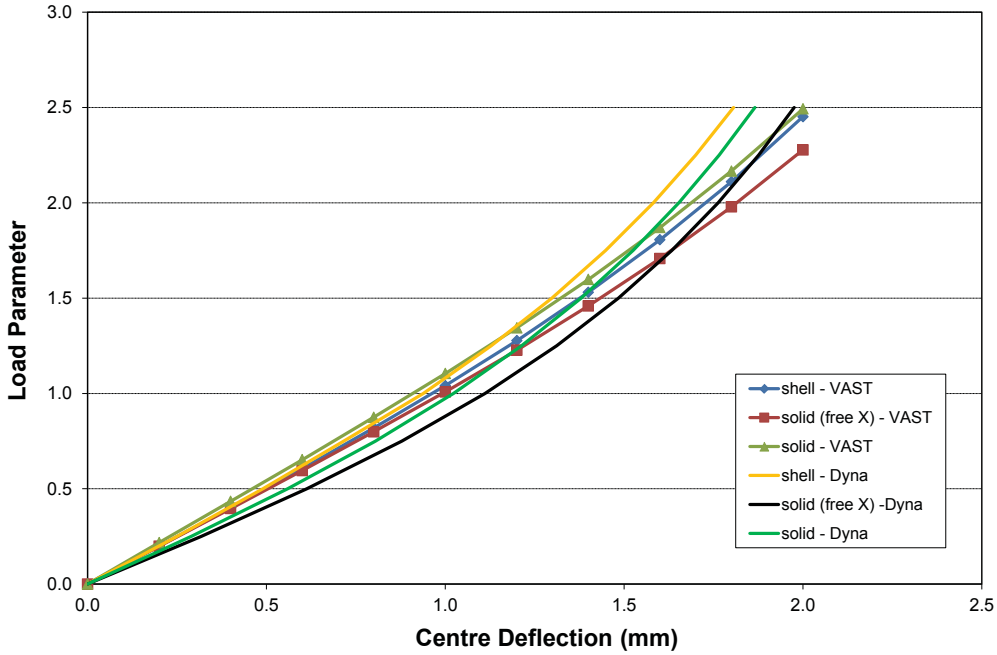

Figure 34: Comparison of geometric nonlinear responses for simply-supported beam obtained using shell and solid elements with different X-constraints.

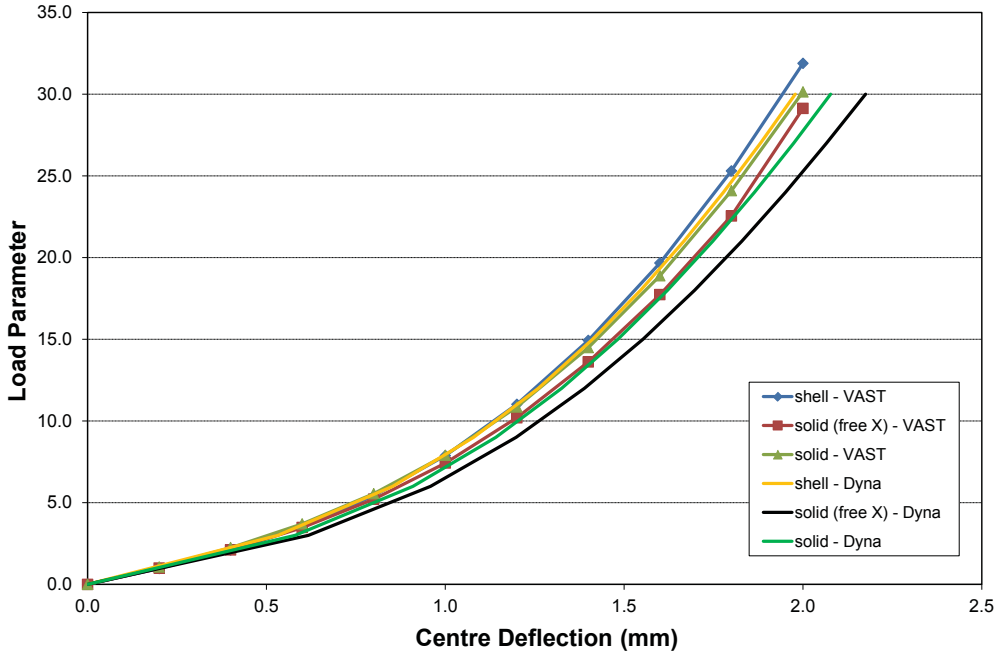

Figure 35: Comparison of geometric nonlinear responses for clamped beam obtained using shell and solid elements with different X-constraints.

Table 3: Comparison of analytical and numerical results for simply supported beam.

X-constraint	Analytical	VAST		LS-DYNA	
		Shell	Solid	Shell	Solid
No	1.0	1.008	1.0032	1.00	1.29
Yes	1.0	1.008	0.9154	1.00	1.18

Table 4: Comparison of analytical and numerical results for clamped beam.

X-constraint	Analytical	VAST		LS-DYNA	
		Shell	Solid	Shell	Solid
No	0.2	0.213	0.203	0.213	0.264
Yes	0.2	0.213	0.191	0.213	0.244

2.4.3 Beam Model for Dynamic Analyses

In order to verify the shell and solid elements in the explicit version of LS-DYNA for nonlinear dynamic analyses with bending dominated deformations, geometrically nonlinear dynamic responses of the simply-supported beam were computed for a sudden application of the pressure loads, such that

$$p(t) = p_0 H(t) \tag{4}$$

where p_0 was taken as 128 M/mm. The shell element solution from LS-DYNA are compared with shell and solid element solutions from VAST in Figure 36, where reasonably close agreement between all solutions was observed. However, very serious hourglass modes appeared in the LS-DYNA explicit solutions using the 8-noded solid elements. In order to reduce the hourglass problem, a refined solid element mesh was generated as shown in Figure 37. However, even with this refined mesh, the magnitude of the hourglass modes still increased rapidly with time as indicated in Figure 38 and caused the analyses to fail after just a few vibration cycles (Figure 37).

These test results seemed to suggest that the solid element in LS-DYNA explicit was not suitable for nonlinear dynamic analyses involving bending dominated deformations. In other words, the previous results on auxetic material simulations using solid elements might not be reliable. Based on these test results, the 8-noded solid element was not used in the present study.

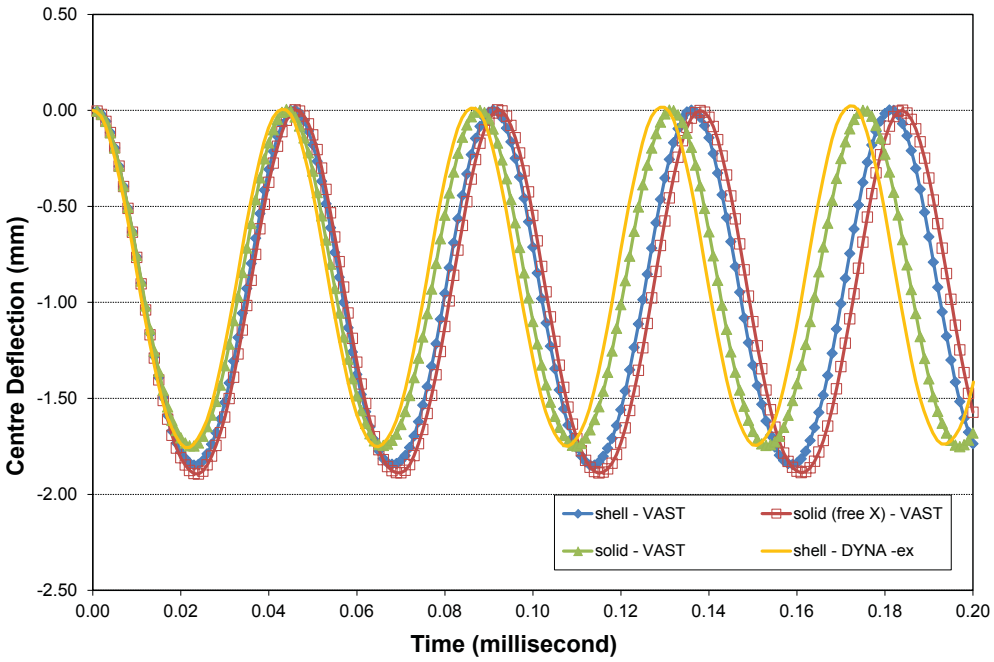

Figure 36: Comparison of geometric nonlinear dynamic responses for simply supported beam obtained using shell and solid elements with different X-constraints.

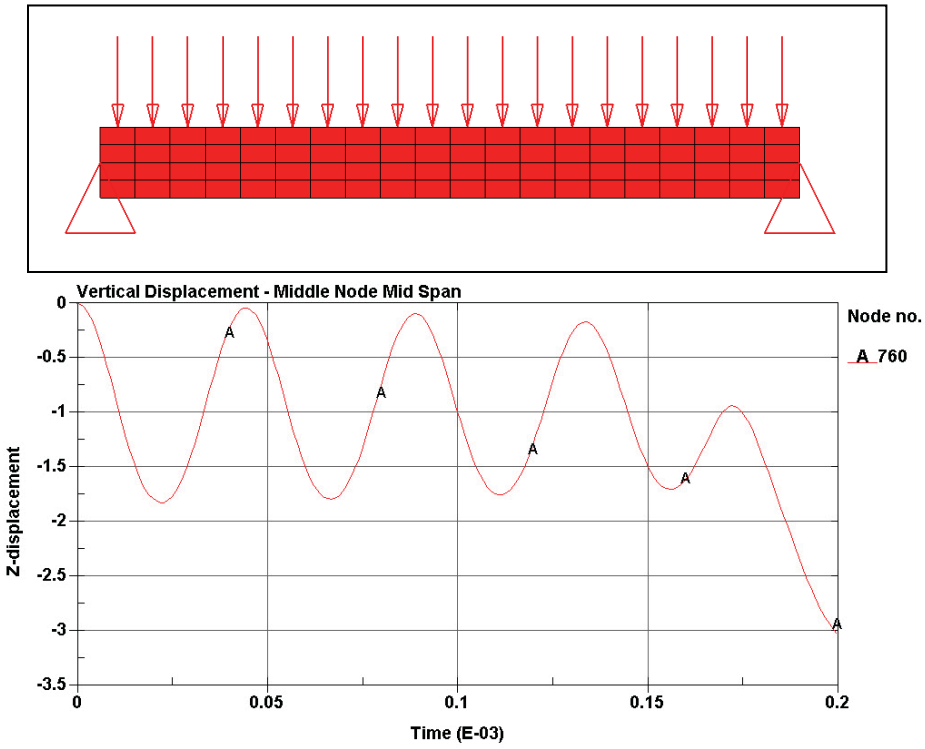

Figure 37: Solid element mesh and displacement time history obtained by LS-DYNA-explicit.

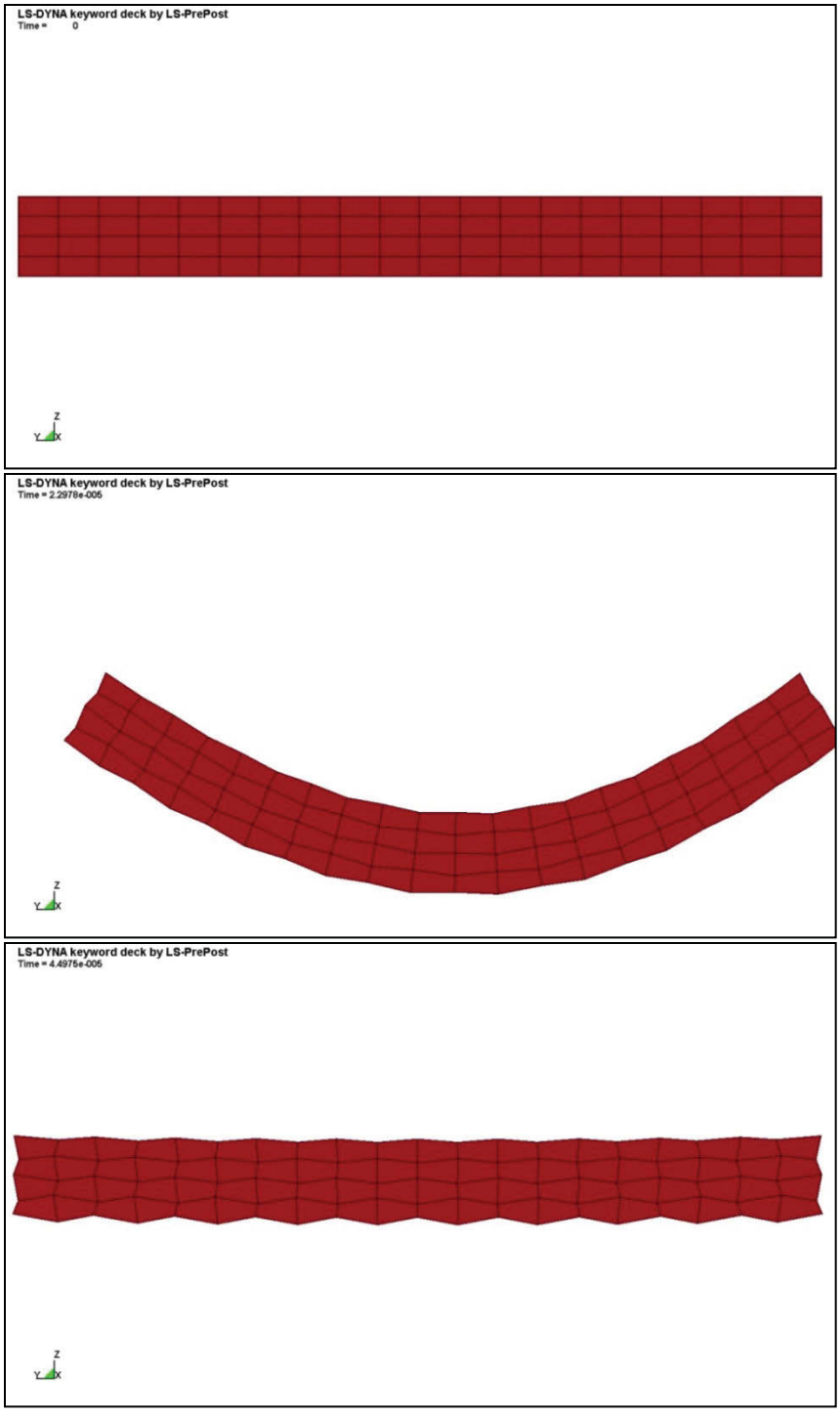

Figure 38: Initial mesh (t=0) and deformed shapes (t=0.023ms, 0.045 ms) of simply-supported beam obtained using solid element in LS-DYNA-explicit.

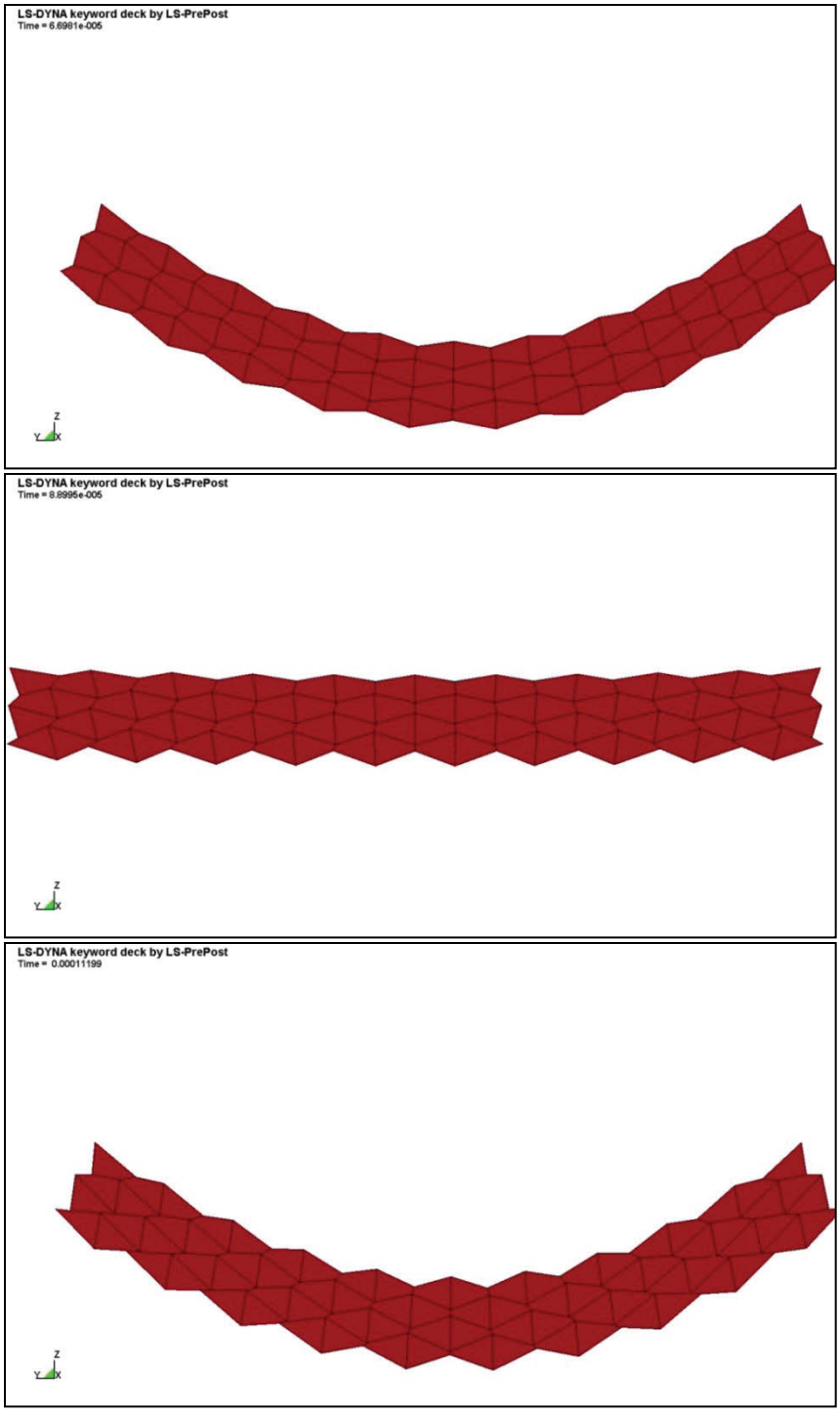

Figure 38 (cont'd): Deformed shapes (t=0.067ms, 0.089 ms, 0.112ms) of simply-supported beam obtained using solid element in explicit LS-DYNA-explicit.

2.4.4 Single Cell Model of Auxetic Material

In order to verify the performance of the shell element for modelling auxetic materials and to justify the predicted mechanical behaviors in the parametric study, numerical analyses were conducted using a finite element model that contained a single unit cell in auxetic materials. The model showing in Figure 39 was for a re-entrant honeycomb with θ=40^o. Due to symmetry, only half of the cell was included in the model. A uniform pressure was applied to the top rib of the cell to simulate the impact force generated from a flat impacter. The bottom of the model was fixed in the vertical (Z) direction. To be consistent with the constraints used in the simulations of auxetic materials, symmetry boundary conditions, such as u_Y=0 and θ_X=θ_Z=0, were applied in the planes parallel to the X-Z plane.

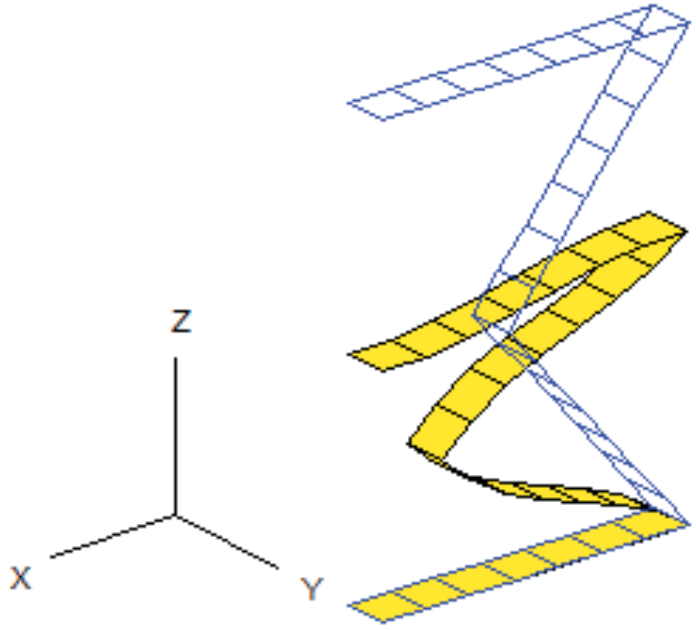

Figure 39: Initial mesh (blue line) and deformed configuration (yellow) for nonlinear analyses of a single cell from an auxetic material.

Nonlinear quasi-static responses of the single cell were first obtained for void fraction of 0.5 by considering both linear elastic and elastic-plastic material properties. The load-displacement curves obtained using various material models (E=elastic, PW=piecewise plasticity) and solution methods (EXP=explicit, IMP=implicit, QS=quasi-static) in VAST and LS-DYNA are presented in Figure 40. It should be pointed out that in these solutions, contacts between the ribs were not considered because at this stage, we would like to focus on the bending behaviour of the ribs. Because a very slow loading rate was specified in the dynamic analyses, the dynamic and quasi-static solutions were expected to be in close agreement, so the nonlinear dynamic capability could be verified. Figure 40 confirmed that the static and dynamic solutions are indeed in good agreemnt for most of the cases. The only exception was the result of the explicit solution of LS-DYNA using the piecewise plastisity (PW) model which predicted a snap-through type of behaviour with a sudden increase of displacement at a load level of 0.04 N.

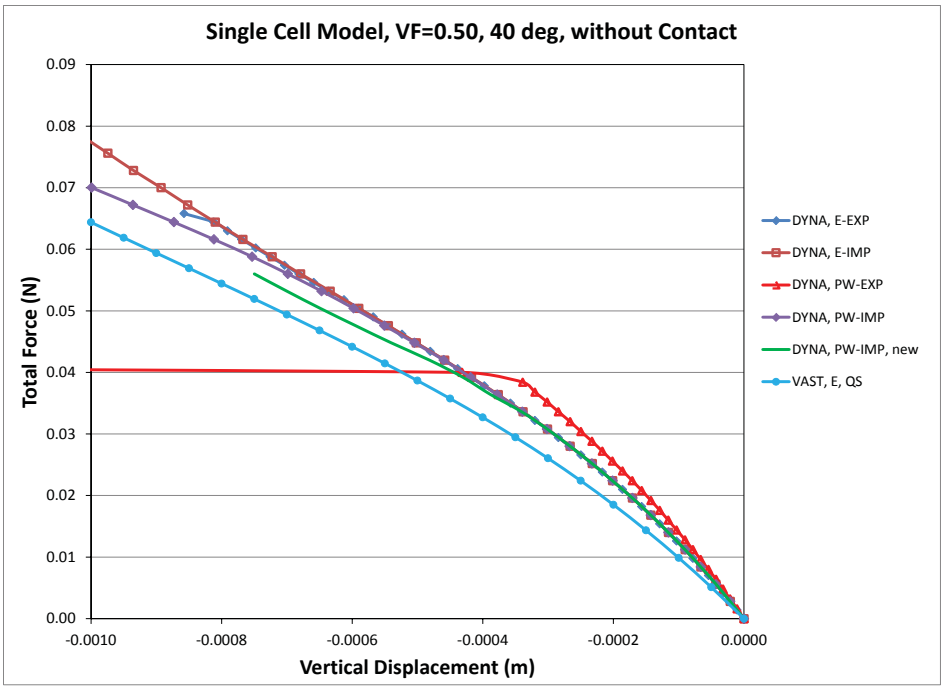

Figure 40: Comparison of load-displacement curves of the single cell model with void fraction of 0.5 obtained through quasi-static and dynamic analyses using LS-DYNA and VAST.

At this point, the LS-DYNA technical support people were contacted for help and they suggested to add several cards to our solution deck as follows:

```
*CONTROL_SHELL
$#   wrpang      esort      irnxx     istupd     theory        bwc      miter       proj
  20.000000          0         -2          0          2          1          1          1
$# rotascl     intgrd     lamsht     cstyp6     tshell
   1.000000          0          0          1          0
$# psstupd    sidt4tu      cntco     itsflg     irquad
           0          0          0          0          2
$#   nfail1     nfail4    psnfail     keepcs      delfr    drcpsid     drcprm
           0          0          0          0          0          0  1.000000
*CONTROL_BULK_VISCOSITY
$#        q1         q2       type      btype
   1.500000 6.0000E-2         -2          0
*CONTROL_ACCURACY
$#      osu        inn     pidosu
          0          4          0
```

These suggested control cards contained a number of non-default values of the solution control parameters which are documented here.

In ****CONTROL_SHELL*** card, which provided shell response controls, the non-default parametes include:

IRNXX = -2

This option controls the shell normal update option which affects the Belytscho-Tsay shell formulations used in present study. Setting this paremeter to -2 means “nodal fibers are updated based on the nodal rotation at the location of the fiber”.

BWC = 1

This option controls the warping stiffness for belytschko-Tsay shell element. Setting it to 1 means “Belytschko-Wong-Chiang warping stiffness is added to the solution”.

PROJ = 1.0

This option controls the projection method for the warping stiffness of Belystchko-Wong-Chiang elements. For explicit impact analyses this should be set to 1.0 which is default for implicit solutions. However, when drill projection is used, the option may cause element to strain under rigid body rotation and result in additional non-physical stiffness.

PSTUPD = 0

This parameter specifies which part ID will or will not have thickness updates. Specifying PSTUPD to 0 means “all deformable shells have their thickness updated”.

IRQUAD = 2

This card specifies the in-plane integration rule for 4-node shell elements. With IRQUAD = 2, “2×2 Gauss quadrature integration is employed”.

The ***CONTROL_BULK_VISCOCITY*** card treats shockwaves by adding an artificial viscocity term which smears the shock discontinuities into rapidly varying continuous transition regions. This term also keeps the Hugoniot jump conditions valid.

TYPE = -2

This card defines the type of bulk viscocity applied. When setting to -2, this option computes and includes the internal energy dissipated by the viscocity in the overall energy balance.

The ***CONTROL_ACCURACY*** card improves the accuracy of the calculation.

INN = 4

This parameter modifies the node numbering such that it is invariant. This shift in node number alters the local system such that it is an exact multiple of 900 for irregularly shaped elements. This card improves the solution by calculating element forces independent of node sequencing, fixing the material directions such that hourglassing will not affect them and makes the solution more stable.

The improved explicit solution using the provided LSTC input cards is shown Figure 40 as a green curve (PW-LSTC new). The improved solution is stable beyond the original snap-through load of 0.04 N and in good agreement with all other solutions.

To verfify solutions with contact conditions, the dynamic response of a single unit cell with void fraction of 0.85 was considered. The quasi-static load-displacement curve without contact was first obtained by VAST and used as a reference for comparison. This reference solution is compared with the dynamic results including contact in Figure 41. The results with and without contact agreed until the contact occurred. This comparison indicated that both the explicit and implicit solution options in LS-DYNA produced correct results.

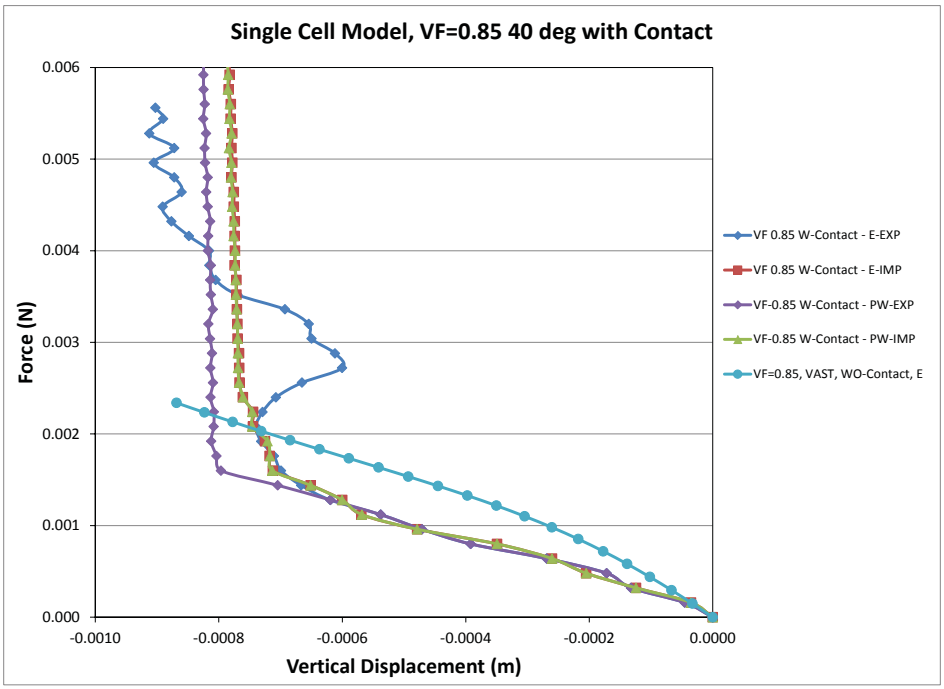

Figure 41: Comparison of load-displacement curves of the single cell model with void fraction of 0.85 obtained through quasi-static and dynamic analyses using LS-DYNA and VAST.

At this point, we estimated the equivalent Young's modulus for both cell geometries using the initial slopes of the nonlinear solutions. The results are compared with the analytical solutions in the Table 5. It should be noted that through very accurate estimates of the equivalent Young's modulus could not be made using such a simple model, the correct orders of magnitude were indeed be predicted. The results in Table 5 indicated that even with a void fraction of 0.5, the initial stiffness of the auxetic material is only 1.6% of the stiffness of solid polymer, suggesting that the extremely low stiffness observed in the parametric study is likely to be physical.

Table 5: Comparison of equivalent Young's modulus of re-entrant honeycombs

Void Fraction	Equivalent Young's Modulus E' (MPa)			Original E of Polymer	Ratio of Modulus E'/E (%)
	Gibson [3]	Master [4]	VAST		
0.50	2.2778	1.7081	1.4378	87.40	1.6451
0.85	0.0658	0.0679	0.0637	87.40	0.0728

2.4.5 Application of New LS-DYNA Solution Parameters to Impact Simulations of Auxetic Materials

With the success of the verification efforts using single cell models, we refocused our attention on the whole auxetic material models with many cells. In order to ensure computational efficiency, a reduced model that included ¼ width of the original model was utilized in these tests. The re-entrant honeycomb with θ=40^o and void fraction of 0.85 was considered and the un-deformed finite element model is depicted in Figure 44 (a). The mass of the impacter was also reduced by a factor of 4, but the impacter velocity was still set to 10 m/s.

Numerical results were first obtained using the explicit solution algorithms for both linear elastic and piecewise plastic material properties and the impacter force time histories are presented in Figures 42 and 43. As before, these results indicated that the auxetic materials produced very little resistance to the impacter until it started to become fully compact.

Implicit solutions were then obtained for verification purposes. These initial runs were performed using the default value of a contact control parameter IGAP and the results for linear elastic and piecewise plastic materials are shown in Figure 42. Surprisingly, the implicit solution predicted a significant resistance of the auxetic material to the impacter from early stage of deformation and the impacter rebounded after the first two rows of the cells were compressed as indicated in Figure 44. A further investigation revealed that in the implicit solver of LS-DYNA, if the default value of IGAP is used, a sticky contact condition is assumed for improved convergence. In the above analyses, this "sticky" contact condition resulted in unrealistically high stiffness of the auxetic material.

In order to allow sliding between the contact surfaces in implicit solutions, IGAP=2 must be used. Reanalysis using IGAP=2 produced a much lower impact force at the beginning of the transient as detailed in Figure 43, but the solution soon became unstable, leading to serious convergence difficulties. The deformed configurations obtained from this analysis were also very irregular and unrealistic as indicated in Figure 45. However, the available implicit solution with IGAP=2 was found to be in close agreement with those from the explicit solutions.

To assess the influence of frictions at the contact surfaces, two additional explicit solutions were performed using a friction coefficient of 1.16 between the contact surfaces. This value of friction coefficient is typical for rubber to rubber contact [5]. The impact force time histories from these runs are shown in Figure 48 and these results revealed a similar behavior of the auxetic material as predicted by earlier explicit solutions. However, be comparing Figures 46 and 47, it is realized that the inclusion of friction resulted in more stable solutions.

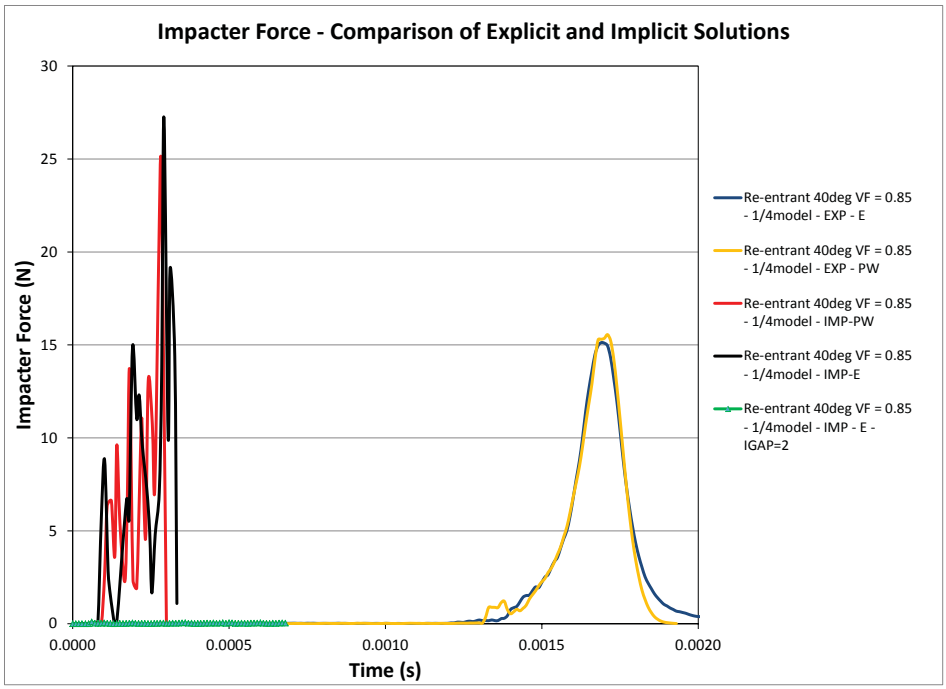

Figure 42: Comparison of impact force time histories for the ¼ test model obtained using different material properties, numerical integration algorithms and contact options.

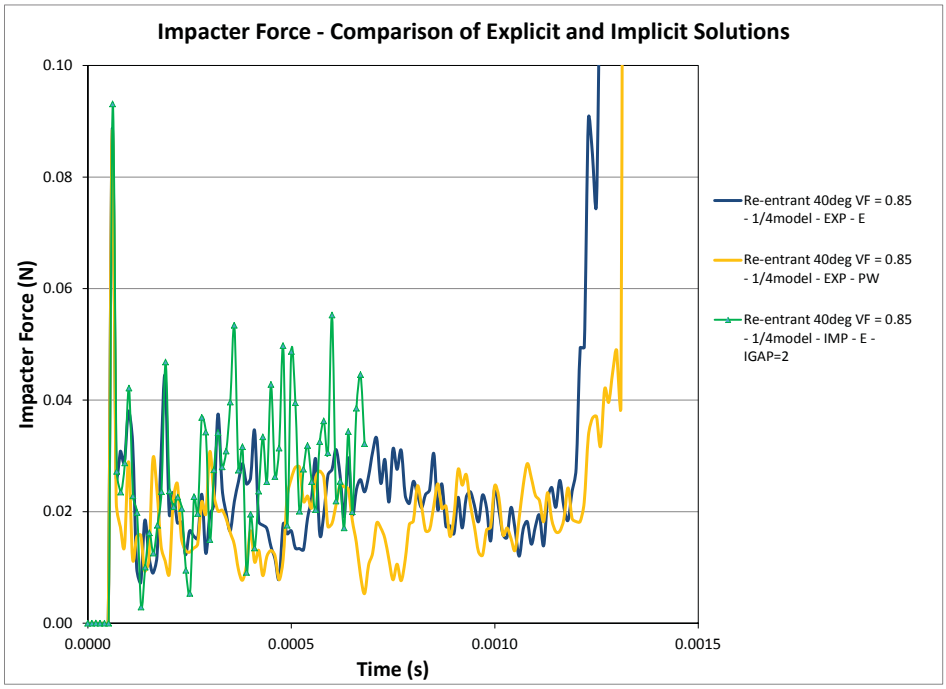

Figure 43: Details of the solutions for the ¼ test model obtained using the explicit integration algorithm and implicit integration algorithm with sliding contact condition (IGAP=2).

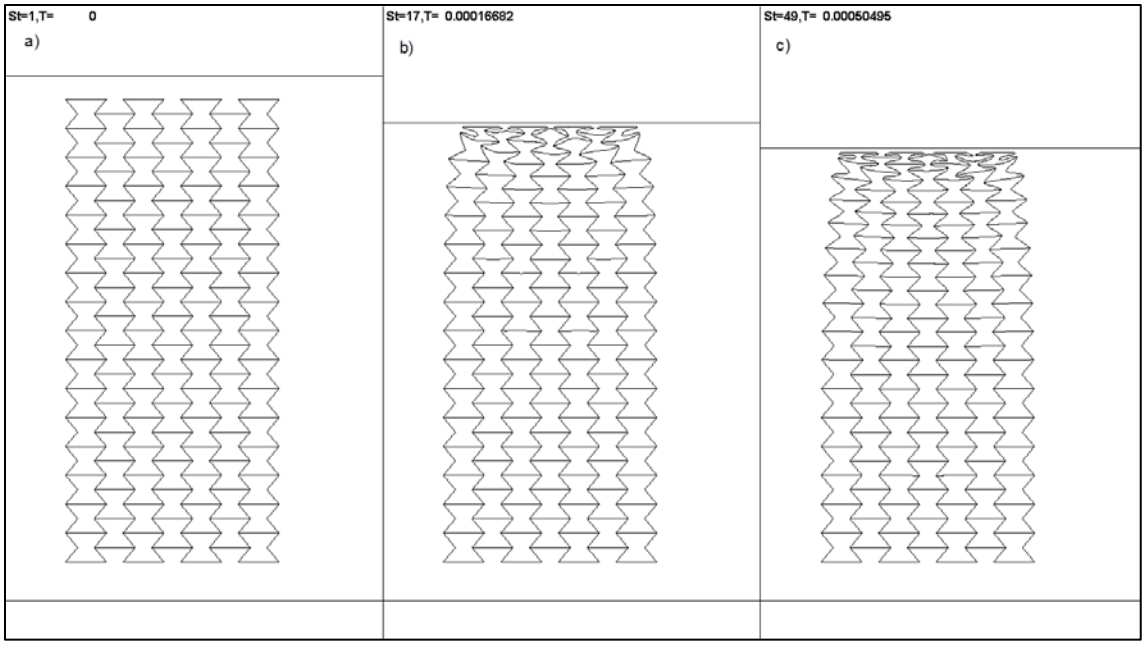

Figure 44: Implicit solution with the default IGAP experiences non-physical stickiness inherent in the implicit contact algorithm to aid convergence. The compressed states are presented at a) initial condition, b) partially impacted and c) final impacted position with impacter rebounding.

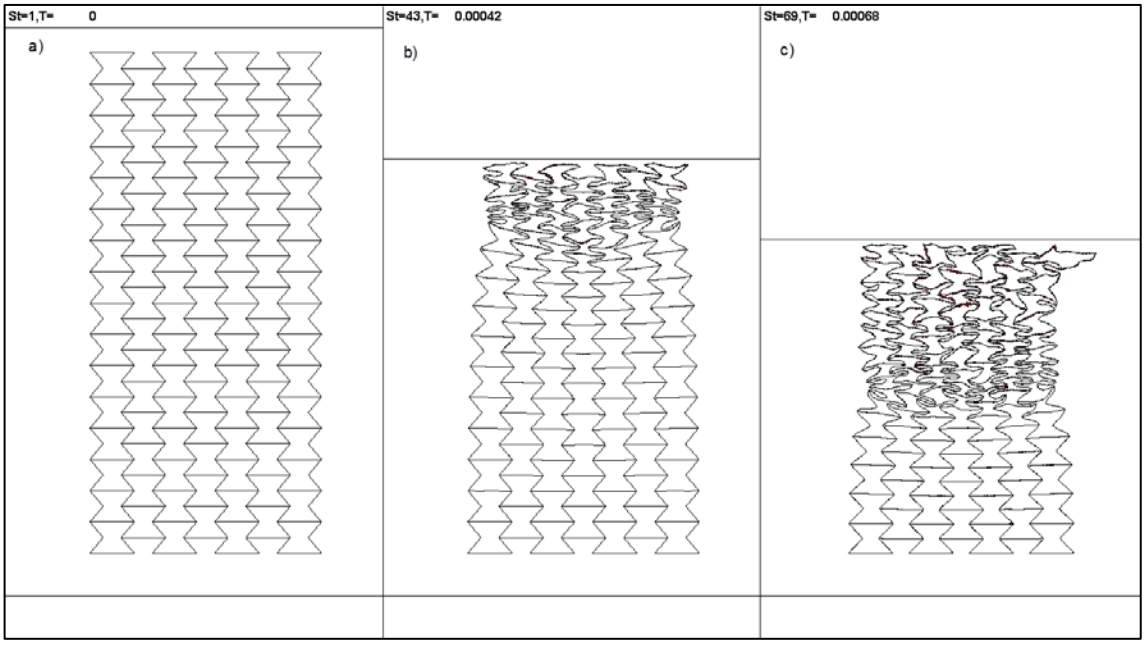

Figure 45: Implicit solution with IGAP=2 (allowing sliding between the contacting surfaces) experiences numerical stability problems. The compressed states are presented above at a) initial condition, b) partially impacted and c) position near convergence failure.

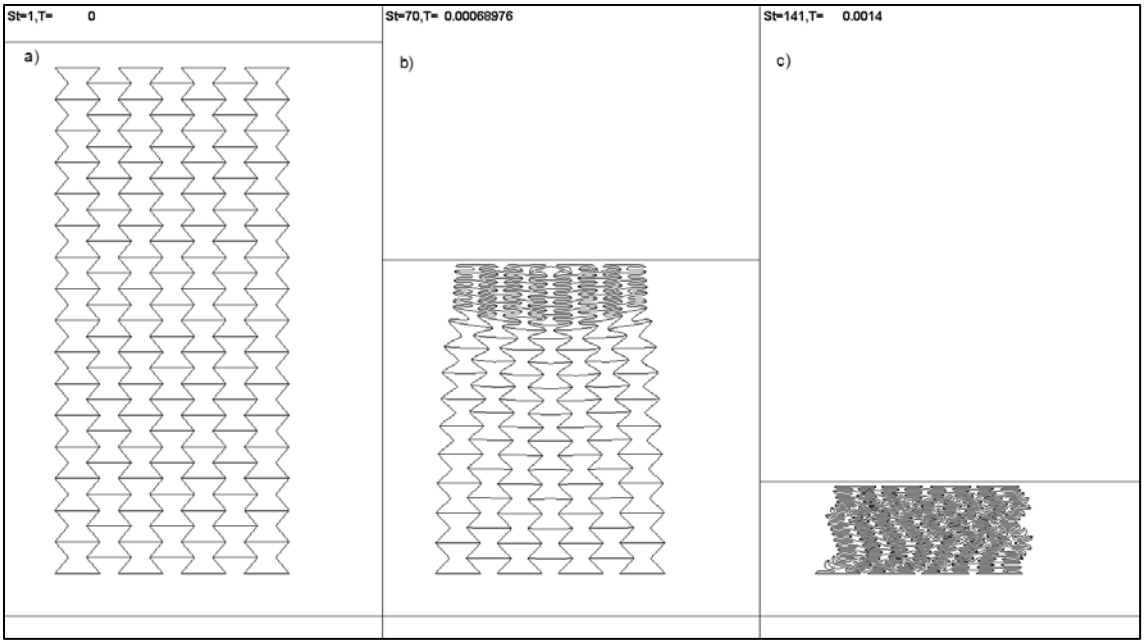

Figure 46: Explicit solution without friction produced symmetrical stable collapse pattern until the material was fully compressed. The compressed states are presented above at a) initial condition, b) half full compression and c) nearly full compression

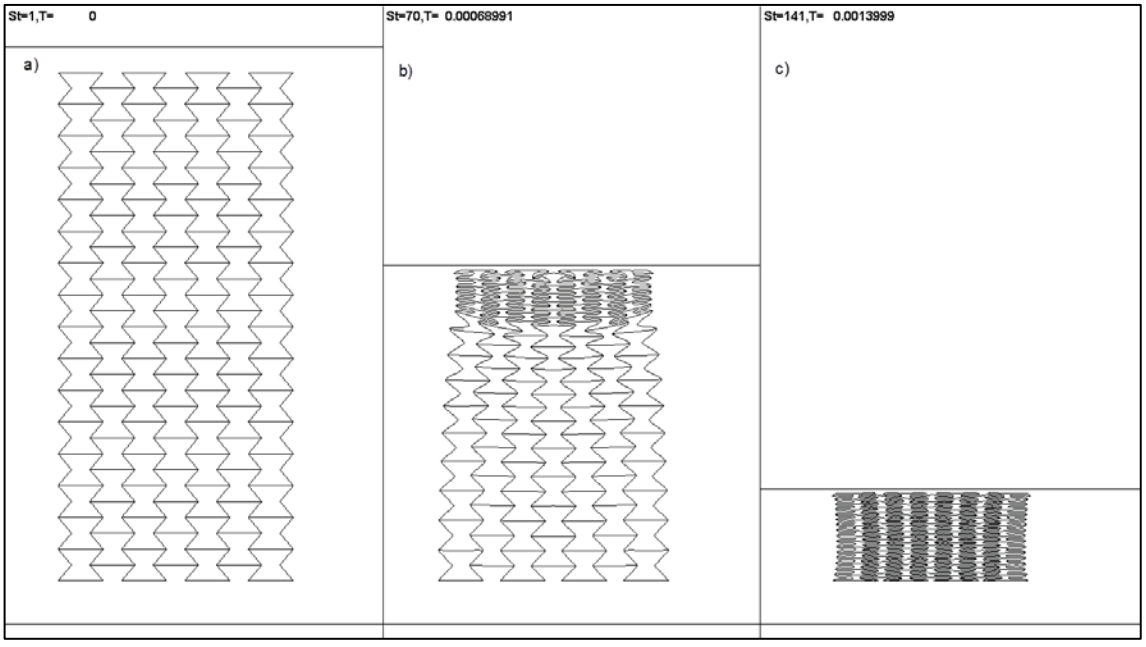

Figure 47: Explicit solution with friction coefficient of 1.16 (rubber on rubber). The compression behaviour was much more stable than model without friction and has a symmetrical collapse pattern. The compressed states are presented above at a) initial condition, b) half full compression and c) near full compression

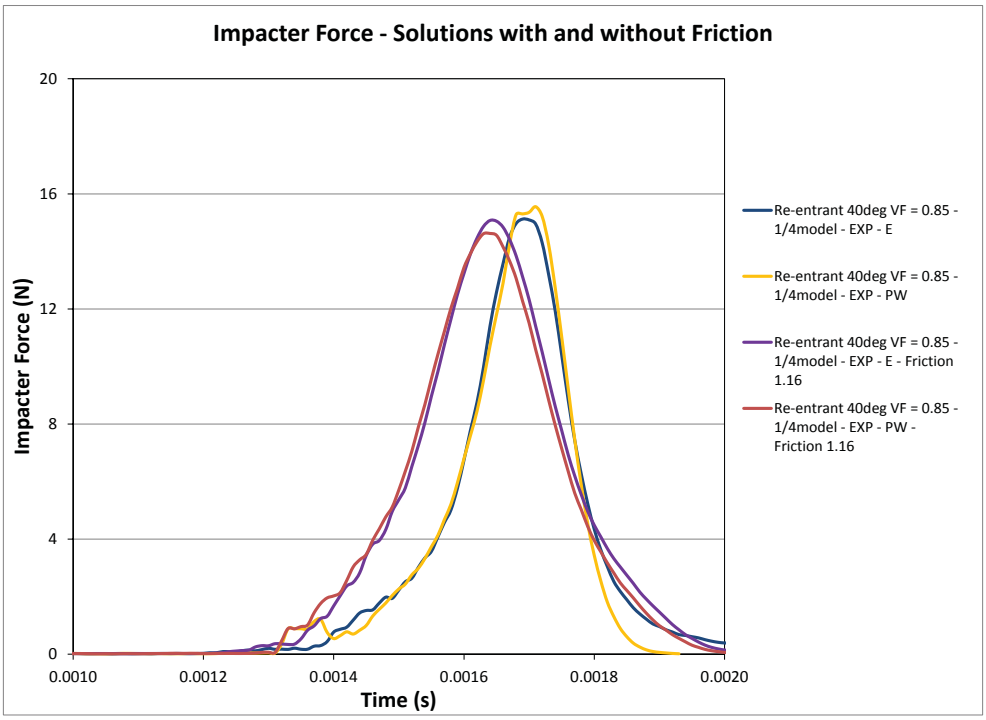

Figure 48: Comparison of impact force time histories for the ¼ test model obtained using the explicit algorithm for elastic and piecewise plastic materials without and with friction.

3 Rerun of the Previous Parametric Study Using the Improved Solution Options

The parametric study with an impacter speed of 10m/s considered previously was re-performed using the recent LS-DYNA solution control parameters identified through the verification study described in the last chapter. This included definitions of contact algorithms, shell formulations, artificial viscosity, frictions between contacting ribs inside the specimens, and parameters related to accuracy control. In addition, the finite element models used in the previous parametric studies were adjusted, so that all models were of the same width and contained 16 columns of unit cells. For easy comparison of results, the heights of the test models with different void fractions were determined to have similar areal densities. The mass of the planar impacter was approximately 100 times of the mass of the specimens. The results from the new parametric study are presented and discussed here.

The predicted deformed configurations of the material specimens at different deformation stages in impact simulations were first examined. Examples taken from four representative cases from the parametric study are presented in Figures 49 to 52. These include vertical and horizontal impacts on regular and re-entrant samples with a void fraction of 0.7 and a geometric angle of 40^{O}. In these figures, the horizontal lines above and below the material samples indicate the planar impacter and the supporting plane, respectively. Both were modelled as rigid plates. The contact between the material samples and the impacter and supporting plane were assumed to be frictionless.

The deformed configurations shown in Figures 49 to 52 indicated that under both vertical and horizontal impact orientations, the conventional honeycomb specimen expanded in the direction perpendicular to the impact direction. However, the re-entrant material contracted in this direction due to its unique effective mechanical property of negative Poisson's ratio. Under impacter speed of 10 m/s, all the specimens were eventually compressed into the fully compact state, where the peak impact forces were generated. The deformed configurations at this state indicated that the true volume of the polymer materials in the specimens was properly preserved in the numerical solutions. Following this fully compact state, the impacter rebounded and the original heights of the material samples were nearly recovered. These predicted deformation sequences agreed well with our expectations and indicated that the numerical solutions were well behaved under the new solution control parameters.

The predicted time histories of impact force and internal energy absorbed by the material samples for all test cases are presented in Figures 53 to 76. In these figures, results obtained for different geometric angle θ are compared for each combination of material type (conventional or re-entrant) and void fraction. The purpose of this arrangement was to show the influence of the angle on the impact properties of the material samples, which is one of the focuses of the present study. The impacter force time histories presented here were evaluated by multiplying the impacter mass and the impacter accelerations that were evaluated by differentiating the impacter displacement time histories generated by LS-DYNA twice. In order to reduce the high-frequency noises in the accelerations, a smoothing algorithm had been applied. The time histories of the polymer internal energy were extracted using the pre- and post-processing code, LS-PREPOST, in the LS-DYNA family.

Examination of these results led to the following general observations:

(1) The impact force time histories obtained from this parametric study consistently showed two distinct phases in the mechanical responses to impact load. At the beginning of the transient, a very low resistance to the impacter was observed. However, at a certain point of time, the resistance to the impacter increased rapidly leading to a peak impact force. After this peak force was reached, the impacter started to rebound and impacter force gradually reduced to zero when the impacter and the sample were completely separated. This predicted mechanical behaviour of the material samples is consistent with the measured effective nonlinear strain-strain properties of the auxetic materials as shown in Figure 77. In this figure, two distinct phases were clearly observed. Among them, the first phase provided a low stiffness which was dominated by the bending deformation of the ribs in the honeycomb materials, whereas the second phase showed a rapid increase of stiffness which happened as the material became more and more compact under large deformations. When all the voids in the material were eliminated, the material became a piece of solid polymer and provided significantly higher stiffness. This nonlinear behaviour is more evident in solutions for re-entrant samples with larger θ values and higher void fractions.

(2) For given void fraction and impact orientation (horizontal or vertical), material samples with larger angle θ normally showed less resistance to the impacter at the beginning of the impact event. This trend is consistent with the effective elastic moduli of both the conventional and re-entrant honeycomb structures presented Table 3 in the phase I report [1] of this contract. Under impact loads, this low resistance at the beginning of the transient let to higher residual impacter speed when the deformation of the sample material entered the second phase of the stress-strain curve, resulting in higher peak forces at a later stage of the impact event. On the other hand, the higher residual impact speed also made the sample material to enter the high stiffness phase at an earlier time as indicated in many figures shown in this chapter.

(3) For given void fraction and angle θ, the material samples with conventional honeycomb structure normally generated higher peak impact force than the re-entrant material samples. This is also consistent with the trend in effective elastic moduli of the conventional and re-entrant honeycomb structures presented in Table 3 in reference [1].

(4) In horizontal impact cases, the times at which the peak impact forces occurred seem to be nearly proportional to the angle θ for both conventional and re-entrant material samples. However, this trend was not observed in cases of vertical impact.

(5) Due to the strain rate effects in the polymer material properties described in [1] and the friction between the contacting ribs, the material behaviour of the specimens was nearly elastic. This is evident from the polymer internal energy profiles which showed the internal energy in the material samples increases to a peak value when the maximum displacement of the impacter was reached where the impact force reaches its maximum value, and then start to decrease to nearly zero upon the release of the impacter. This nearly elastic response should represent the physical behaviour of the polymer foams reasonably well.

(6) For vertical impact, the peak internal energy decreases with the increase of θ. However, the opposite trend was observed for horizontal impact.

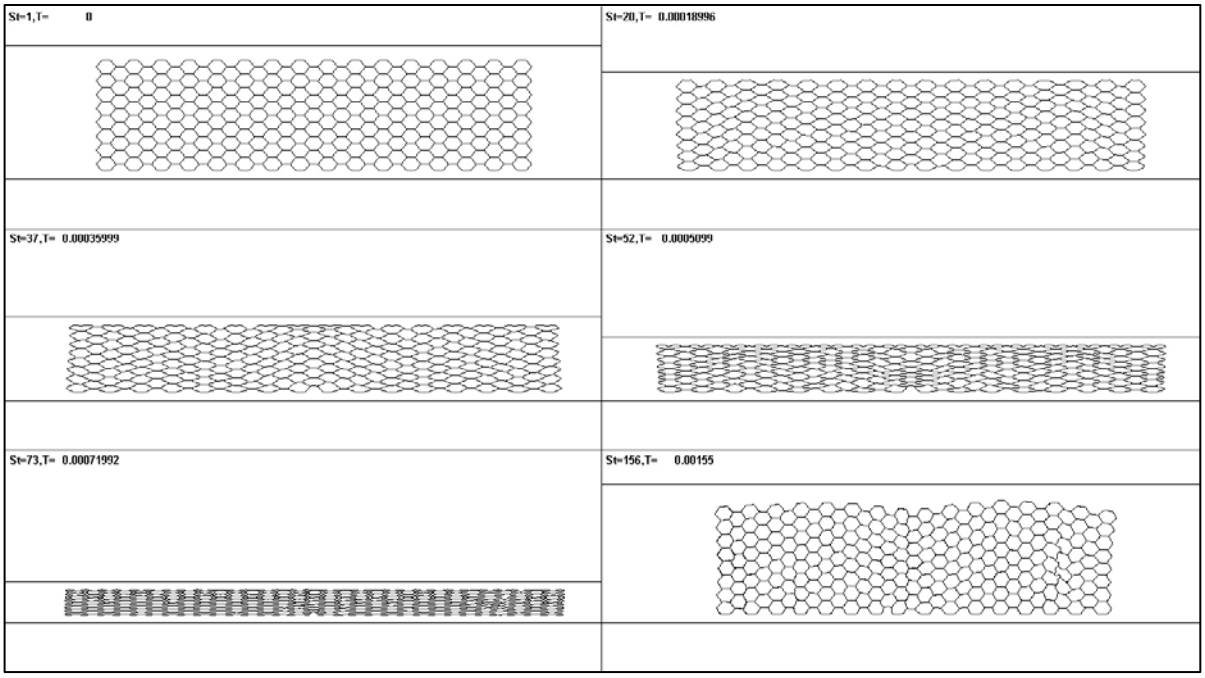

Figure 49: Original and deformed configurations of a regular honeycomb specimen (VF=0.7, θ=40^o) under vertical impact of a planar impacter with an initial speed of 10 m/s.

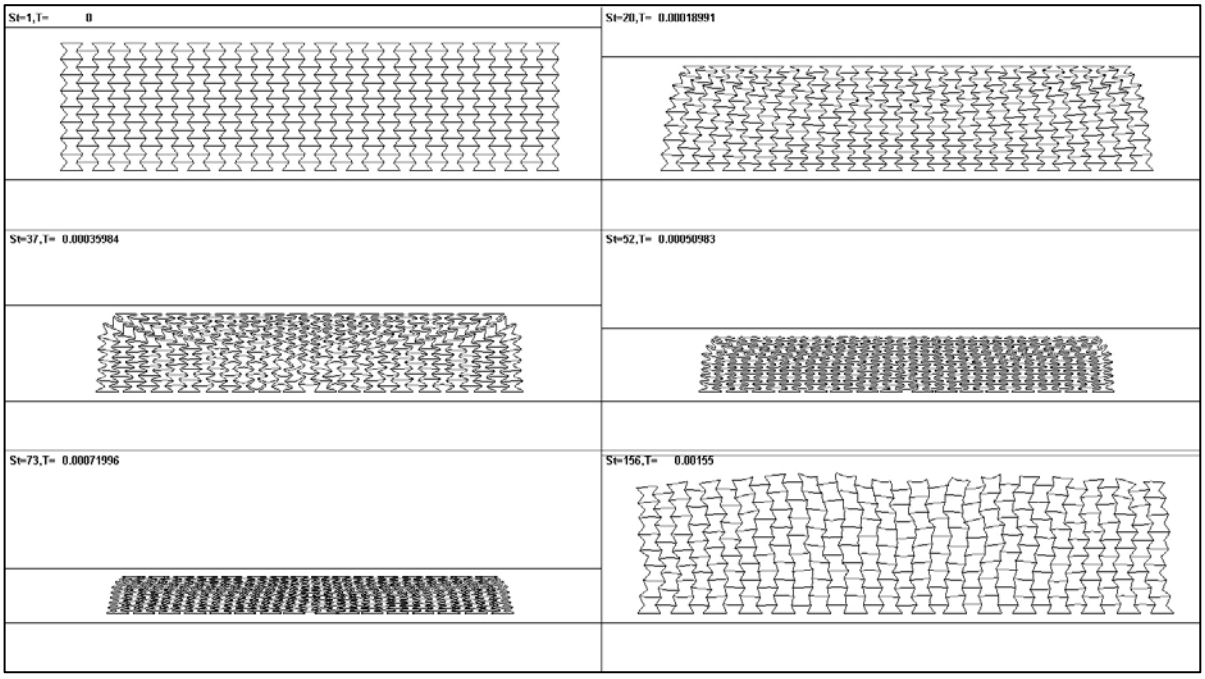

Figure 50: Original and deformed configurations of a re-entrant honeycomb specimen (VF=0.7, θ=40^o) under vertical impact of a planar impacter with an initial speed of 10 m/s.

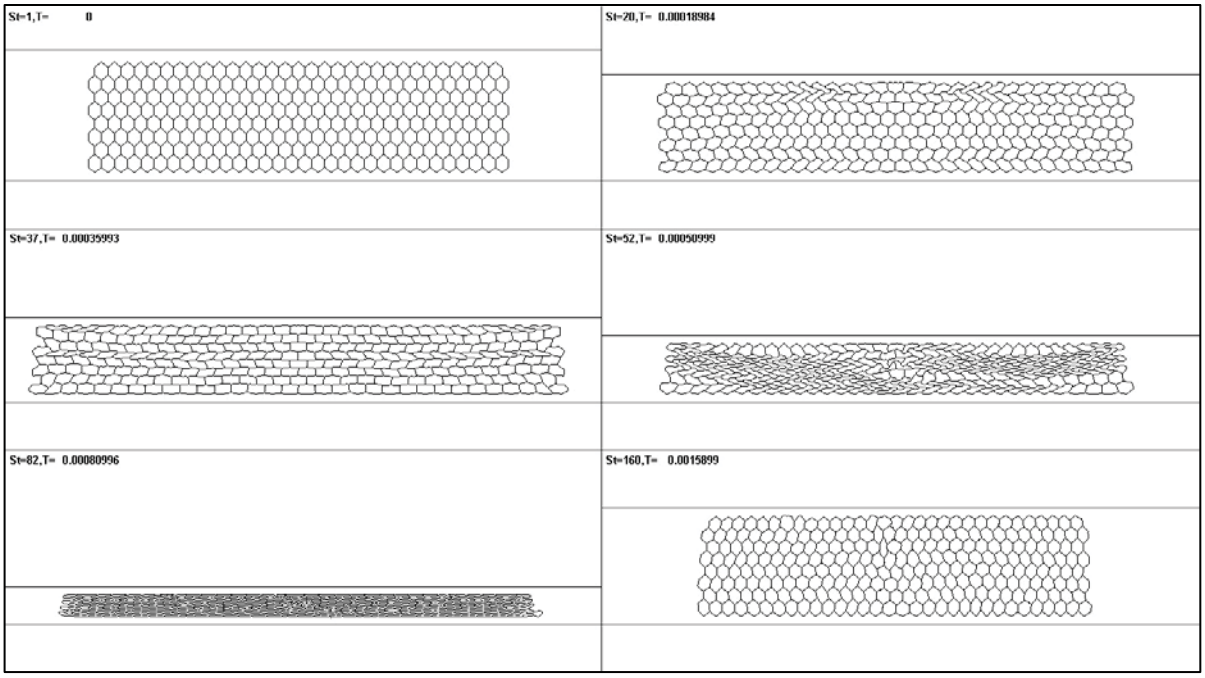

Figure 51: Original and deformed configurations of a regular honeycomb specimen (VF=0.7, θ=40°) under horizontal impact of a planar impacter with an initial speed of 10 m/s.

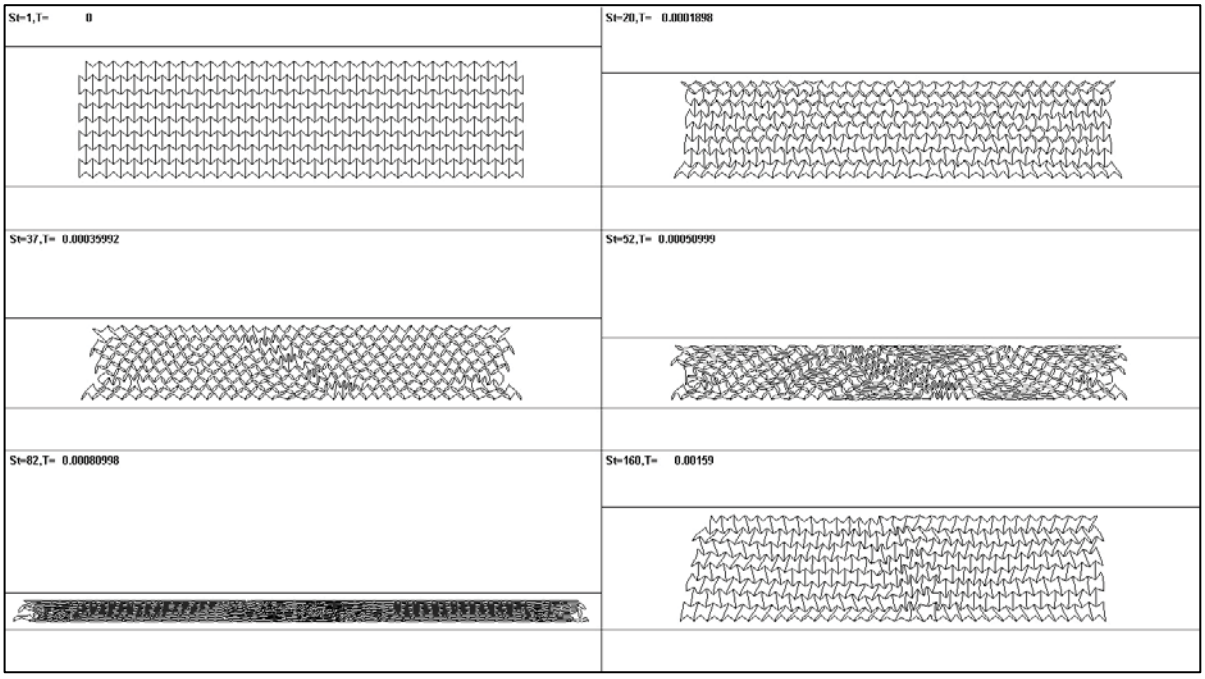

Figure 52: Original and deformed configurations of a re-entrant honeycomb specimen (VF=0.7, θ=40°) under horizontal impact of a planar impacter with an initial speed of 10 m/s.

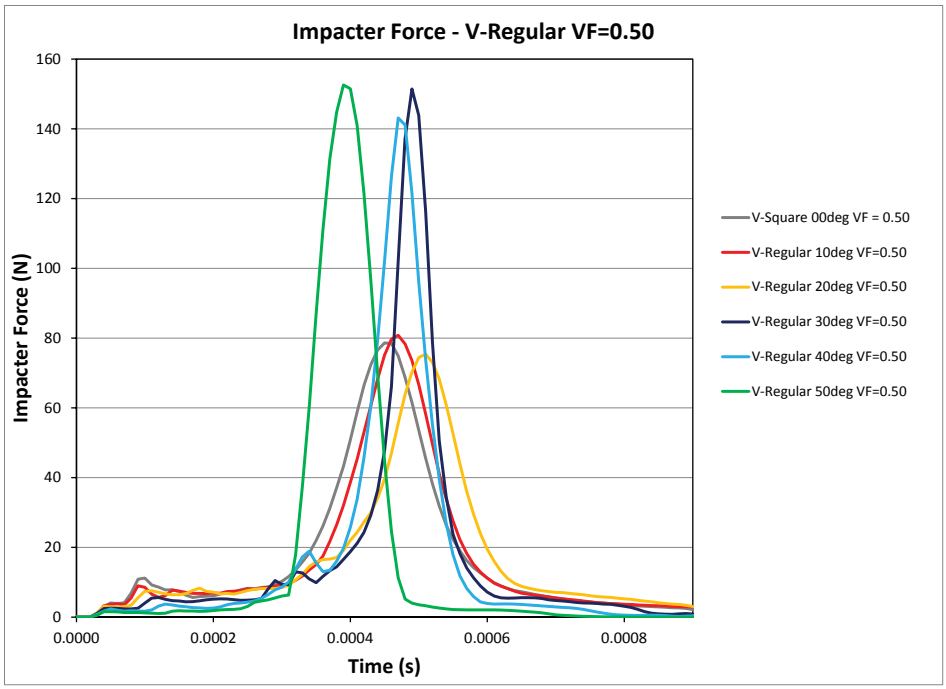

Figure 53: Impact force time histories obtained using the new solution parameters for vertical impact of a planar impacter at 10 m/s on regular honeycomb specimens with void fraction of 0.5 and different angles.

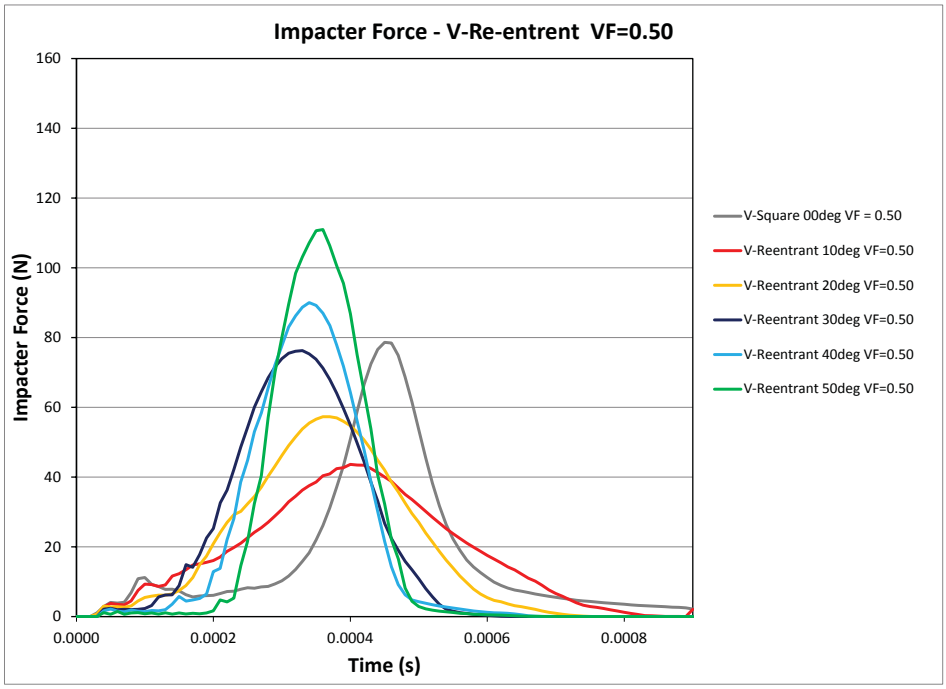

Figure 54: Impact force time histories obtained using the new solution parameters for vertical impact of a planar impacter at 10 m/s on re-entrant honeycomb specimens with void fraction of 0.5 and different angles.

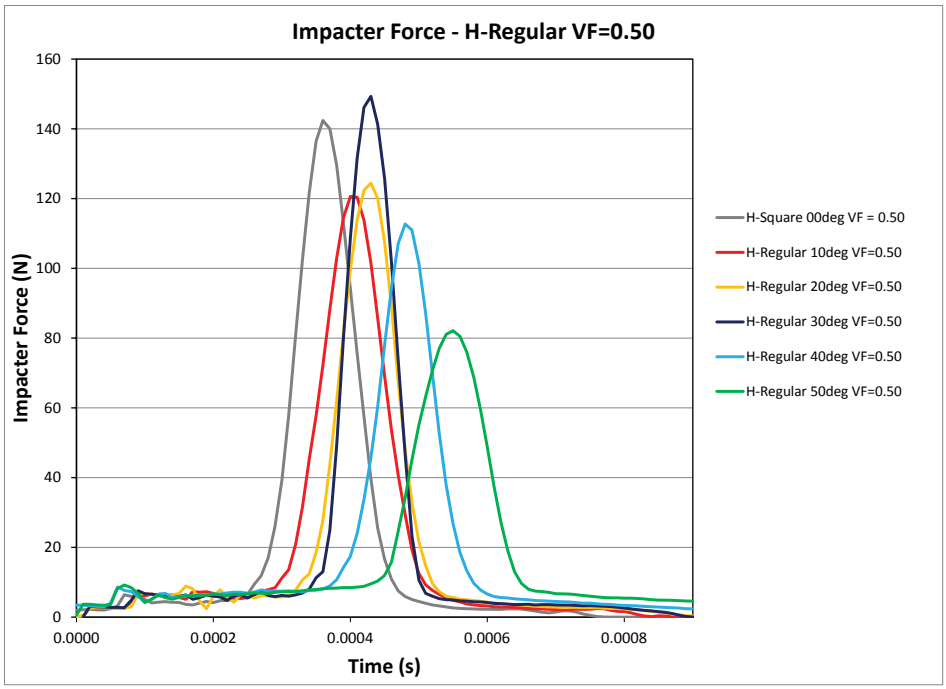

Figure 55: Impact force time histories obtained using the new solution parameters for horizontal impact of a planar impacter at 10 m/s on regular honeycomb specimens with void fraction of 0.5 and different angles.

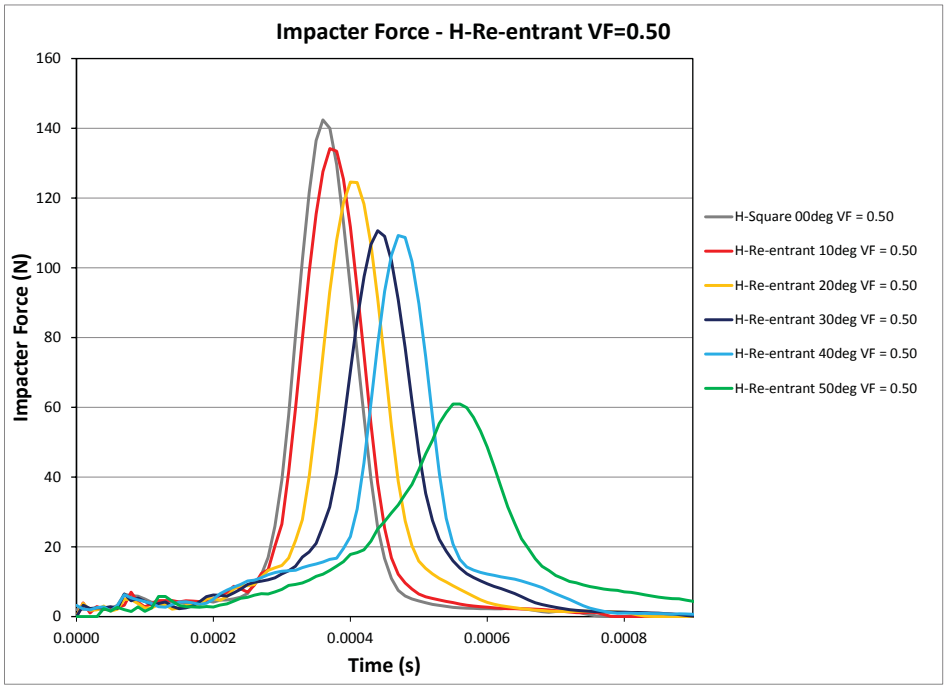

Figure 56: Impact force time histories obtained using the new solution parameters for horizontal impact of a planar impacter at 10 m/s on re-entrant honeycomb specimens with void fraction of 0.5 and different angles.

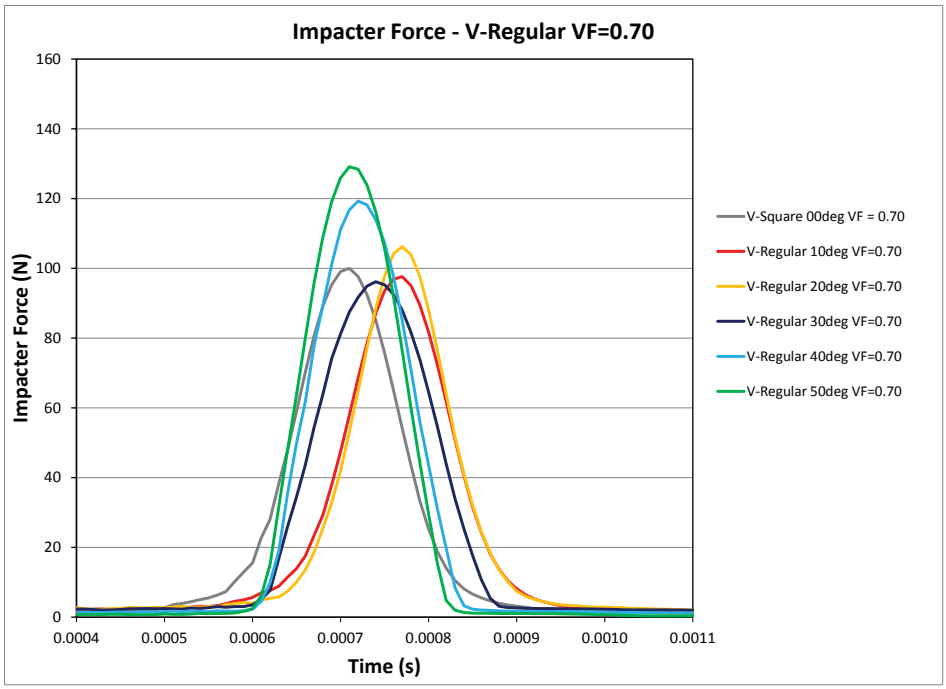

Figure 57: Impact force time histories obtained using the new solution parameters for vertical impact of a planar impacter at 10 m/s on regular honeycomb specimens with void fraction of 0.7 and different angles.

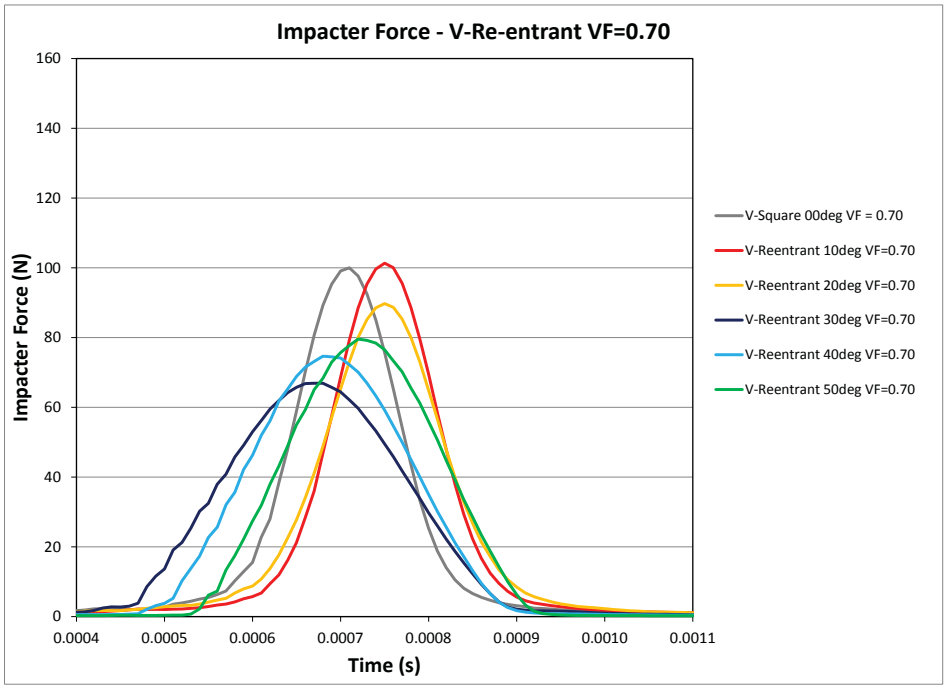

Figure 58: Impact force time histories obtained using the new solution parameters for vertical impact of a planar impacter at 10 m/s on re-entrant honeycomb specimens with void fraction of 0.7 and different angles.

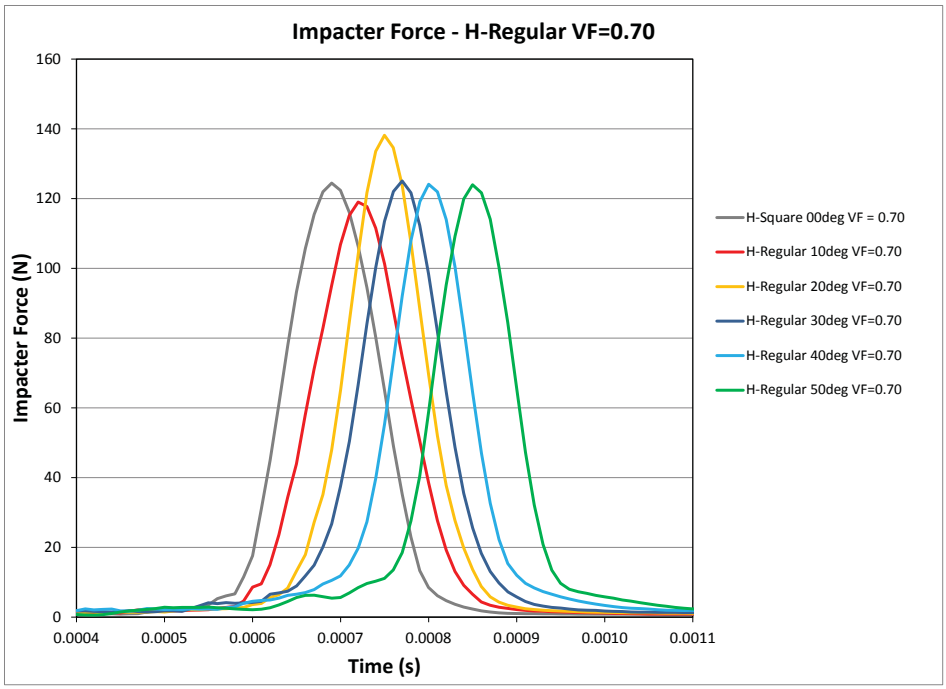

Figure 59: Impact force time histories obtained using the new solution parameters for horizontal impact of a planar impacter at 10 m/s on regular honeycomb specimens with void fraction of 0.7 and different angles.

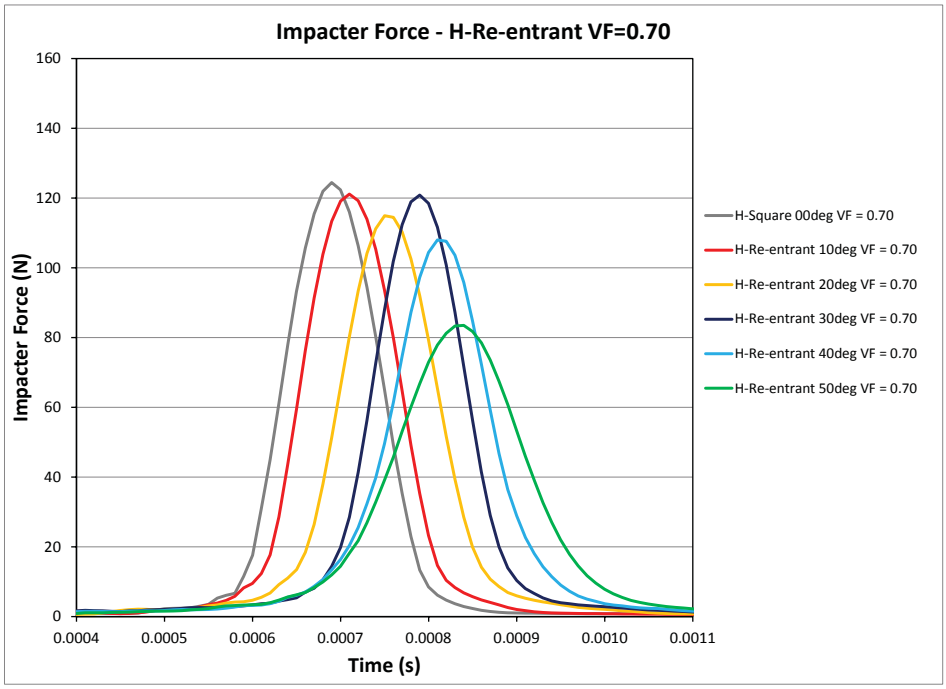

Figure 60: Impact force time histories obtained using the new solution parameters for horizontal impact of a planar impacter at 10 m/s on re-entrant honeycomb specimens with void fraction of 0.7 and different angles.

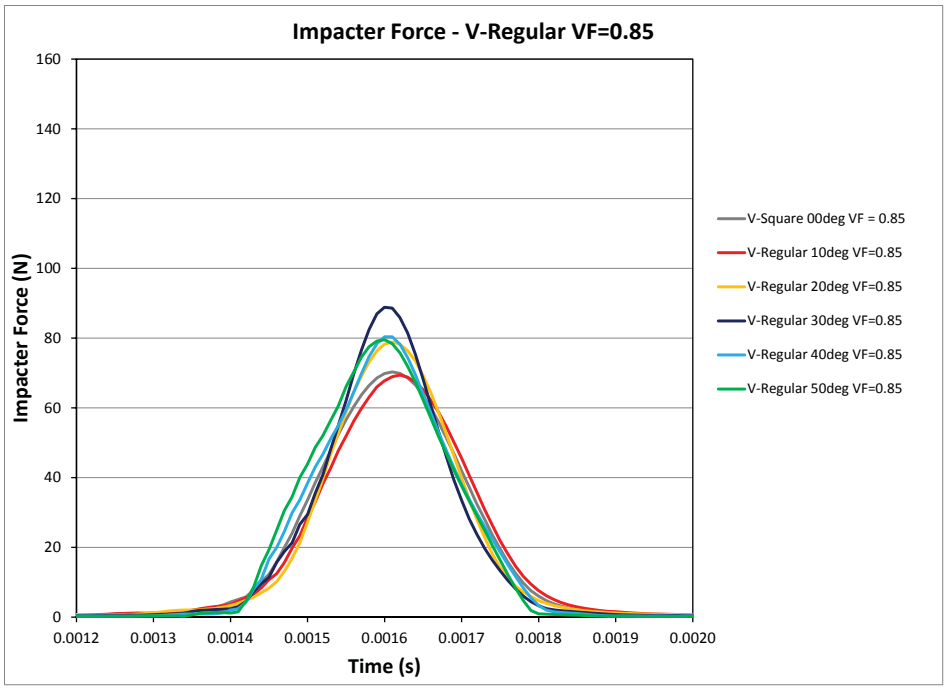

Figure 61: Impact force time histories obtained using the new solution parameters for vertical impact of a planar impacter at 10 m/s on regular honeycomb specimens with void fraction of 0.85 and different angles.

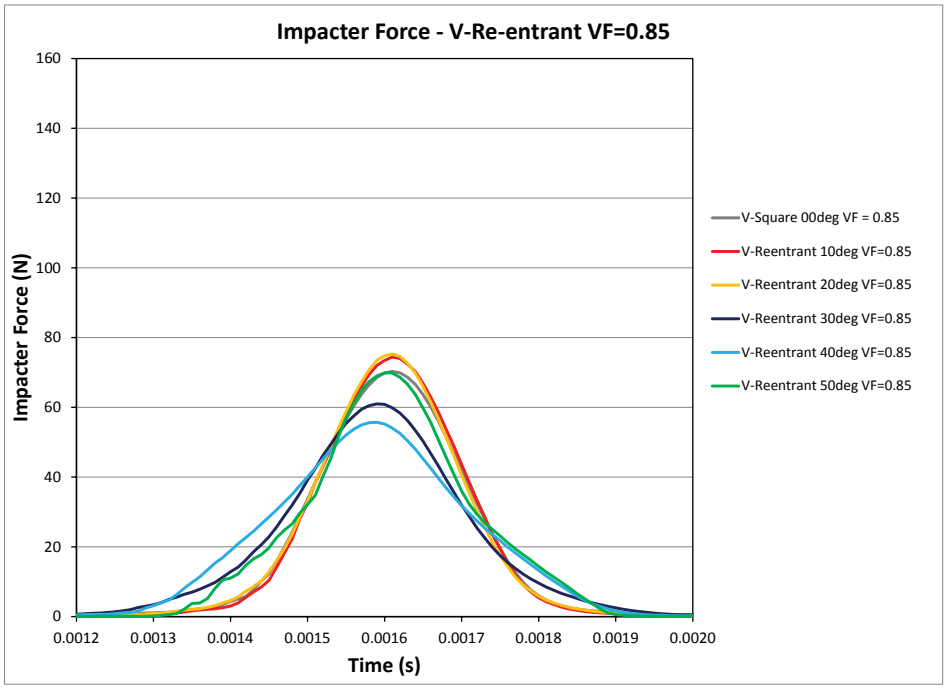

Figure 62: Impact force time histories obtained using the new solution parameters for vertical impact of a planar impacter at 10 m/s on re-entrant honeycomb specimens with void fraction of 0.85 and different angles.

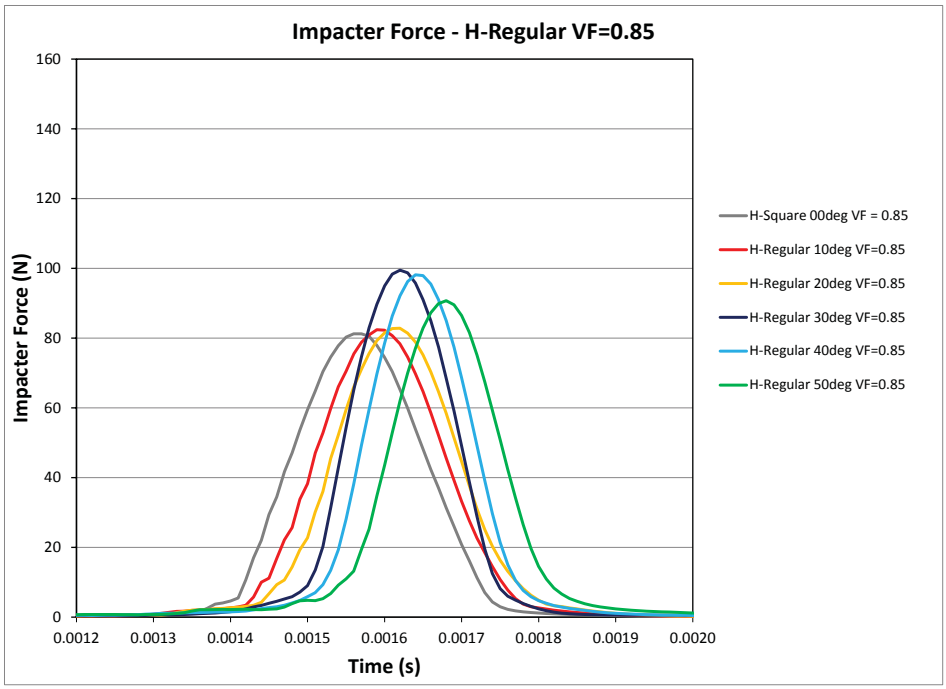

Figure 63: Impact force time histories obtained using the new solution parameters for horizontal impact of a planar impacter at 10 m/s on regular honeycomb specimens with void fraction of 0.85 and different angles.

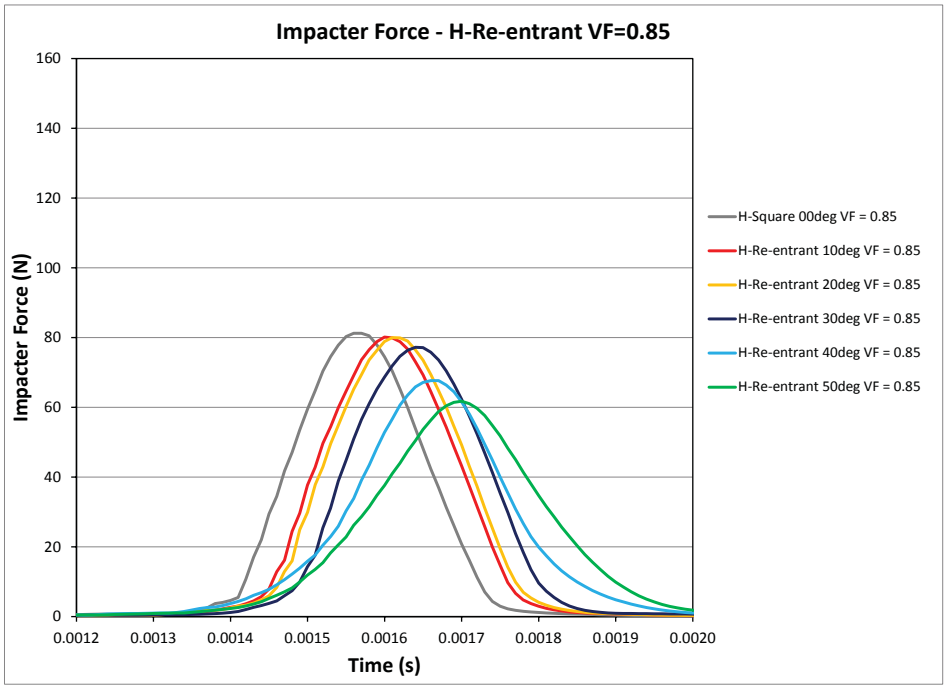

Figure 64: Impact force time histories obtained using the new solution parameters for horizontal impact of a planar impacter at 10 m/s on re-entrant honeycomb specimens with void fraction of 0.85 and different angles.

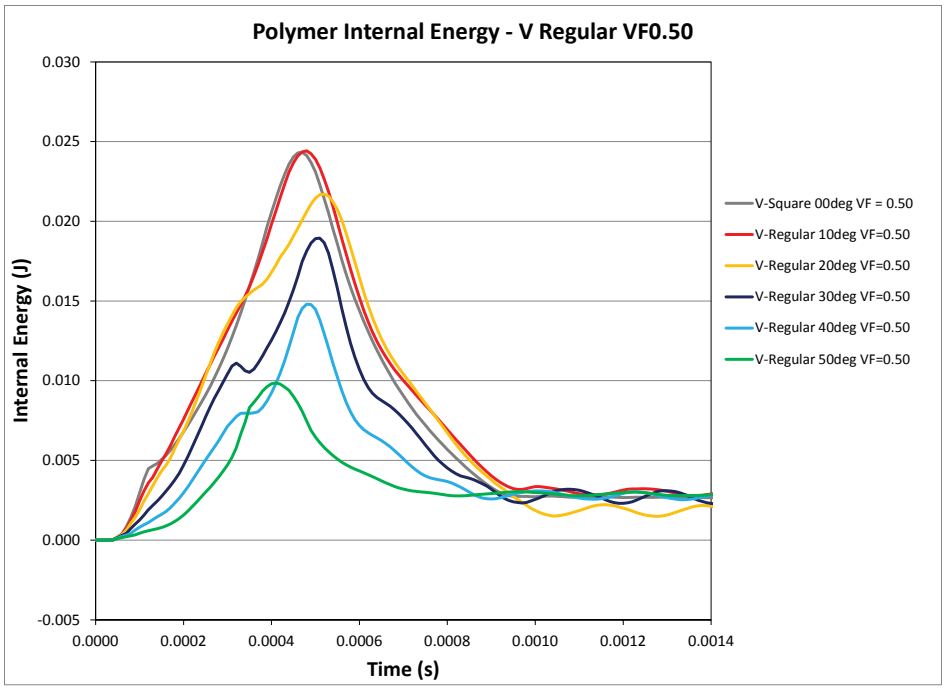

Figure 65: Internal energy time histories obtained using the new solution parameters for vertical impact of a planar impacter at 10 m/s on regular honeycomb specimens with void fraction of 0.5 and different angles.

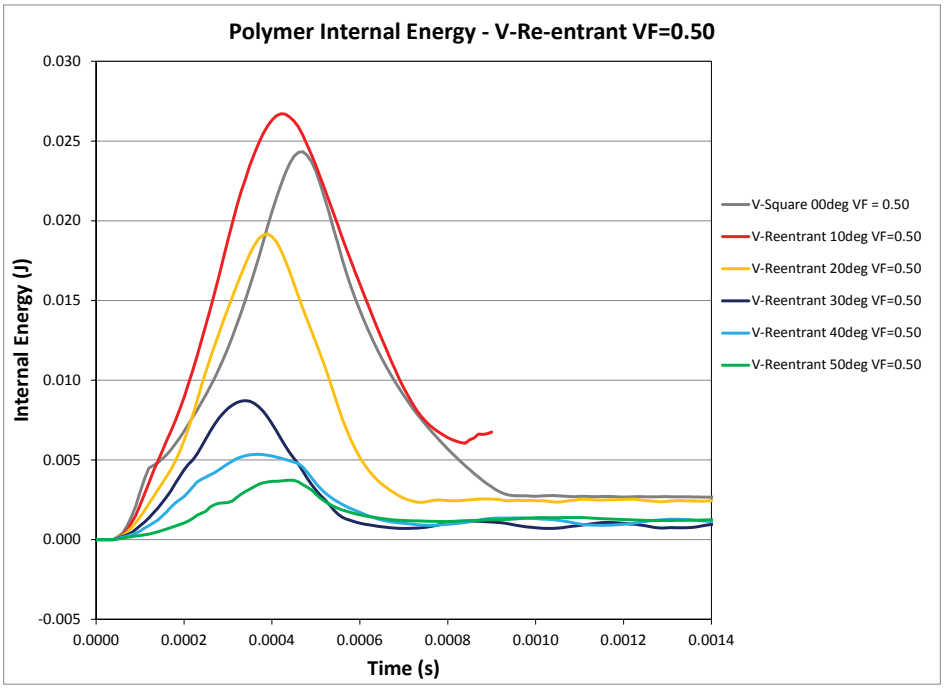

Figure 66: Internal energy time histories obtained using the new solution parameters for vertical impact of a planar impacter at 10 m/s on re-entrant honeycomb specimens with void fraction of 0.5 and different angles.

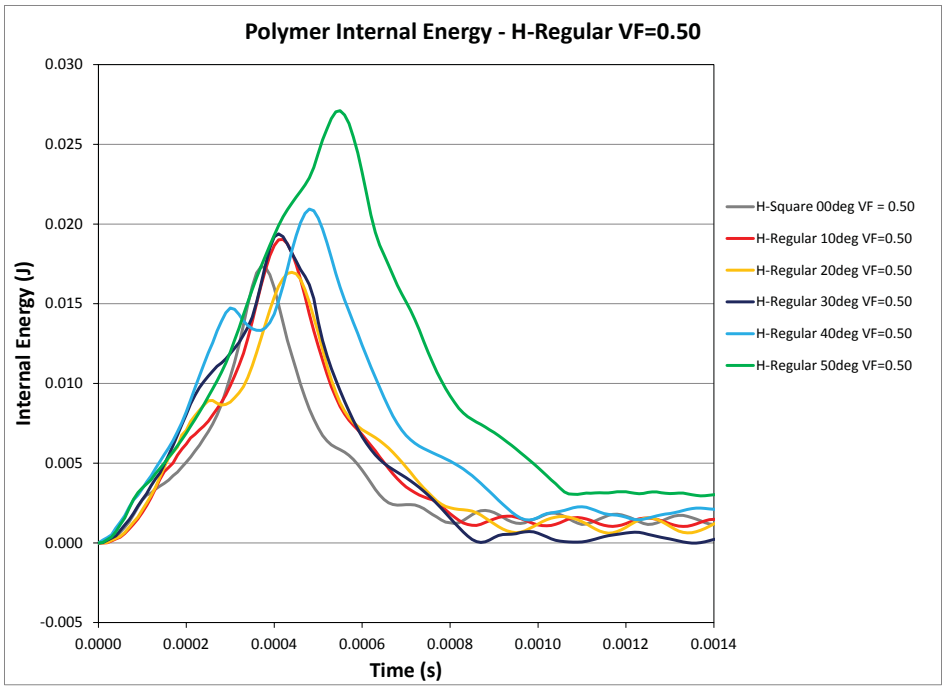

Figure 67: Internal energy time histories obtained using the new solution parameters for horizontal impact of a planar impacter at 10 m/s on regular honeycomb specimens with void fraction of 0.5 and different angles.

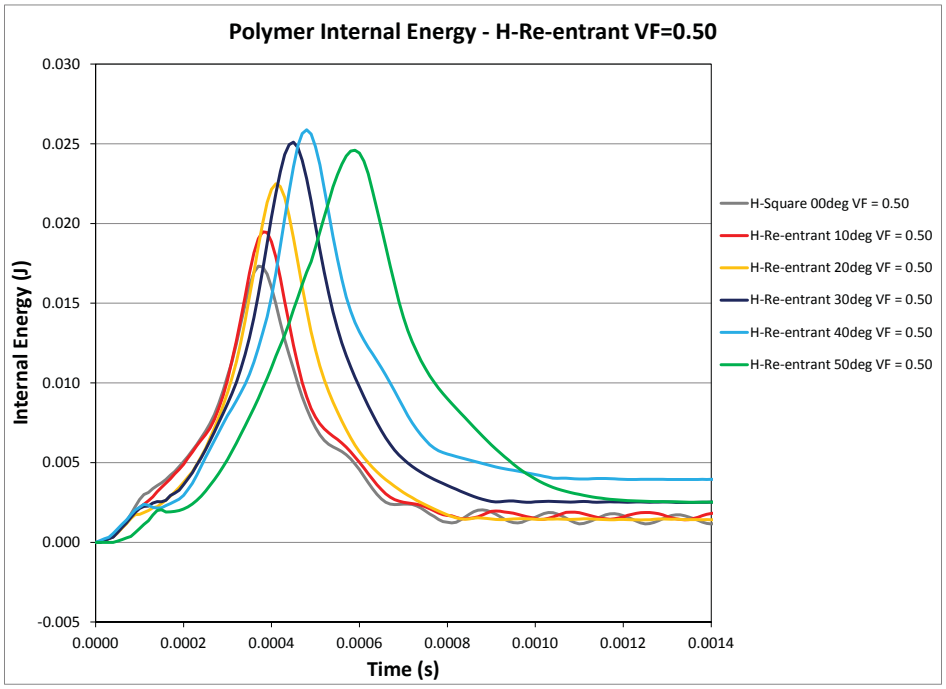

Figure 68: Internal energy time histories obtained using the new solution parameters for horizontal impact of a planar impacter at 10 m/s on re-entrant honeycomb specimens with void fraction of 0.5 and different angles.

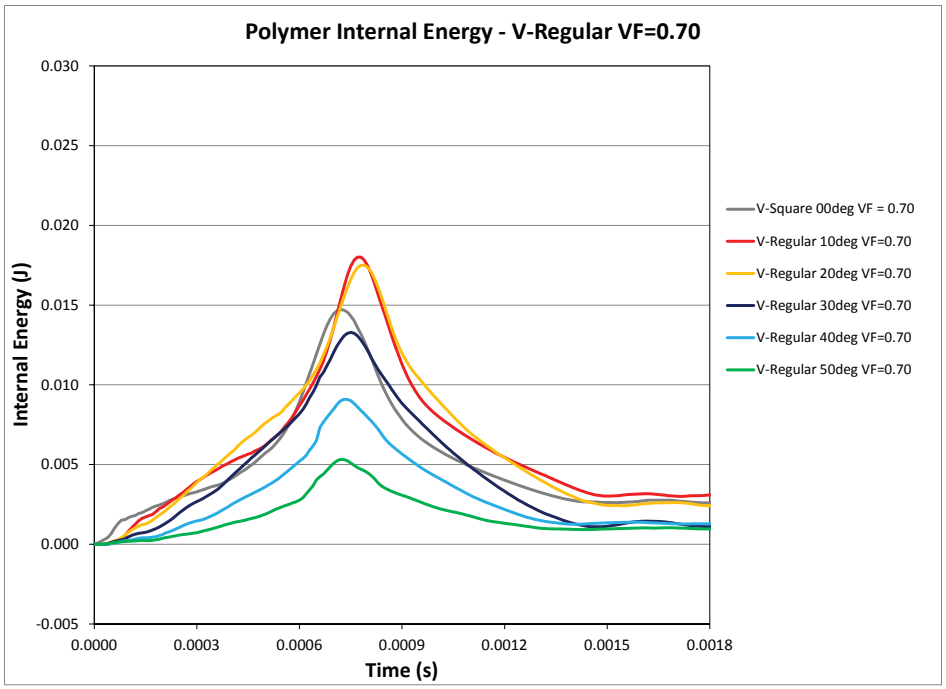

Figure 69: Internal energy time histories obtained using the new solution parameters for vertical impact of a planar impacter at 10 m/s on regular honeycomb specimens with void fraction of 0.7 and different angles.

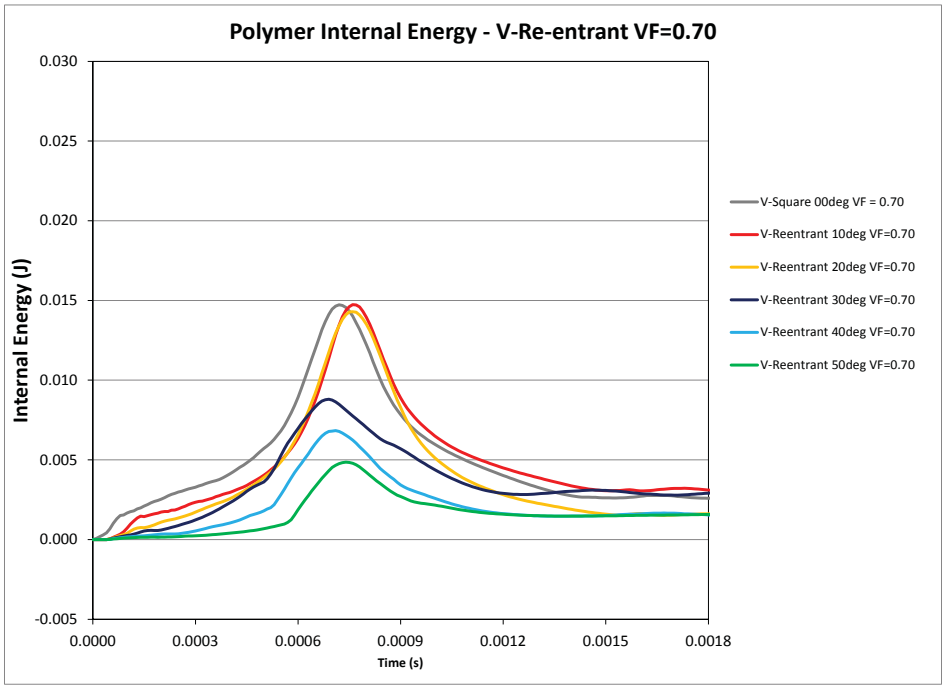

Figure 70: Internal energy time histories obtained using the new solution parameters for vertical impact of a planar impacter at 10 m/s on re-entrant honeycomb specimens with void fraction of 0.7 and different angles.

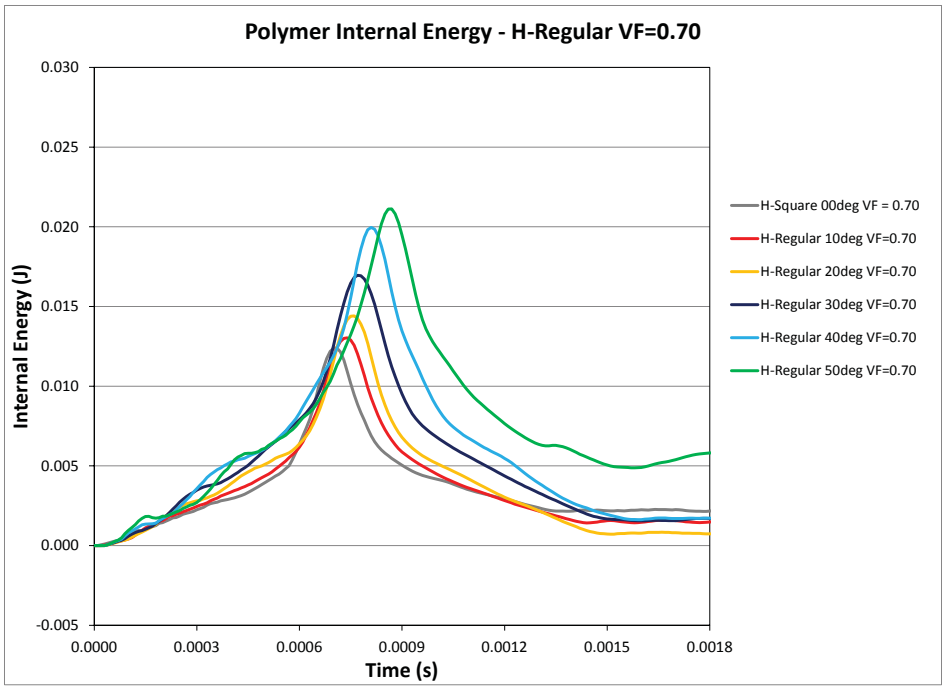

Figure 71: Internal energy time histories obtained using the new solution parameters for horizontal impact of a planar impacter at 10 m/s on regular honeycomb specimens with void fraction of 0.7 and different angles.

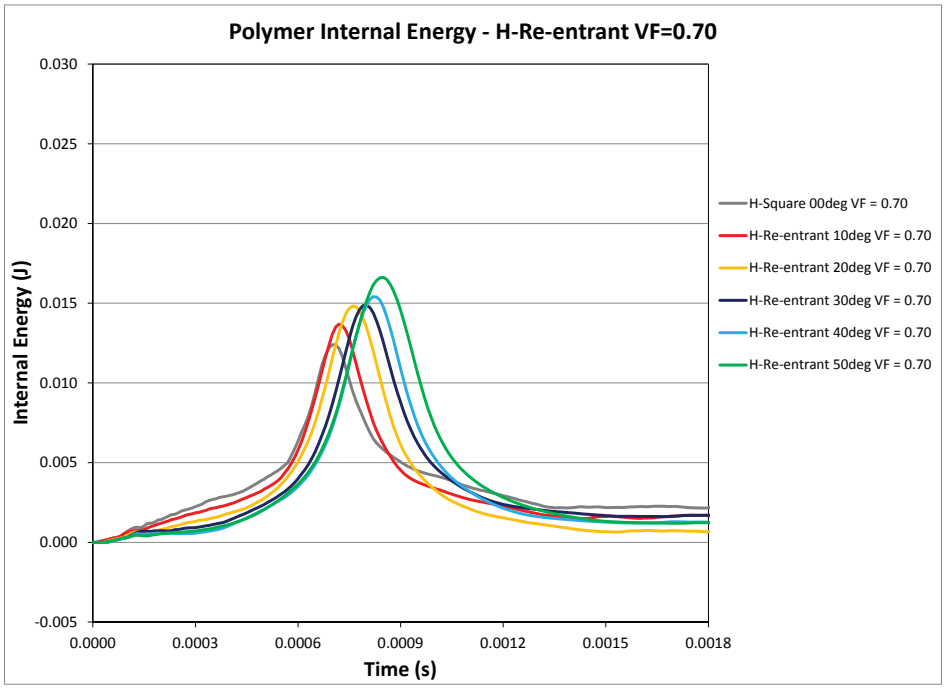

Figure 72: Internal energy time histories obtained using the new solution parameters for horizontal impact of a planar impacter at 10 m/s on re-entrant honeycomb specimens with void fraction of 0.7 and different angles.

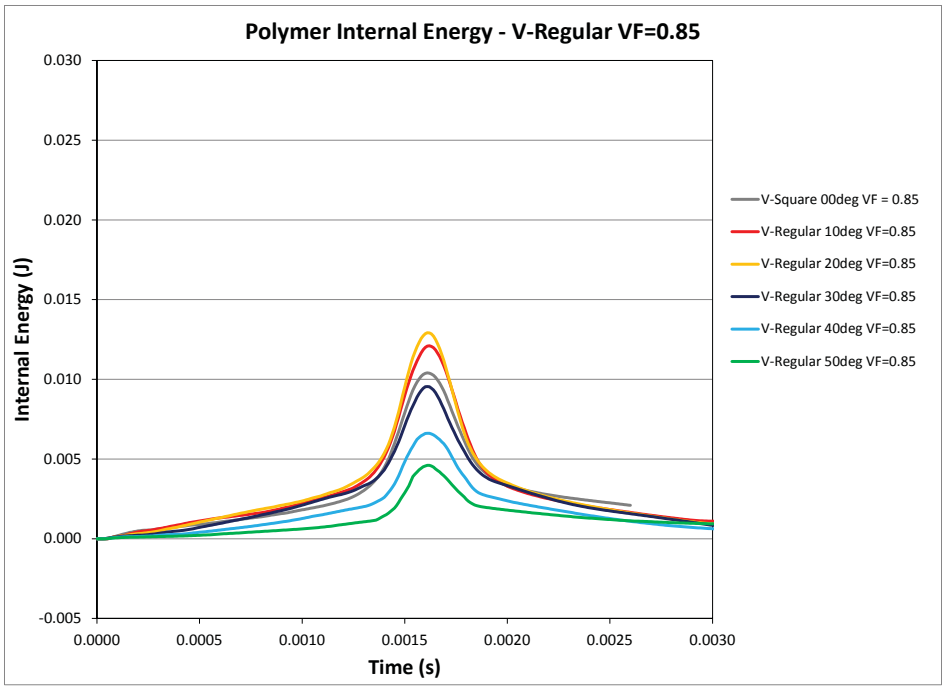

Figure 73: Internal energy time histories obtained using the new solution parameters for vertical impact of a planar impacter at 10 m/s on regular honeycomb specimens with void fraction of 0.85 and different angles.

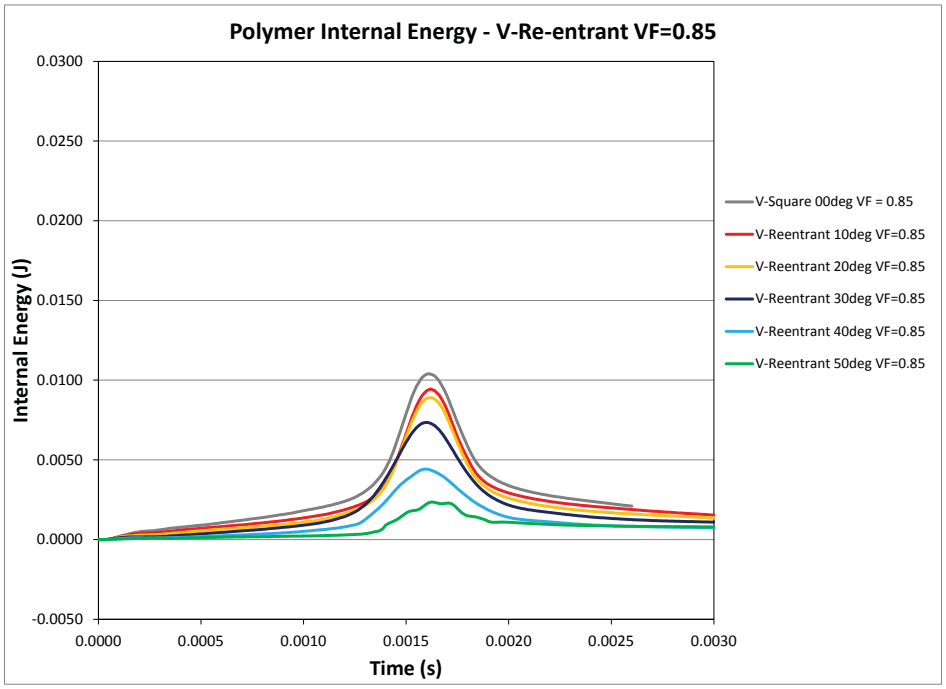

Figure 74: Internal energy time histories obtained using the new solution parameters for vertical impact of a planar impacter at 10 m/s on re-entrant honeycomb specimen with void fraction of 0.85 and different angles.

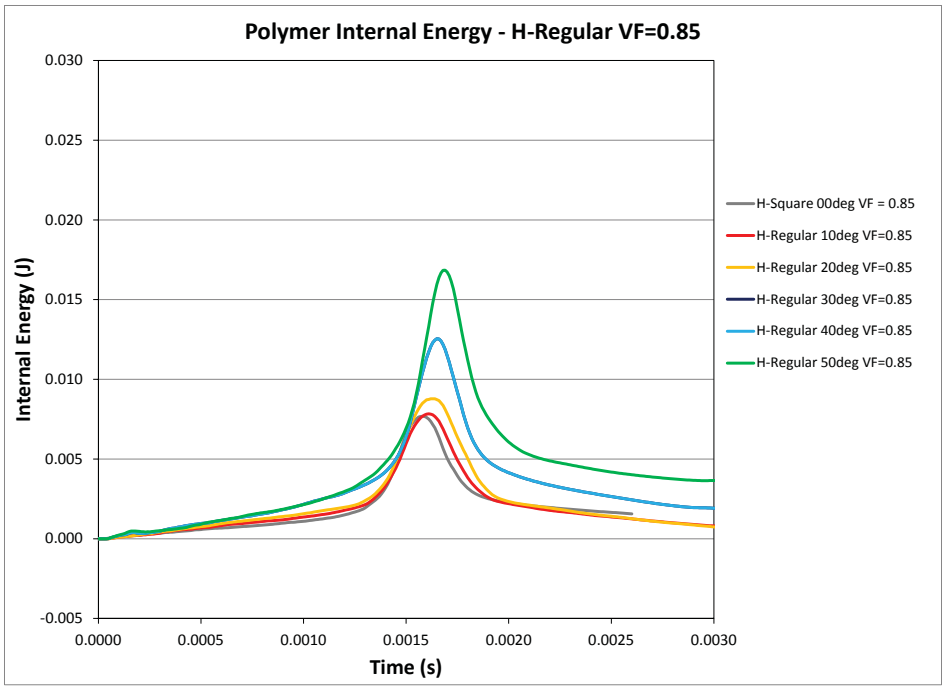

Figure 75: Internal energy time histories obtained using the new solution parameters for horizontal impact of a planar impacter at 10 m/s on regular honeycomb specimens with void fraction of 0.85 and different angles.

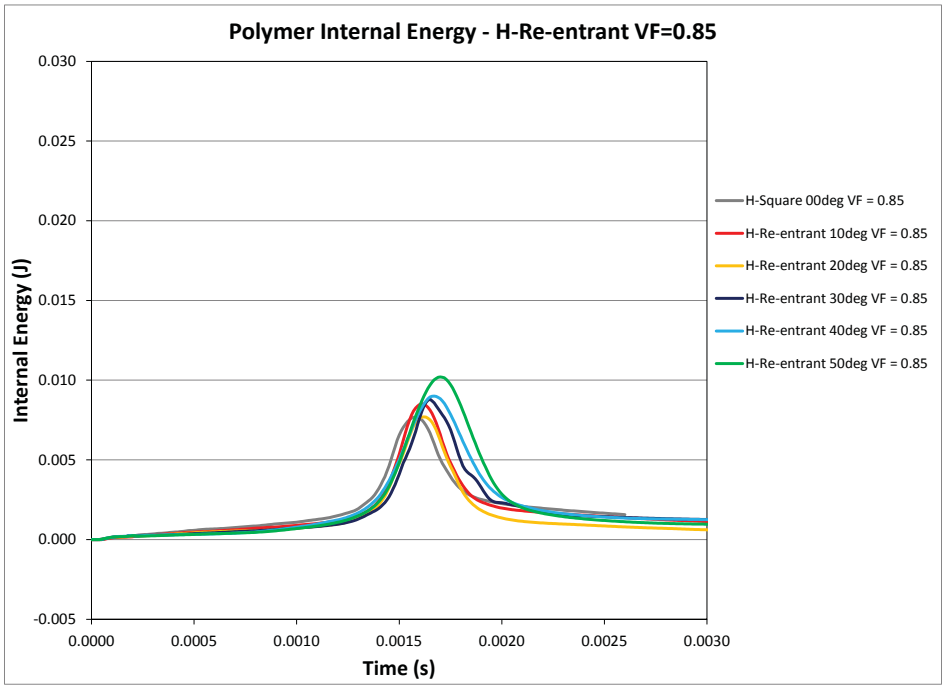

Figure 76: Internal energy time histories obtained using the new solution parameters for horizontal impact of a planar impacter at 10 m/s on re-entrant honeycomb specimens with void fraction of 0.85 and different angles.

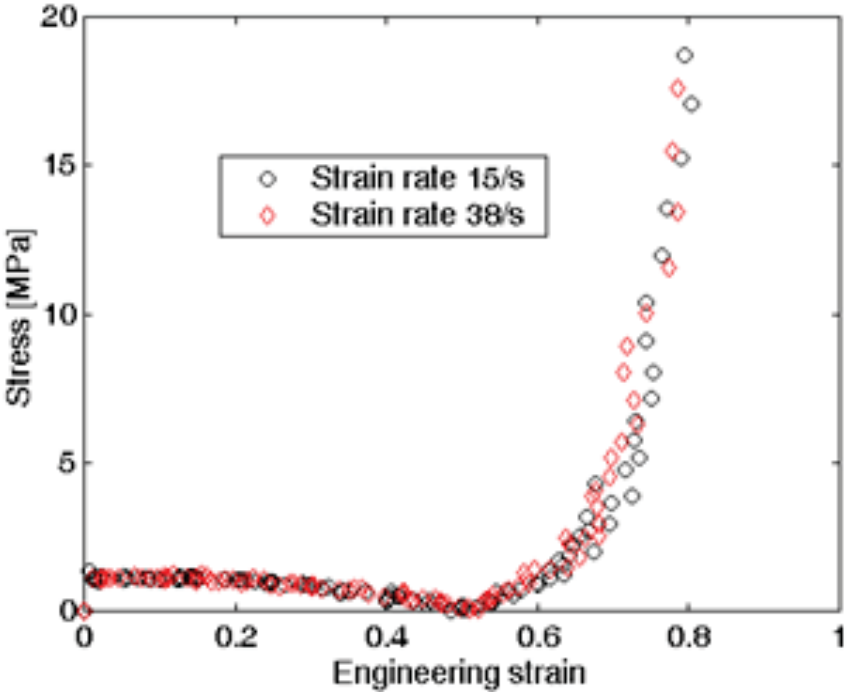

Figure 77: Experimentally measured stress-strain curves for a typical auxetic foam at different strain rates. (Re-produced from Reference [6])

4 Parametric Study Involving Partial Compression of Auxetic Materials Subject to Impact of a Planar Impacter

In the previous parametric study, the material samples were loaded beyond the fully compact state. However, in real applications of the auxetic foam as a protection layer, the material should operate in the range before it becomes fully compact. In order to investigate the mechanical behaviour of the auxetic material in this target deformation range, a parametric study using a reduced impact velocity was designed and conducted.

In order to determine the desired initial velocity of the impacter, a series of numerical simulations were first conducted using a representative model from the previous parametric study. For this purpose, the models with a void fraction of 0.7 and an angle of 40^{O} were utilized, and the original impact velocity of 10 m/s was gradually reduced until the desired responses were obtained. This numerical study concluded that an initial impact velocity of 2 m/s satisfied this requirement. Other than the impacter velocity, the models used in the present parametric study were identical to those utilized in the previous parametric studies. As indicated in Figures 78 to 81, the reduced impacter velocity resulted in partial compression of the material samples under both vertical and horizontal impacts. However, for some material samples with higher void fraction, say 0.85, this reduced impact velocity still caused full compression of the specimens, as shown in Figures 82 and 83, resulting in large peaks in impact force time histories. This phenomenon will be discussed further later in this chapter.

The predicted time histories of impact force and polymer internal energy for all cases considered in this parametric study are presented in Figures 88 to 111. The results are grouped in the same format as in the previous chapter to show the influence of the angle θ on the impact properties of the various conventional and re-entrant material samples. For cases containing large peaks, zoom-in plots are provided show the details at the beginning of the transient.

These results indicated that under vertical impact, conventional and re-entrant material samples with larger geometric angle θ provided lower initial stiffness. This is again consistent with the trend observed in effective elastic moduli given in Table 3 of reference [1]. For materials with larger θ, the lower initial stiffness resulted in lower resistance to the impacter at the beginning of the transient and slower deceleration of the impacter. For this reason, the impacter took a longer time to rebound, resulting in longer impact duration. In some cases, especially for re-entrant materials with larger geometric angle θ, the low initial stiffness caused the material response to enter the high stiffness phase, as indicated in Figure 77, leading to large peaks in the impact force time histories.

Under horizontal impact, the results for re-entrant material samples still showed decreased initial stiffness with the increase of angle θ. However, an opposite trend was observed in the results for the conventional materials. This is inconsistent with the trend observed in the effective elastic moduli. However, we noticed that the effective elastic moduli were derived using linear elastic theory, but this phenomenon could be a consequence of the complicated nonlinear deformations.

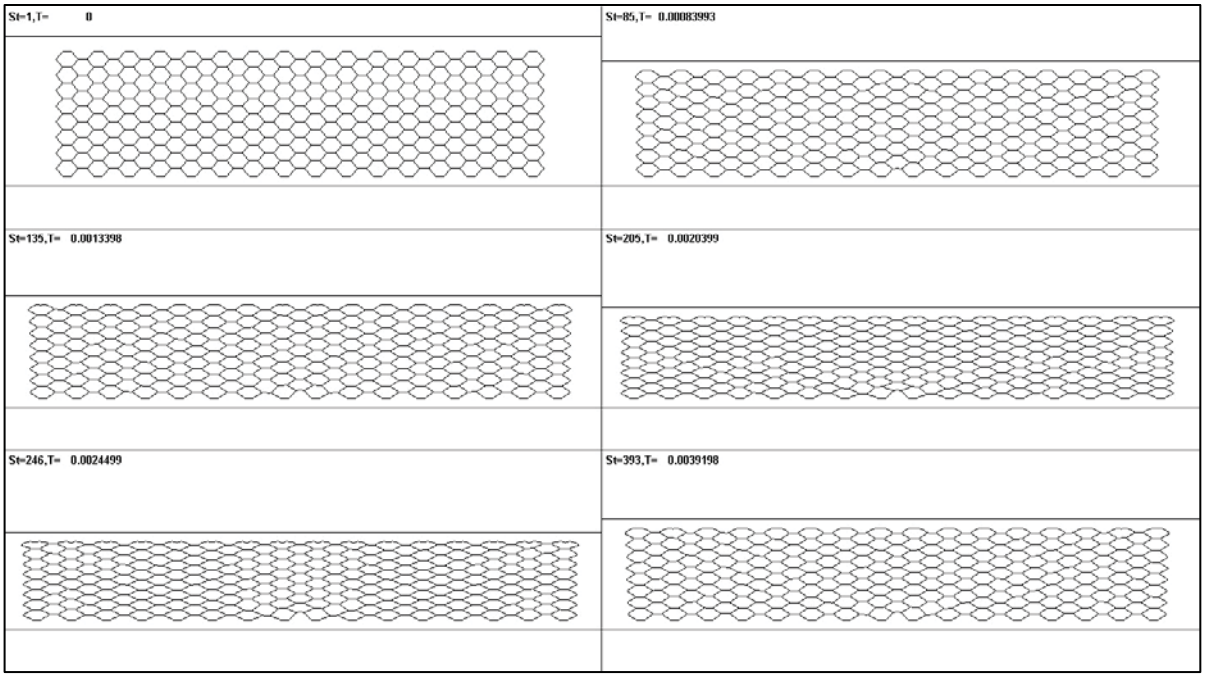

Figure 78: Original and deformed configurations of a regular honeycomb specimen (VF=0.7, θ=40°) under vertical impact of a planar impacter with an initial speed of 2m/s.

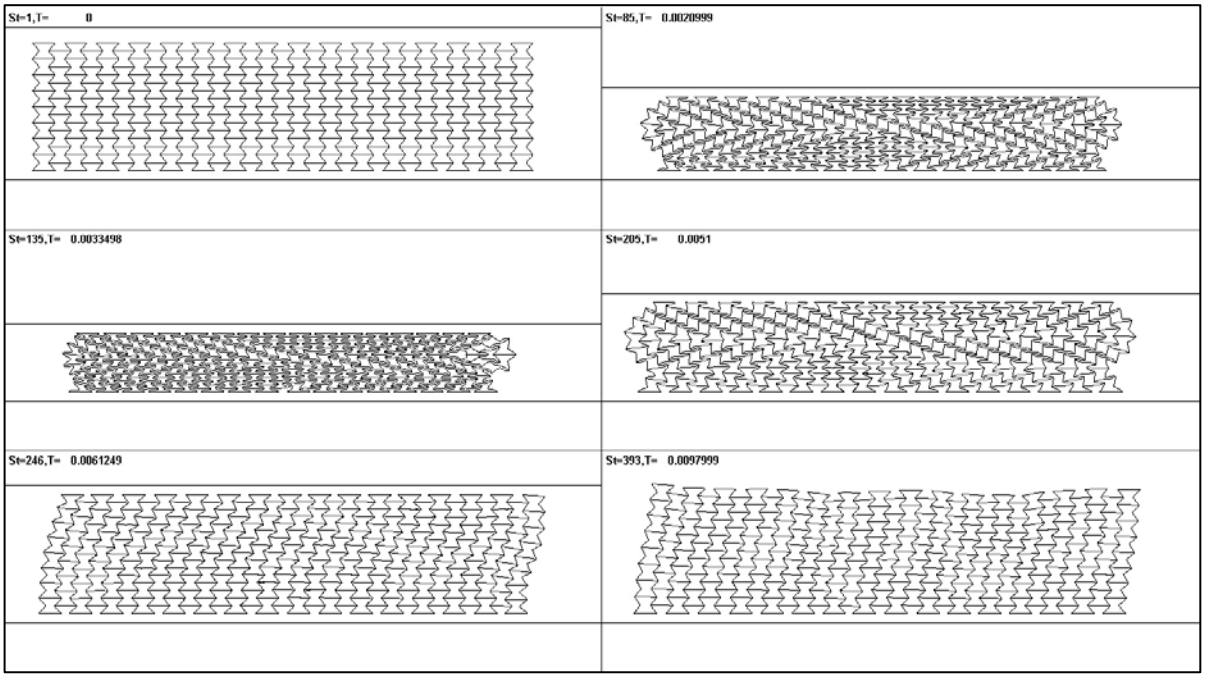

Figure 79: Original and deformed configurations of a re-entrant honeycomb specimen (VF=0.7, θ=40°) under vertical impact of a planar impacter with an initial speed of 2m/s.

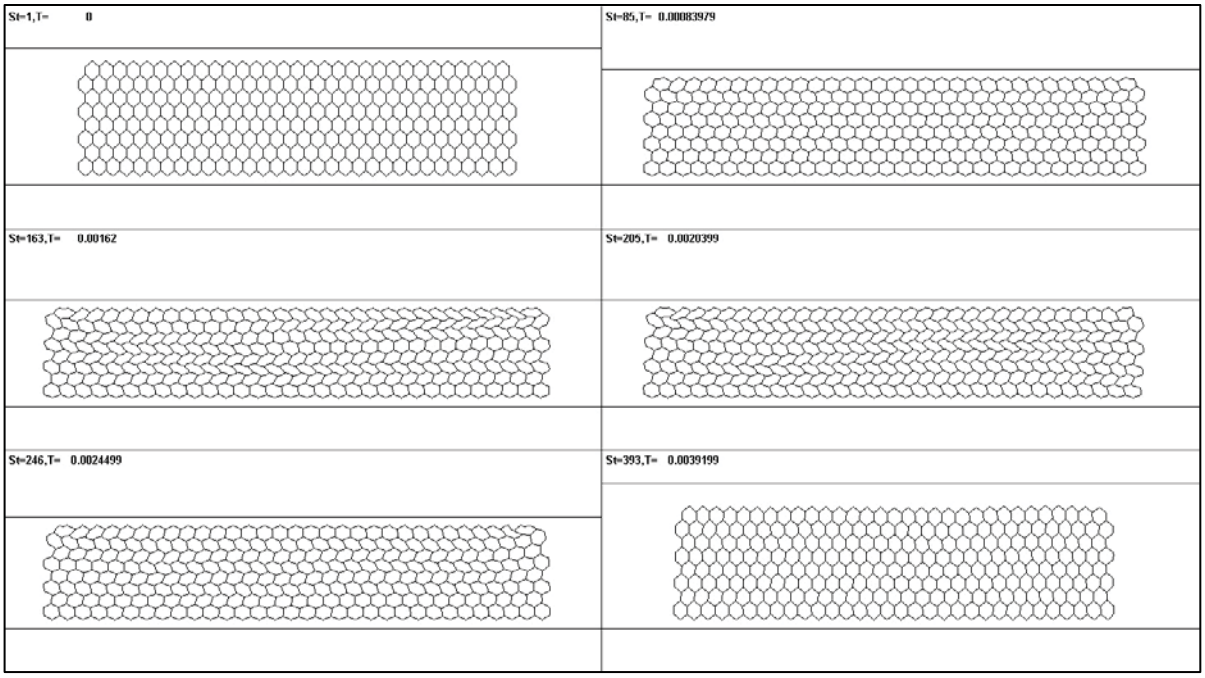

Figure 80: Original and deformed configurations of a regular honeycomb specimen (VF=0.7, θ=40^o) under horizontal impact of a planar impacter with an initial speed of 2m/s.

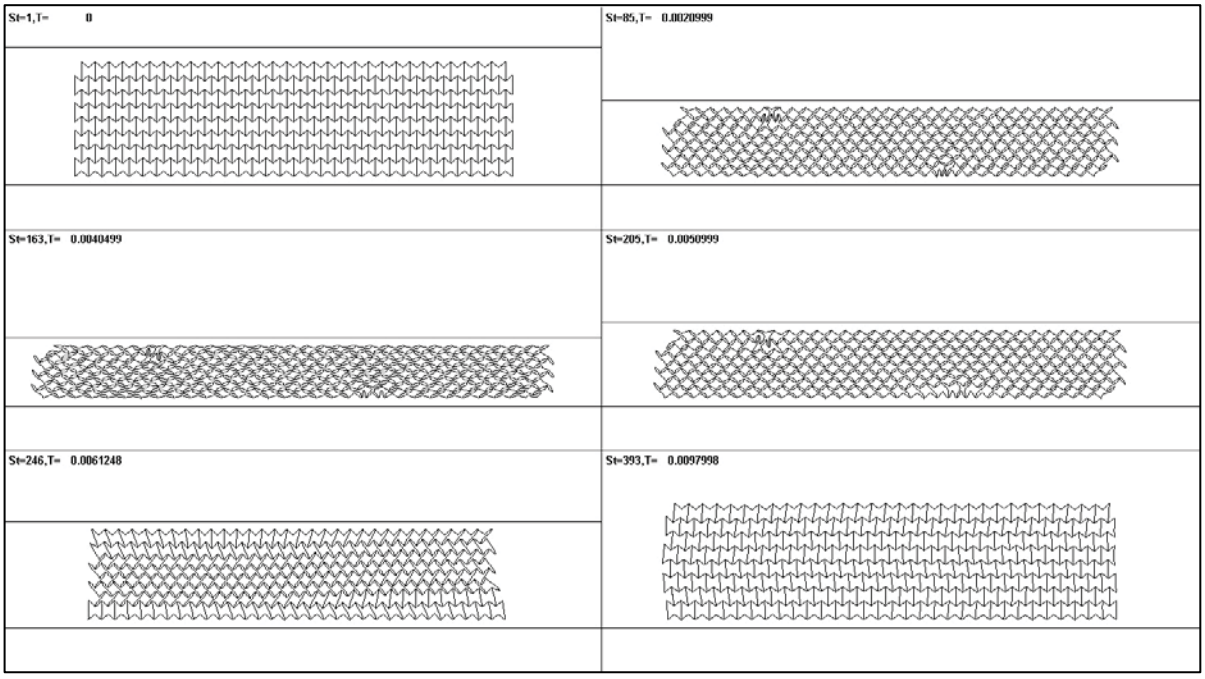

Figure 81: Original and deformed configurations of a re-entrant honeycomb specimen (VF=0.7, θ=40^o) under horizontal impact of a planar impacter with an initial speed of 2m/s.

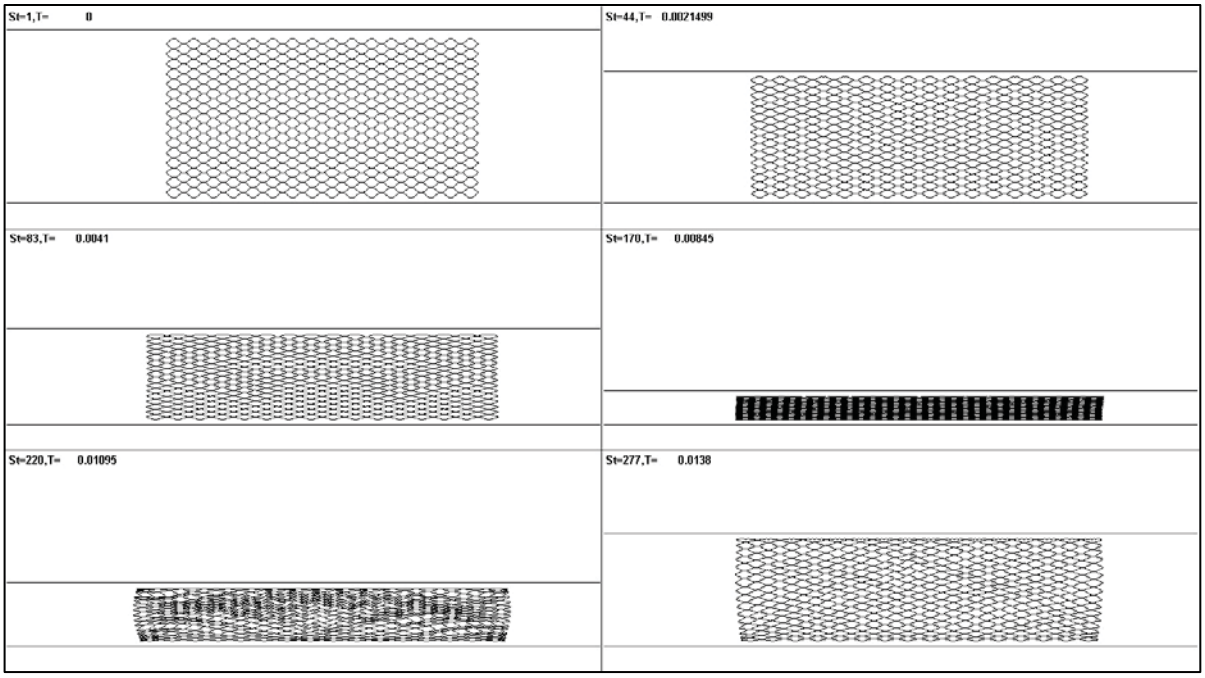

Figure 82: Original and deformed configurations of a regular honeycomb specimen (VF=0.85, θ=50^o) under horizontal impact of a planar impacter with an initial speed of 2m/s.

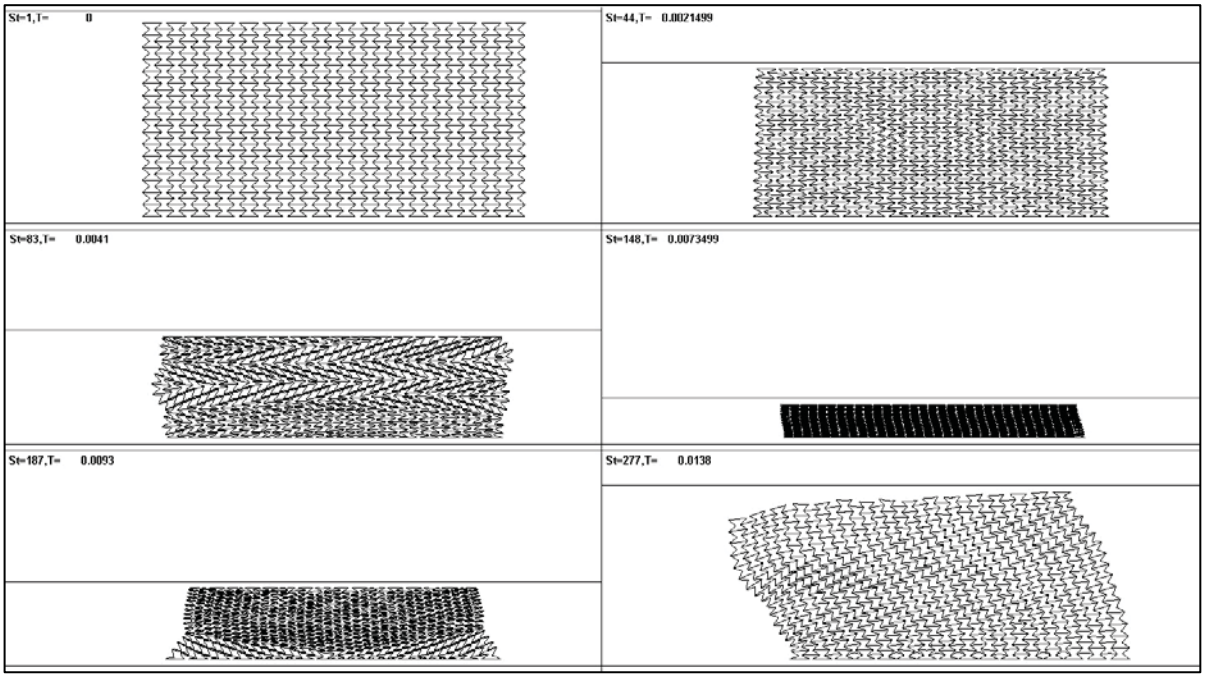

Figure 83: Original and deformed configurations of a re-entrant honeycomb specimen (VF=0.85, θ=50^o) under horizontal impact of a planar impacter with an initial speed of 2m/s.

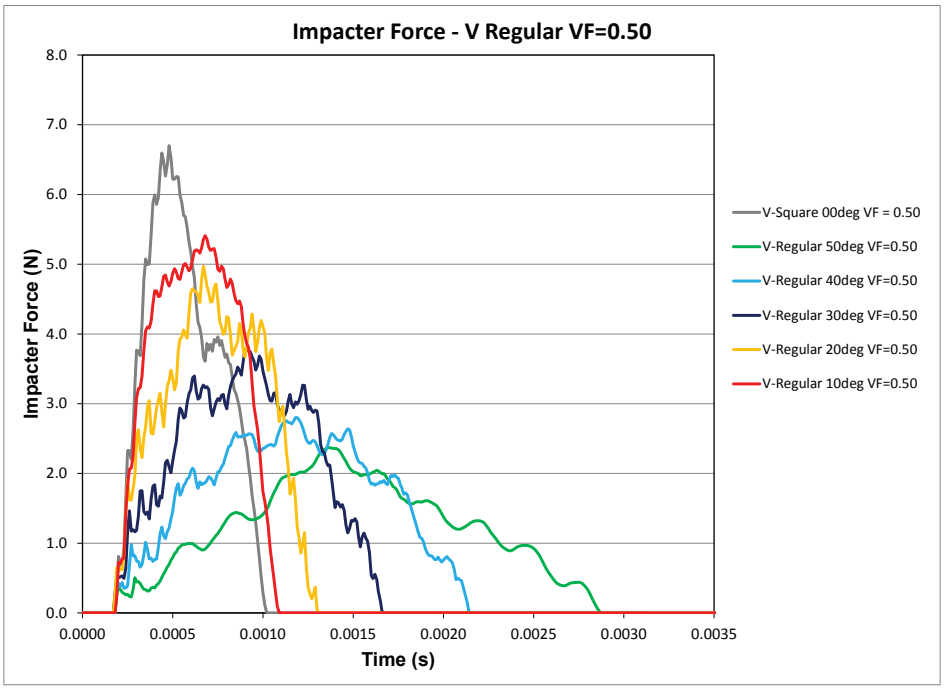

Figure 84: Impact force time histories obtained for vertical impact of a planar impacter at 2 m/s on regular honeycomb specimens with void fraction of 0.5 and different angles.

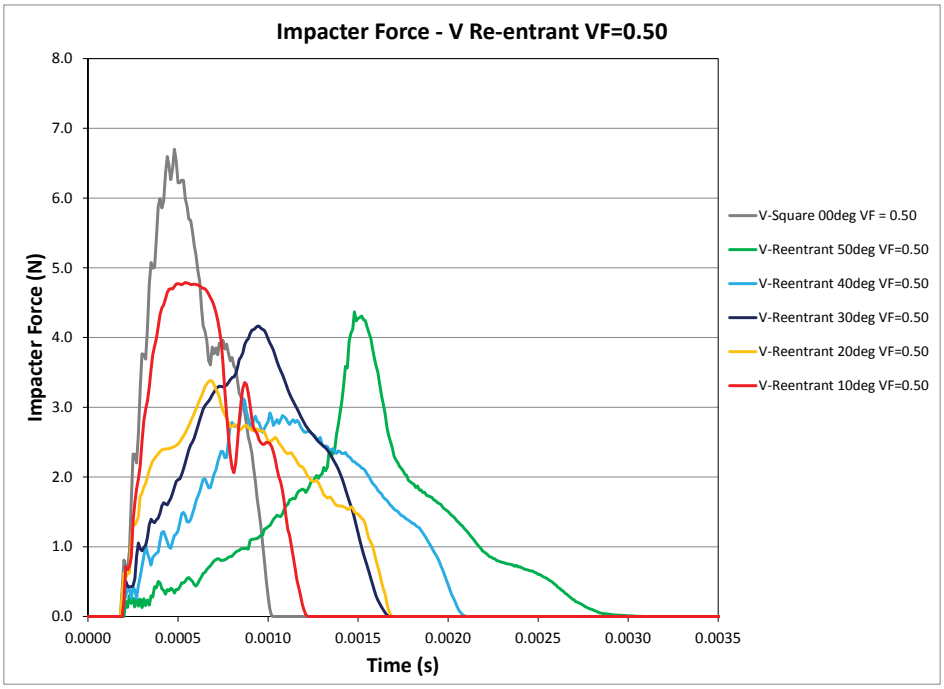

Figure 85: Impact force time histories obtained for vertical impact of a planar impacter at 2 m/s on re-entrant honeycomb specimens with void fraction of 0.5 and different angles.

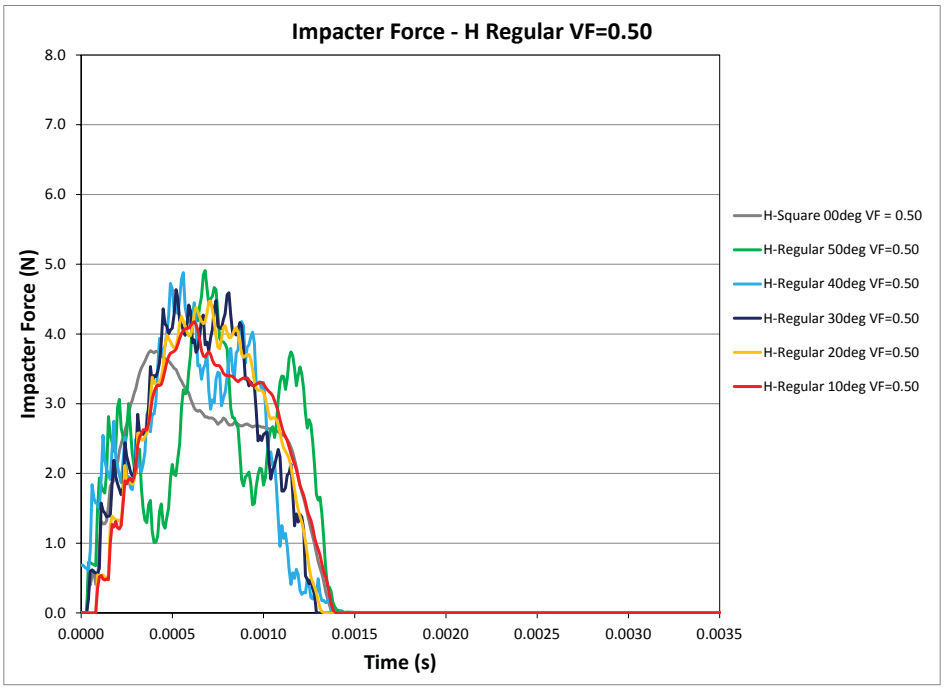

Figure 86: Impact force time histories obtained for horizontal impact of a planar impacter at 2 m/s on regular honeycomb specimens with void fraction of 0.5 and different angles.

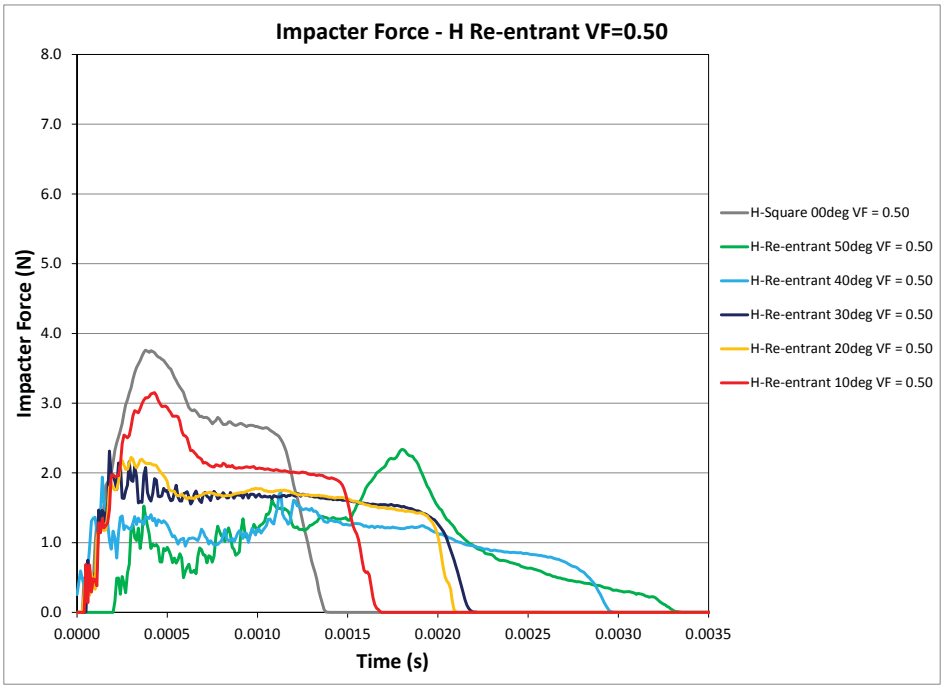

Figure 87: Impact force time histories obtained for horizontal impact of a planar impacter at 2 m/s on re-entrant honeycomb specimens with void fraction of 0.5 and different angles.

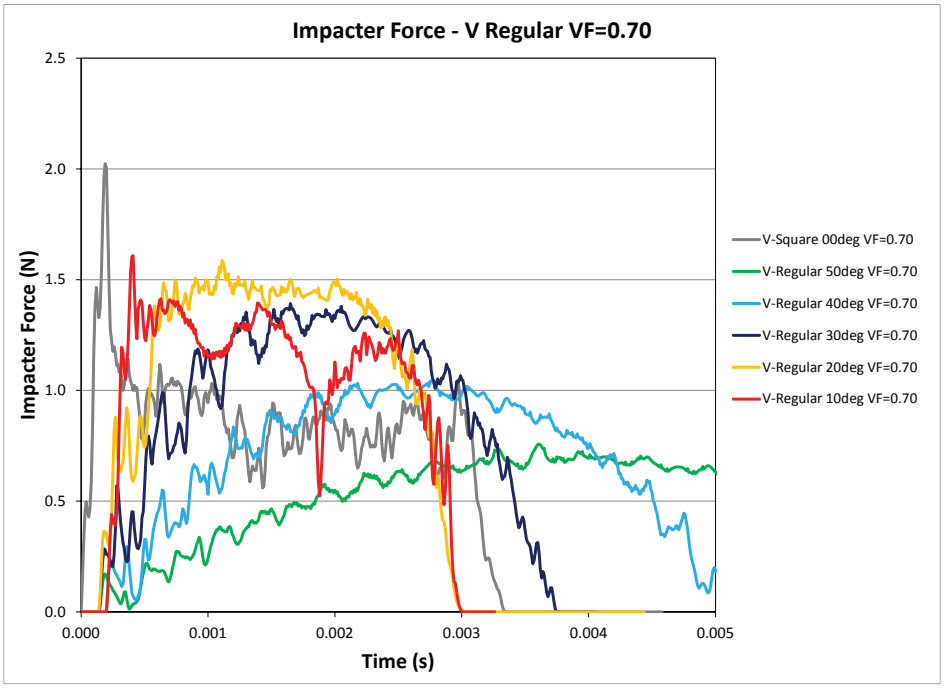

Figure 88: Impact force time histories obtained for vertical impact of a planar impacter at 2 m/s on regular honeycomb specimens with void fraction of 0.7 and different angles.

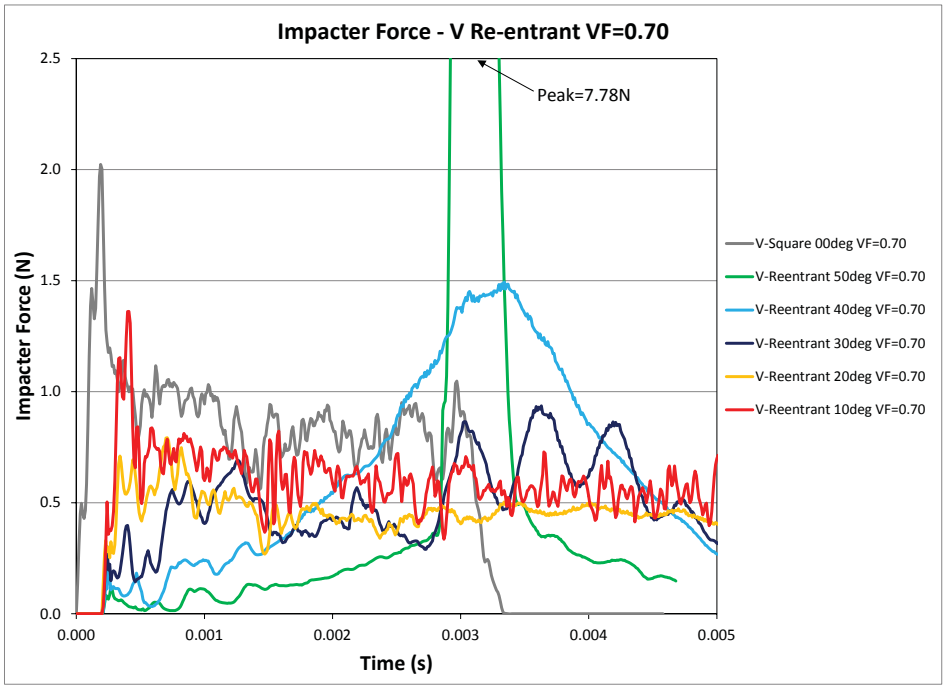

Figure 89: Impact force time histories obtained for vertical impact of a planar impacter at 2 m/s on re-entrant honeycomb specimens with void fraction of 0.7 and different angles.

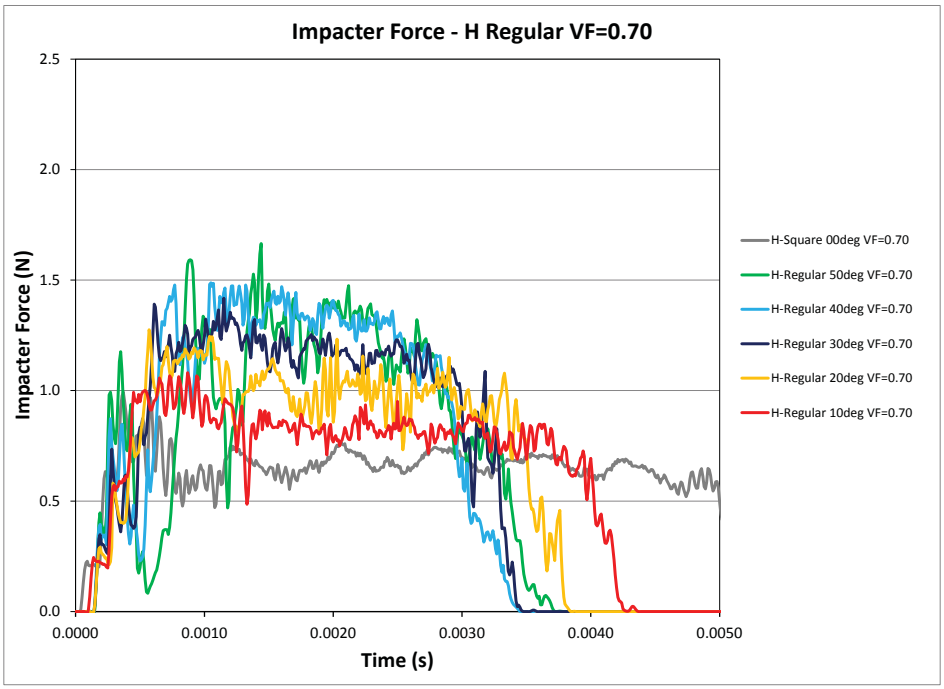

Figure 90: Impact force time histories obtained for horizontal impact of a planar impacter at 2 m/s on regular honeycomb specimens with void fraction of 0.7 and different angles.

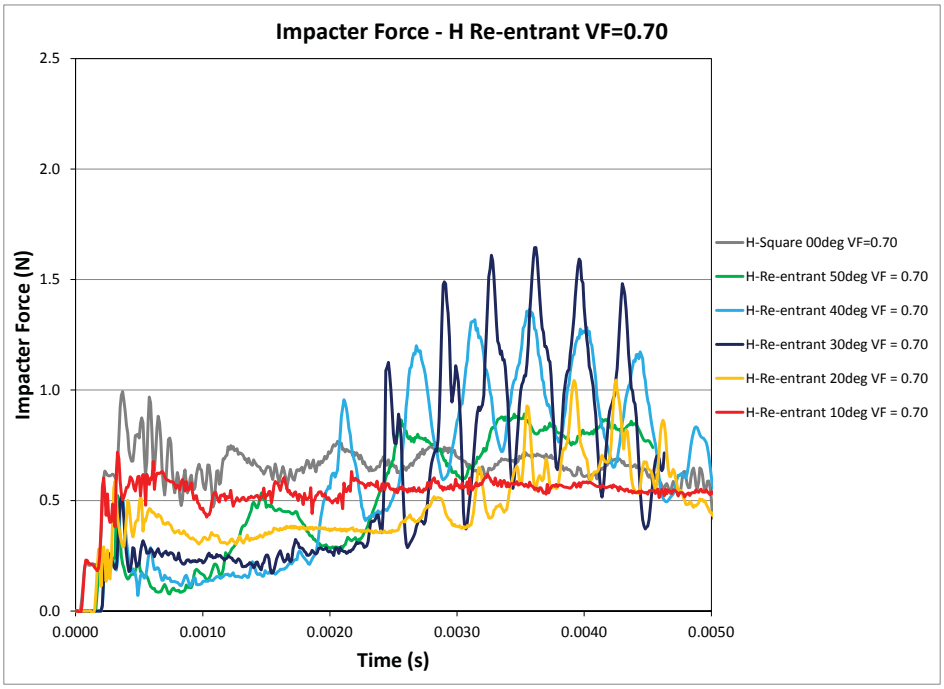

Figure 91: Impact force time histories obtained for horizontal impact of a planar impacter at 2 m/s on re-entrant honeycomb specimens with void fraction of 0.7 and different angles.

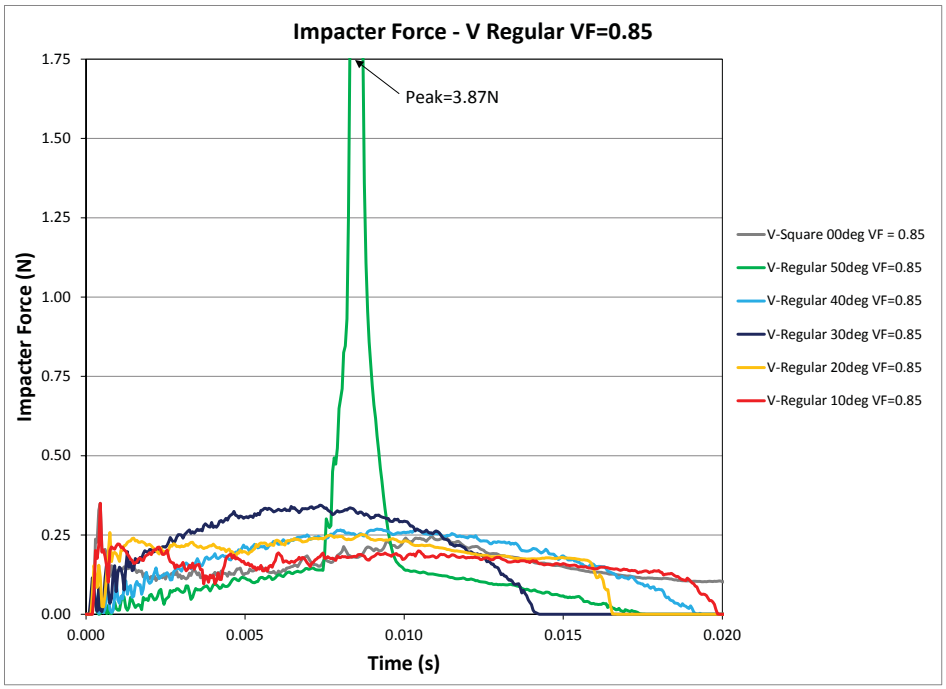

Figure 92: Impact force time histories obtained for vertical impact of a planar impacter at 2 m/s on regular honeycomb specimens with void fraction of 0.85 and different angles.

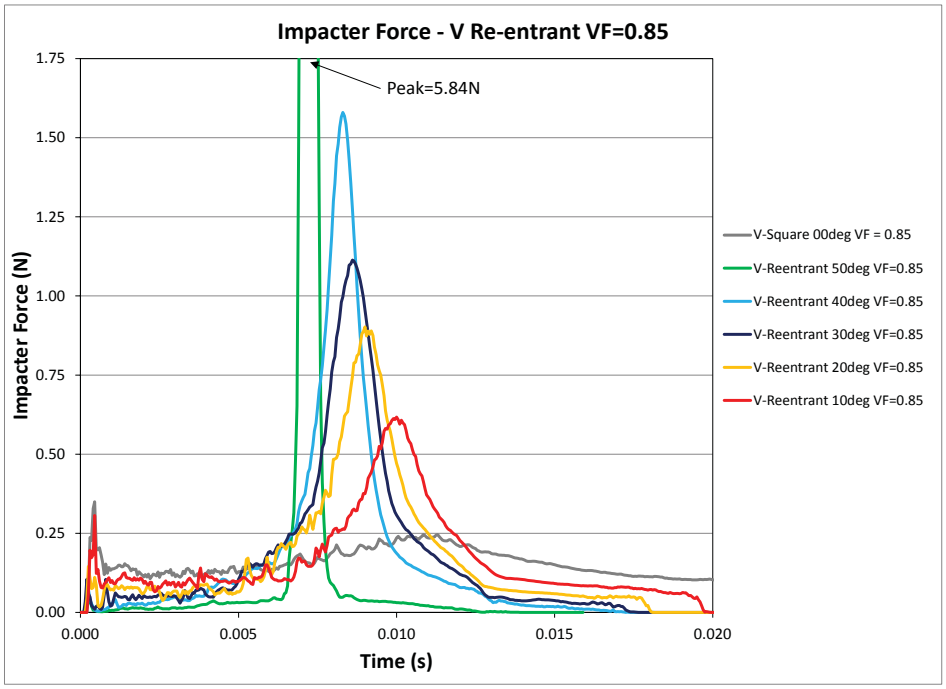

Figure 93: Impact force time histories obtained for vertical impact of a planar impacter at 2 m/s on re-entrant honeycomb specimens with void fraction of 0.85 and different angles.

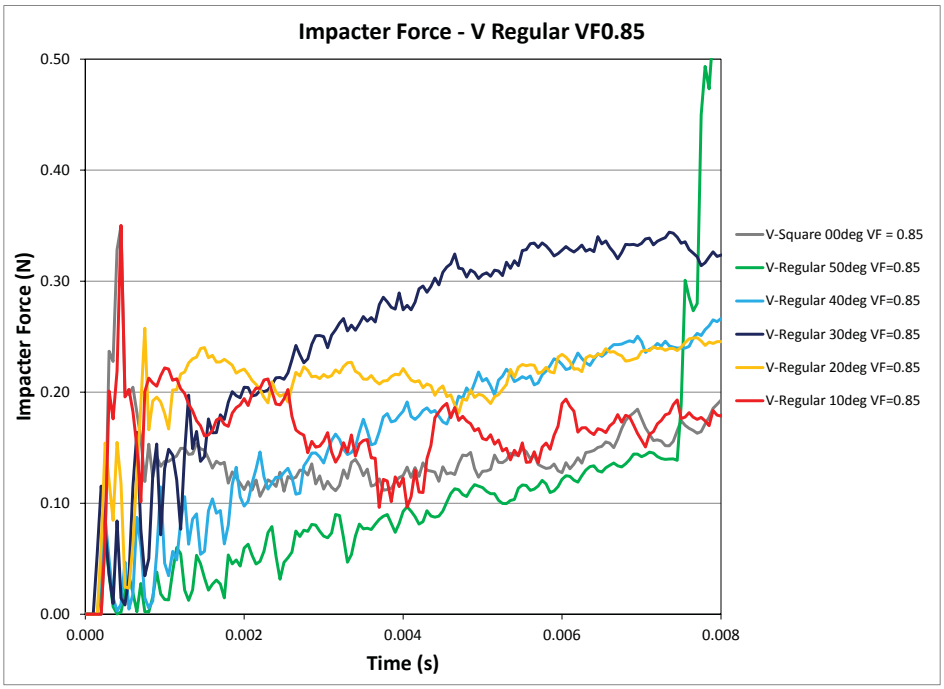

Figure 94: Details of impact forces obtained for vertical impact of a planar impacter at 2 m/s on regular honeycomb specimens with void fraction of 0.7 and different angles.

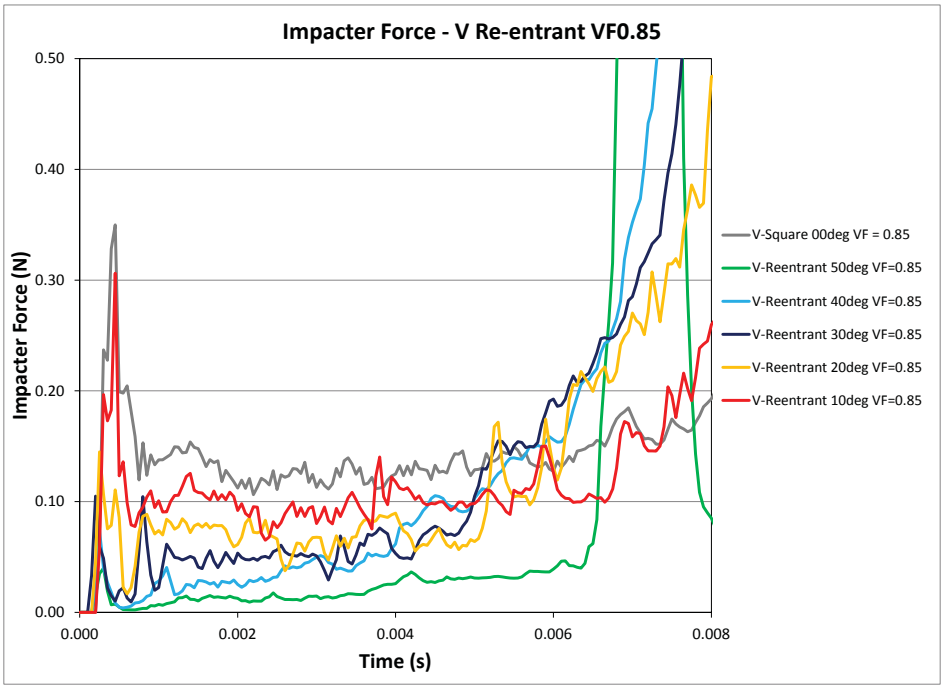

Figure 95: Details of impact forces obtained for vertical impact of a planar impacter at 2 m/s on re-entrant honeycomb specimens with void fraction of 0.7 and different angles.

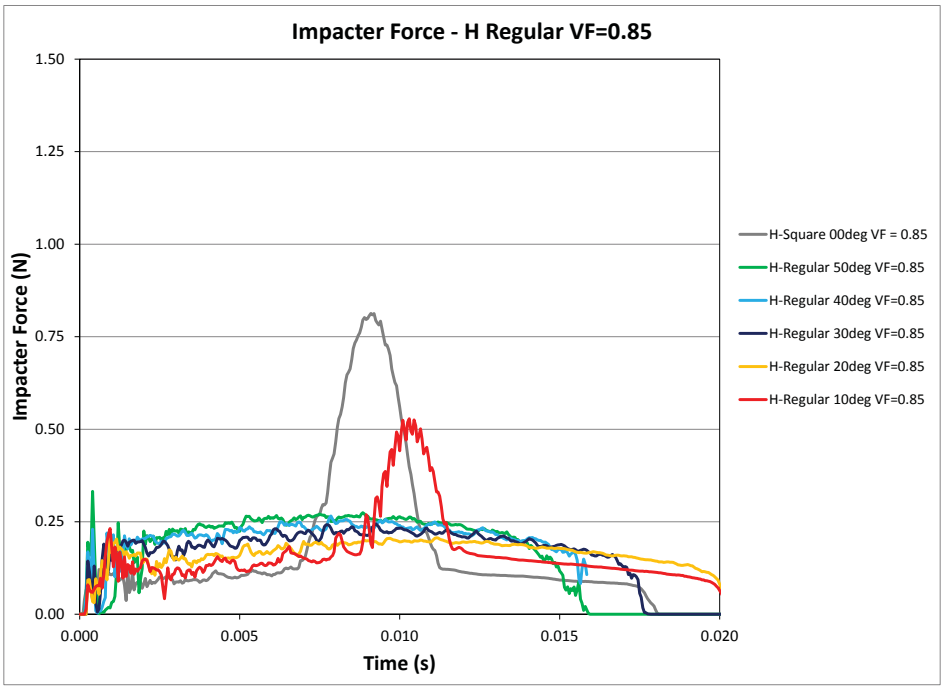

Figure 96: Impact force time histories obtained for horizontal impact of a planar impacter at 2m/s on regular honeycomb specimens with void fraction of 0.85 and different angles.

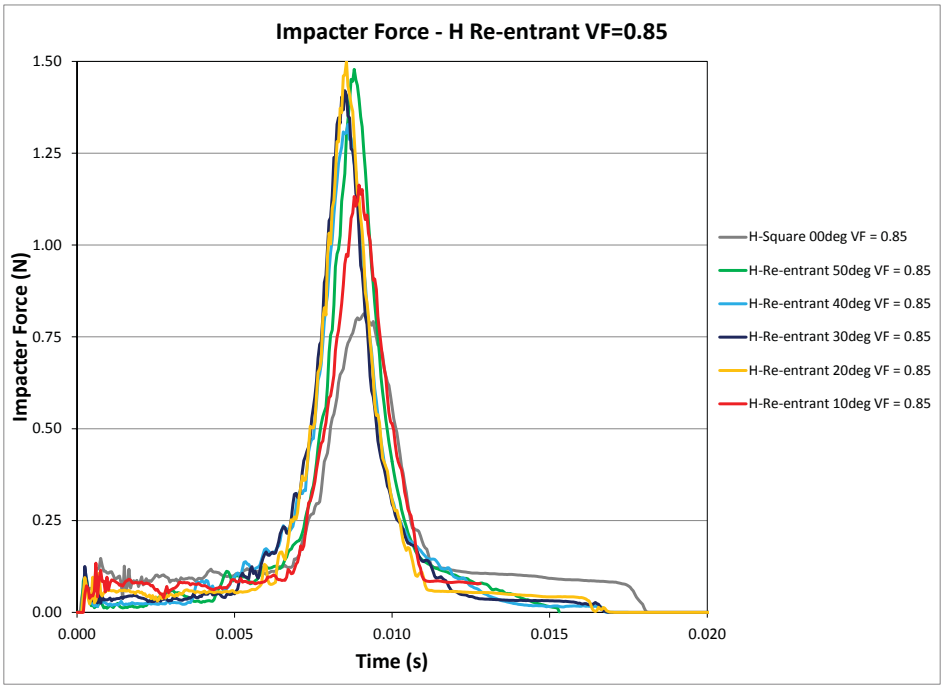

Figure 97: Impact force time histories obtained for horizontal impact of a planar impacter at 2m/s on re-entrant honeycomb specimens with void fraction of 0.85 and different angles.

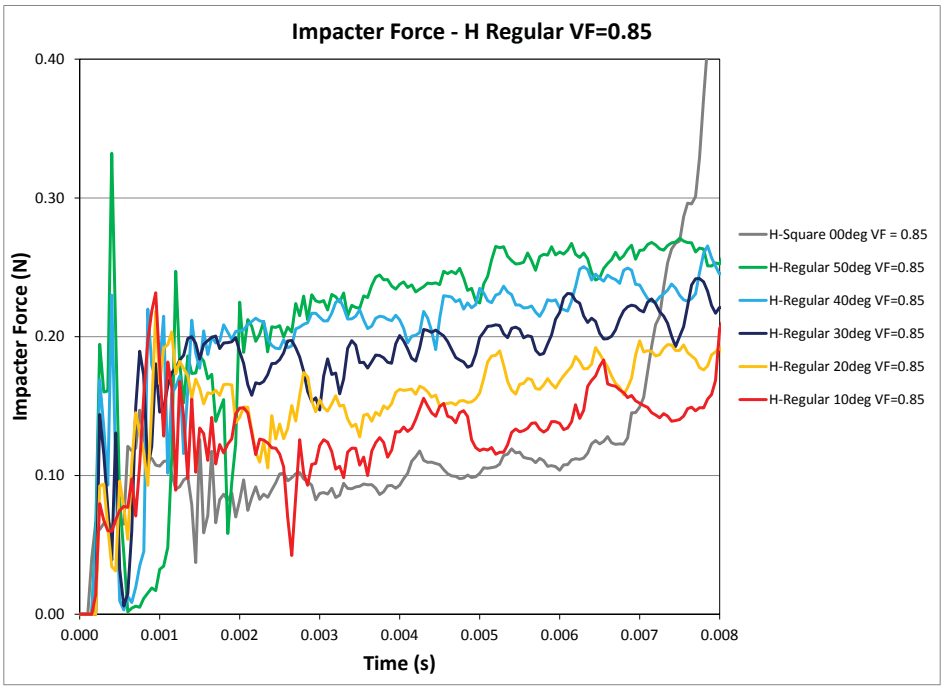

Figure 98: Details of impact forces obtained for horizontal impact of a planar impacter at 2 m/s on regular honeycomb specimens with void fraction of 0.85 and different angles.

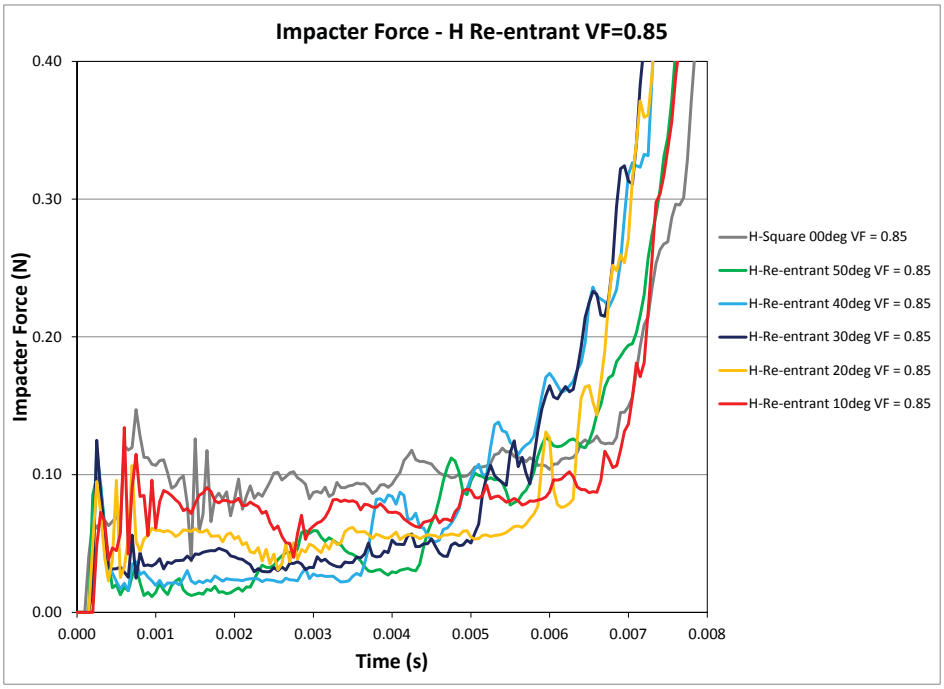

Figure 99: Details of impact forces obtained for horizontal impact of a planar impacter at 2 m/s on re-entrant honeycomb specimens with void fraction of 0.85 and different angles.

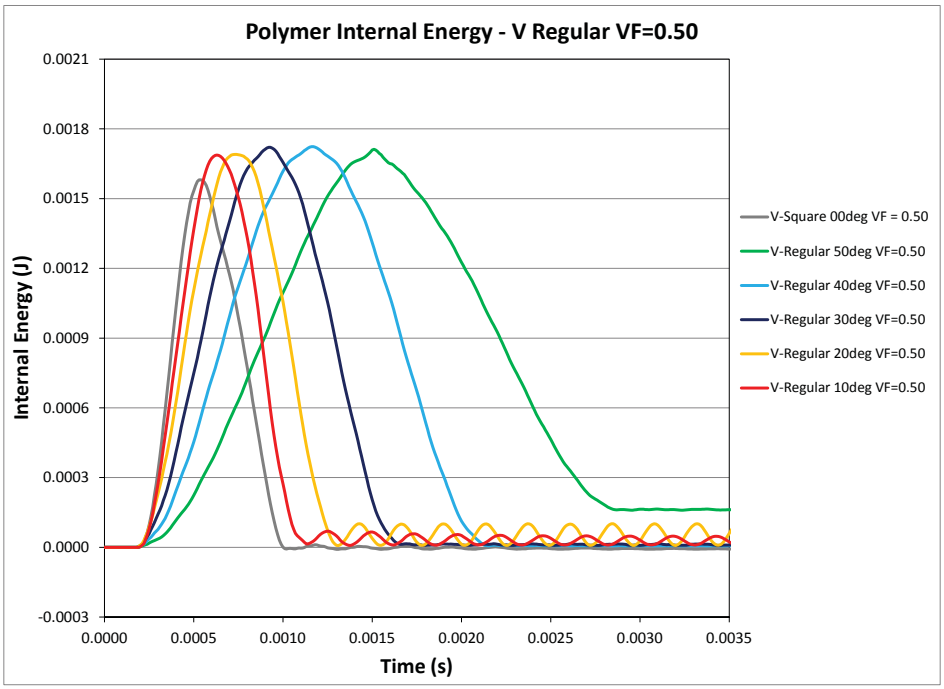

Figure 100: Internal energy time histories obtained for vertical impact of a planar impacter at 2m/s on regular honeycomb specimens with void fraction of 0.5 and different angles.

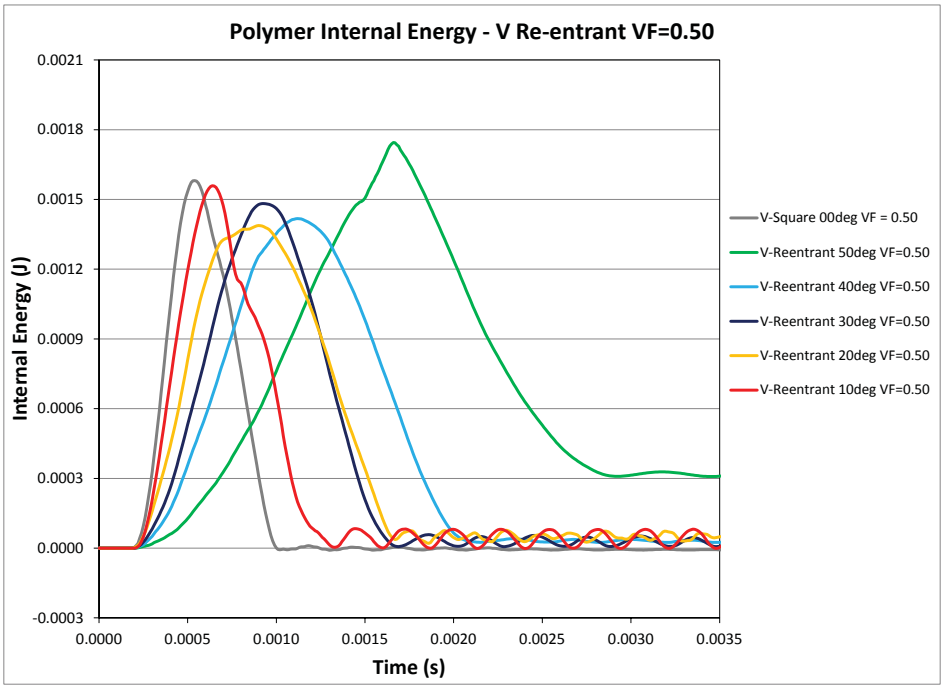

Figure 101: Internal energy time histories obtained for vertical impact of a planar impacter at 2m/s on re-entrant honeycomb specimens with void fraction of 0.5 and different angles.

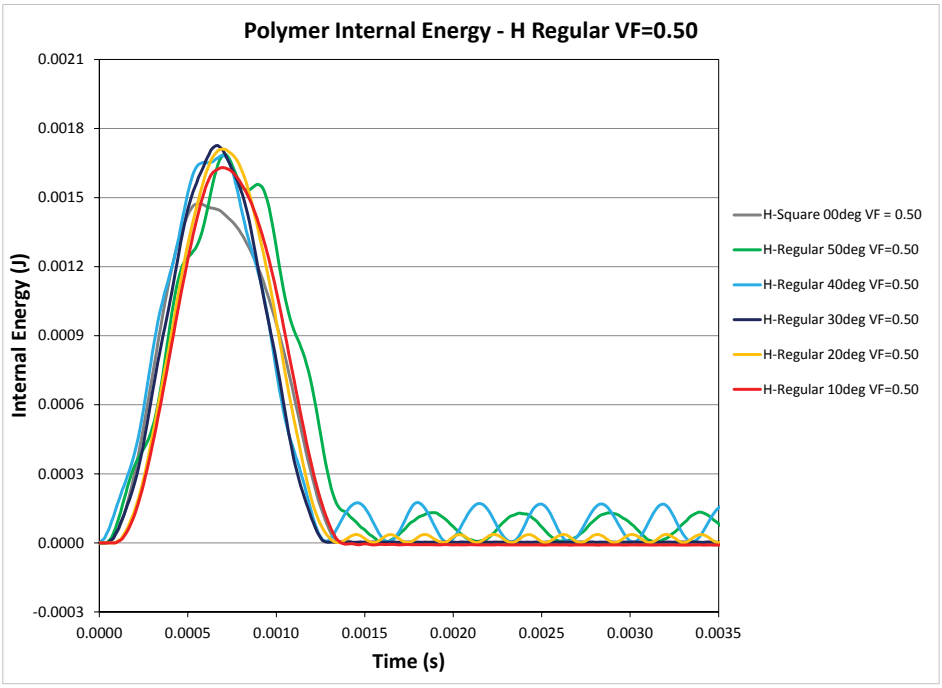

Figure 102: Internal energy time histories obtained for horizontal impact of a planar impacter at 2m/s on regular honeycomb specimens with void fraction of 0.5 and different angles.

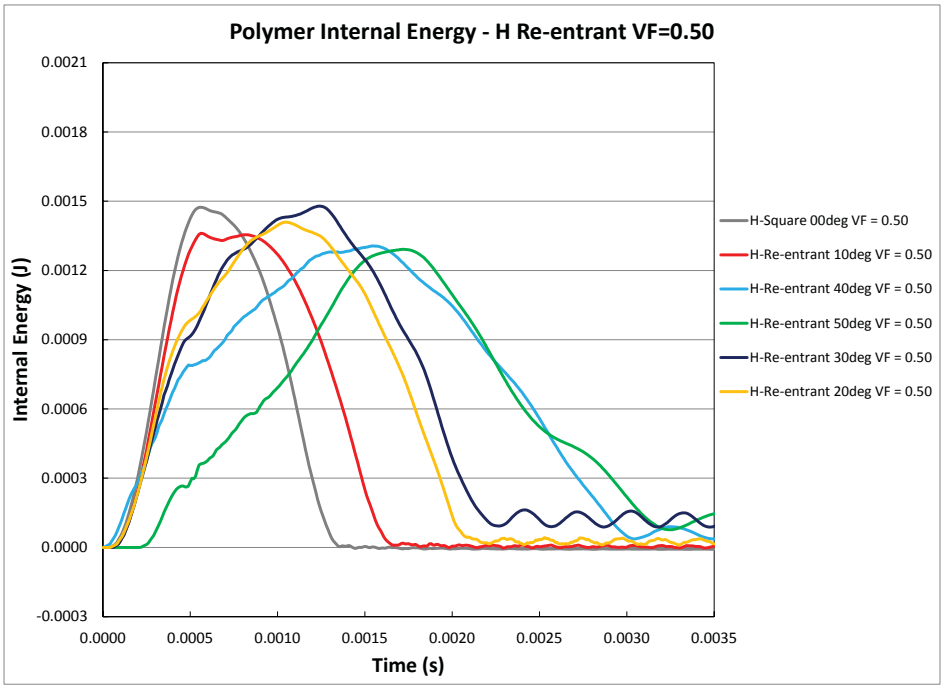

Figure 103: Internal energy time histories obtained for horizontal impact of a planar impacter at 2m/s on re-entrant honeycomb specimens with void fraction of 0.5 and different angles.

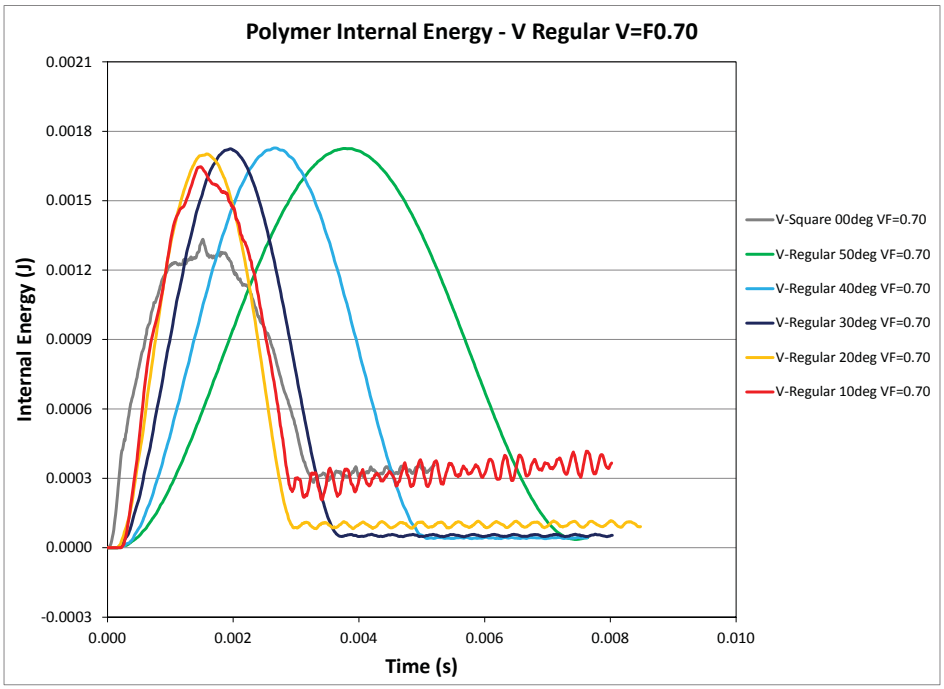

Figure 104: Internal energy time histories obtained for vertical impact of a planar impacter at 2m/s on regular honeycomb specimens with void fraction of 0.7 and different angles.

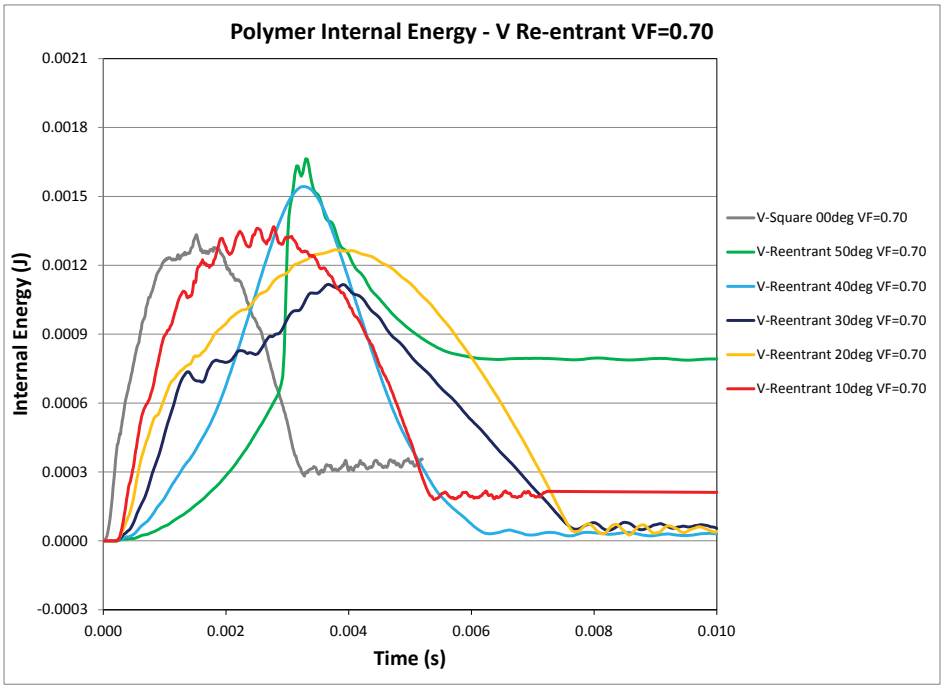

Figure 105: Internal energy time histories obtained for vertical impact of a planar impacter at 2m/s on re-entrant honeycomb specimens with void fraction of 0.7 and different angles.

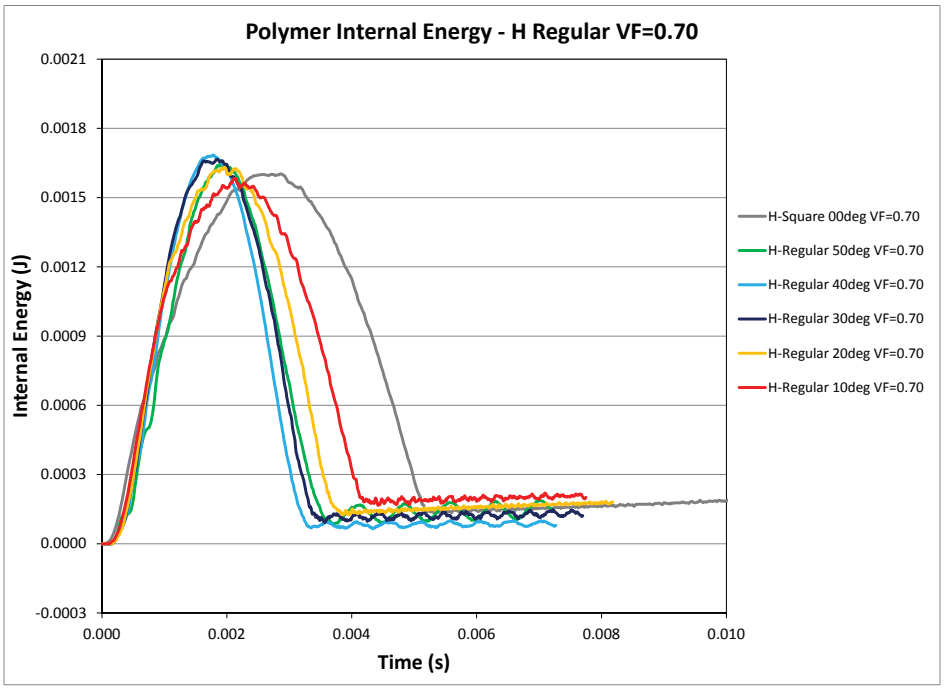

Figure 106: Internal energy time histories obtained for horizontal impact of a planar impacter at 2m/s on regular honeycomb specimens with void fraction of 0.7 and different angles.

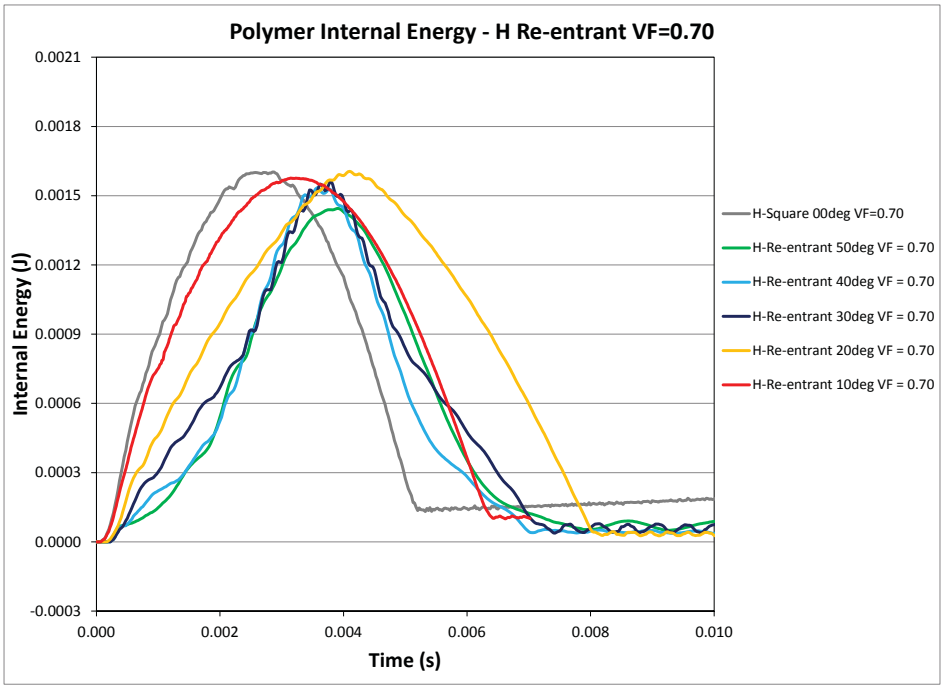

Figure 107: Internal energy time histories obtained for horizontal impact of a planar impacter at 2m/s on re-entrant honeycomb specimens with void fraction of 0.7 and different angles.

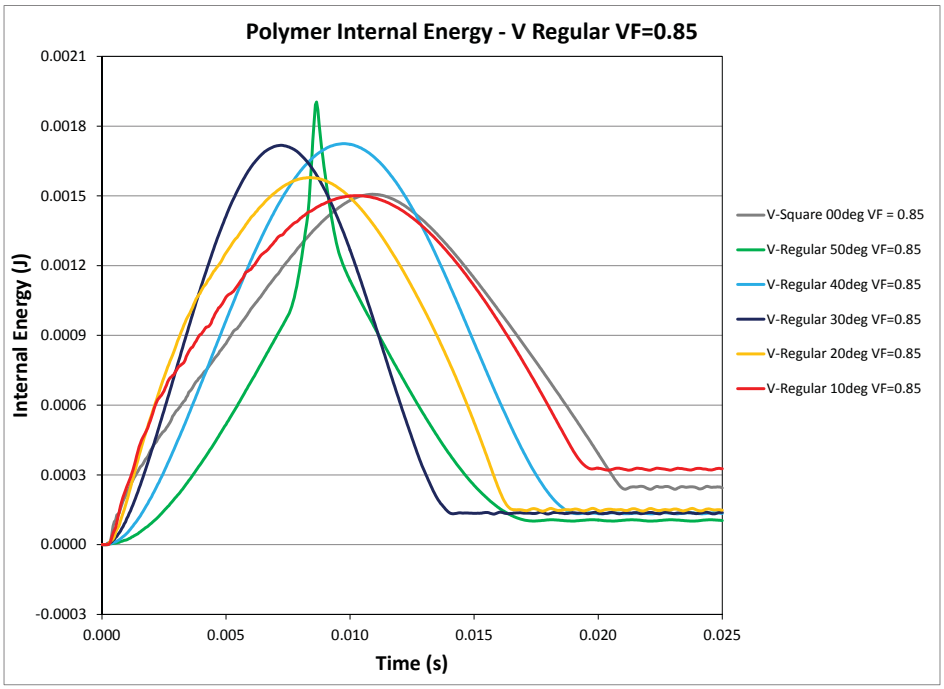

Figure 108: Internal energy time histories obtained for vertical impact of a planar impacter at 2m/s on regular honeycomb specimens with void fraction of 0.85 and different angles.

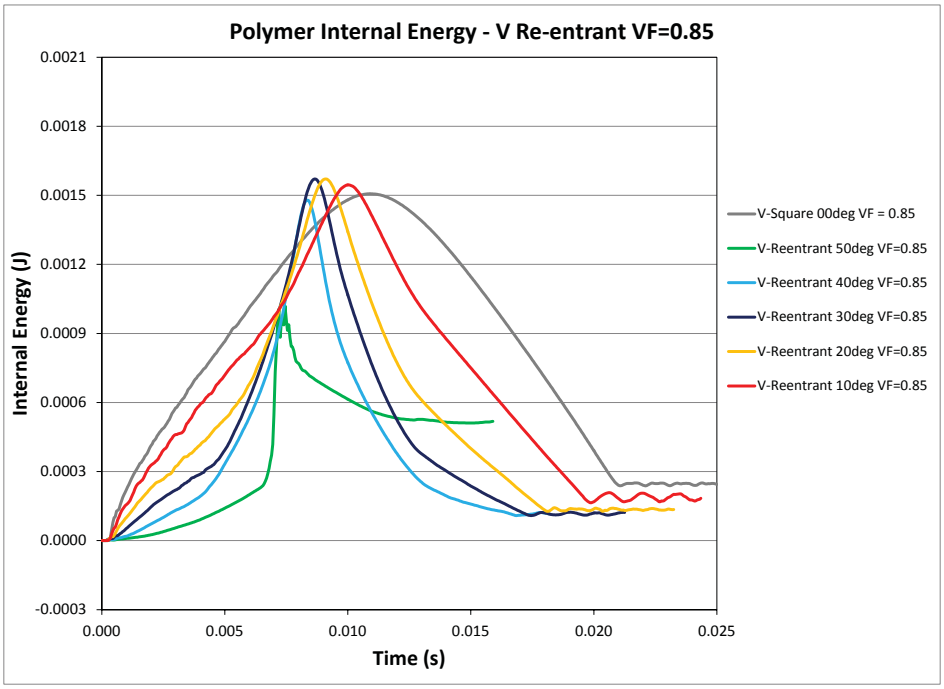

Figure 109: Internal energy time histories obtained for vertical impact of a planar impacter at 2m/s on re-entrant honeycomb specimens with void fraction of 0.85 and different angles.

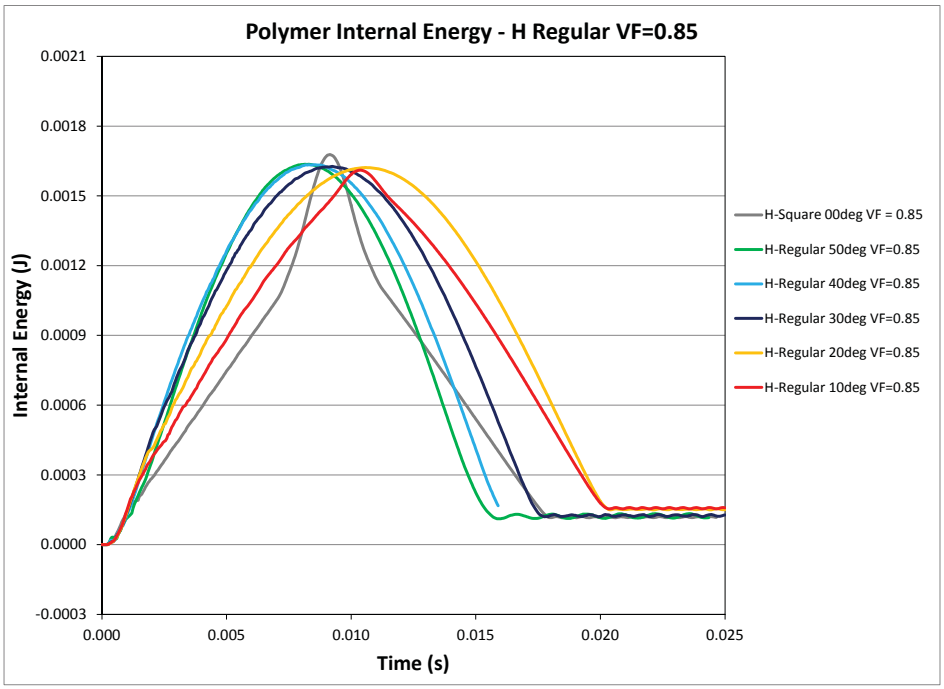

Figure 110: Internal energy time histories obtained for horizontal impact of a planar impacter at 2m/s on regular honeycomb specimens with void fraction of 0.85 and different angles.

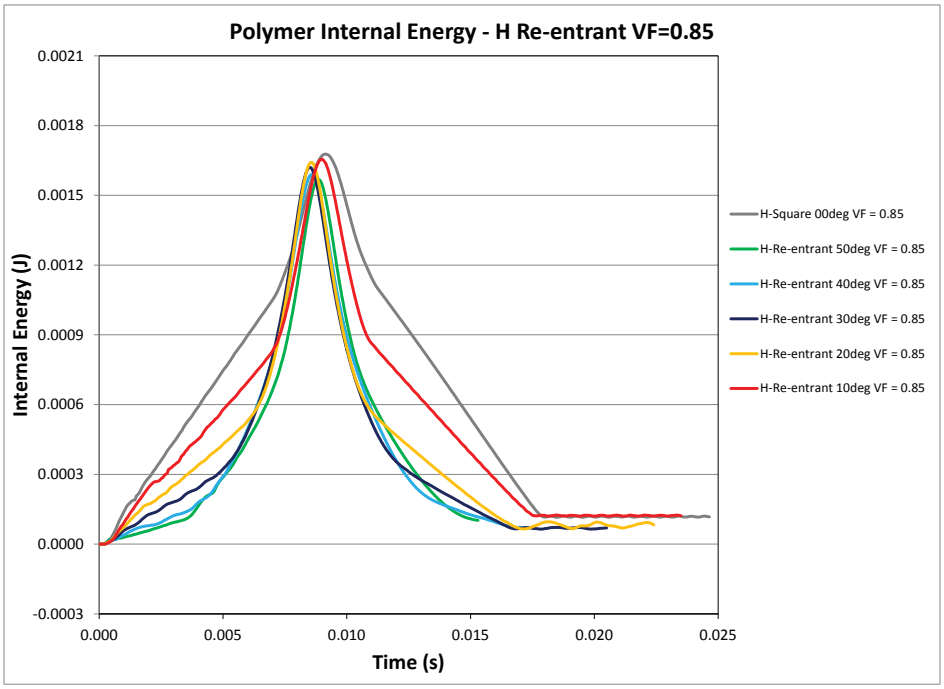

Figure 111: Internal energy time histories obtained for horizontal impact of a planar impacter at 2m/s on re-entrant honeycomb specimens with void fraction of 0.85 and different angles.

5 Parametric Study for Partial Compression of Auxetic Materials Subject to Impact of a Cylindrical Impacter

The previous parametric studies involved full and partial compression of the auxetic materials under impact of a planar impacter simulated using a rigid plate. This impact condition resulted in a nearly uniform distribution of impact force over the whole width of the material samples. However, in reality, the impacter is normally of finite size where the impact force applied on the auxetic foam material is localized.

In order to investigate the material performance under localized impact, a test model involving a cylindrical impacter was developed and a parametric study was then designed and performed. The same matrix of the conventional and re-entrant honeycomb configurations utilized in the previous parametric studies was again adopted and the study was focused on partial compression of the material samples.

The set-up of the test model for local impact is given in Figure 112 below. This model contains a cylindrical impacter with an outer diameter of 5 mm. The mass of the impacter was 10 times of that of the material samples. This cylindrical impacter was represented by rigid shell elements with a thickness of 1 mm. The initial impacter speed was set of 2 m/s. The contact between the impacter and the sample was assumed to be frictionless. As before, the sample was supported by a rigid plate. In order to prevent the deformed sample to lift from the supporting plate, the vertical displacements on the bottom of the sample were constrained. However, these bottom nodes were allowed to slide freely in the horizontal (X) direction.

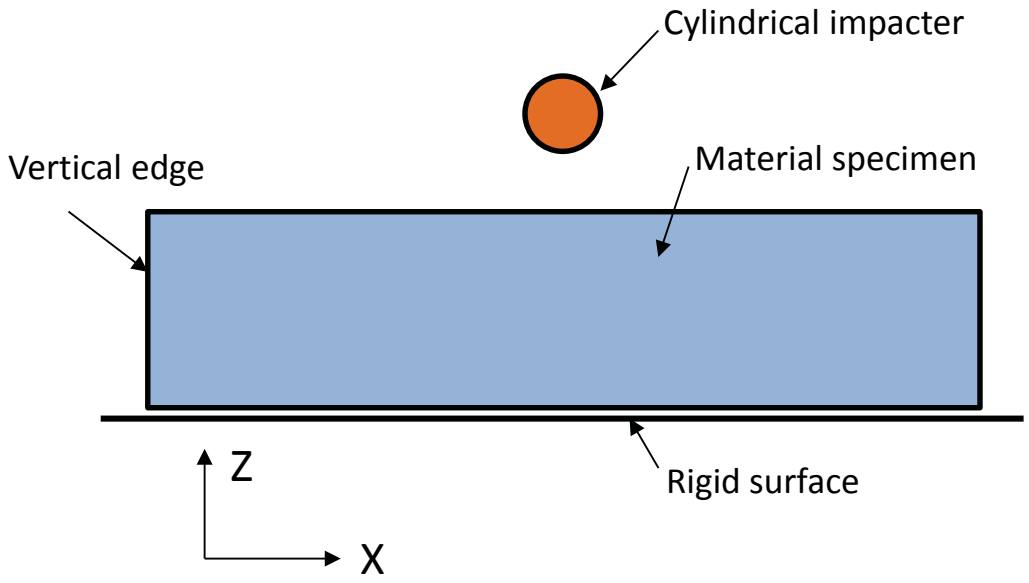

Figure 112: Problem setup for parametric study with a cylindrical Impacter.

In order to ensure that the numerical solutions are insensitive to the model width, a numerical study was first conducted to determine the suitable width of the material samples in the finite element model. This study concluded that for this local impact problem, the model width used in the previous parametric studies for planar impacter needed to be doubled to contain 32 columns of the unit cells.

The next factor to be considered was the influence of the X-constraints along the vertical edges on the mechanical behaviour of the material samples. The purpose of the boundary conditions was to account for the interactions of the sample material in the finite element models with the surrounding materials which were truncated from the models. Numerical results shown in Figures 113 and 114 indicated that the predicted peak impact forces for conventional material samples were not influenced by the boundary conditions on the vertical edges. However, for the re-entrant material samples, these boundary conditions had significant effects on the predicted peak impact force, especially for the vertical impact condition.

In order to gain a better understanding on the cause of the differences in peak impacter forces, we compared the impacter force time histories (Figure 115) and the deformed configurations (Figures 116 to 119) generated from these numerical simulations. This examination indicated that in the solution for free boundary conditions, the materials from surrounding area flowed freely into the impact region. This flow of material increased the material density right below the impacter, resulting in a significant increase in the impact force. In addition, due to the free contraction of the material in the horizontal direction, the sample experienced more straining in the vertical direction upon the impact, pushing the material into the high stiffness phase indicated in Figure 77. On the other hand, when the horizontal displacements were constrained on the vertical edges, the flow of material towards the impact region was restricted, but the resistance to impacter was enhanced by the tension developed in the horizontal direction. This resulted in a more smooth impact force time history as shown in Figure 115. It should be noted that both the free and fully constrained boundary conditions considered above represented the extreme conditions and the real situation was in the middle. However, in order to make the boundary conditions in this parametric study consistent with the previous ones, the free boundary condition has been adopted.

The current parametric study for local impact was designed to use the test case matrix defined in Table 1 which contained a total of 66 unique combinations of sample types (conventional or re-entrant; angle θ), void fraction and impact orientation (vertical; horizontal). The numerical results were processed using the same procedure as before and the resulting time histories of the impact force and polymer internal energy are presented in Figures 120 to 143. The predicted deformed configurations for all cases were also checked to ensure the stability of the numerical solutions.

These results indicated that for re-entrant materials under both vertical and horizontal impacts, the initial resistance to the impacter was inversely proportional to the geometric angle θ. This trend is in line with the effective elastic moduli presented in Table 3 in reference [1] and is also consistent with the observations from the previous parametric studies based on planar impacter. However, if the initial stiffness of the material samples was too low, such as for re-entrant specimens with void fraction of 0.7 and 0.85 and angle $\theta=50^{O}$, the low resistance provided by the material would be insufficient to decelerate the impacter effectively at the early part of the transient, so that the material around the impacter entered the high stiffness phase of the stress-strain curve. In these cases, large peak impact forces were generated.

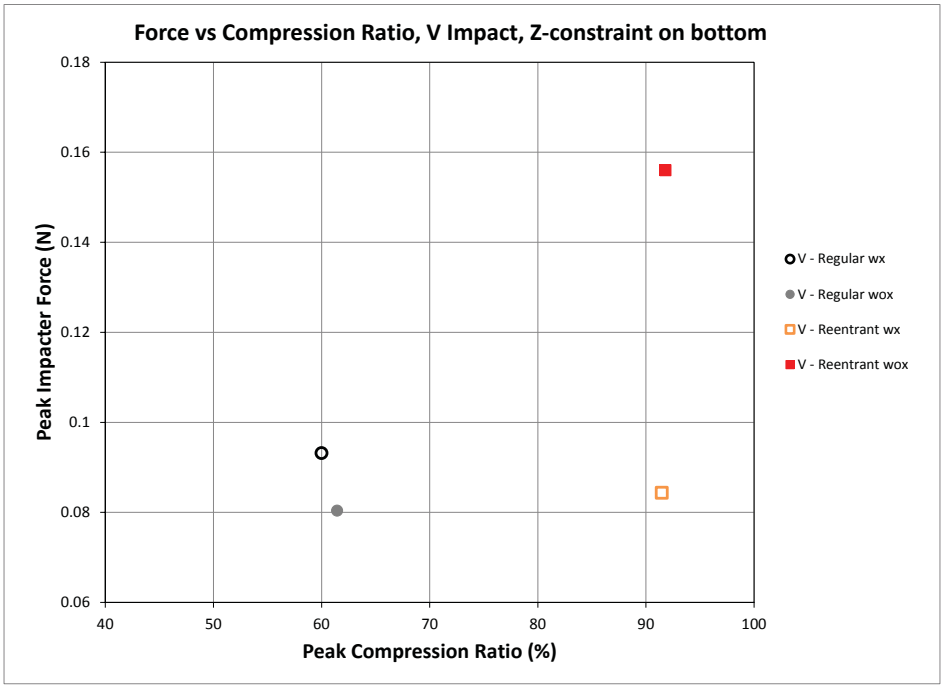

Figure 113: Peak impacter force vs peak compression ratio for vertical impact of a cylindrical impacter of 2m/s on regular and re-entrant honeycomb samples (VF=0.85, θ=40°) with and without X-constraints on the vertical edges.

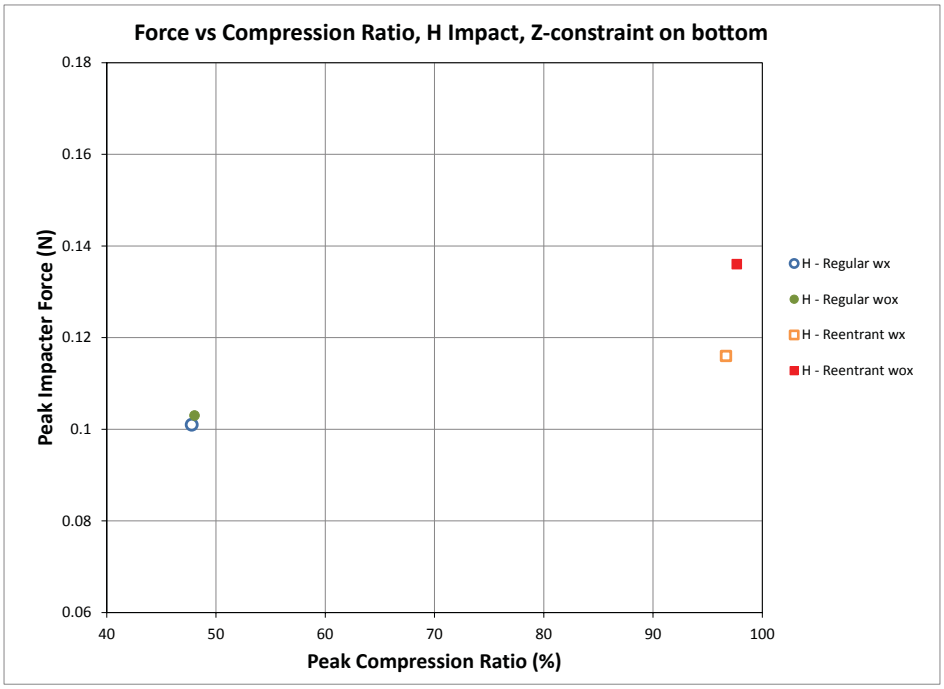

Figure 114: Peak impacter force vs peak compression ratio for horizontal impact of a cylindrical impacter on regular and re-entrant honeycomb samples (VF=0.85, θ=40°) with and without X-constraints on the vertical edges.

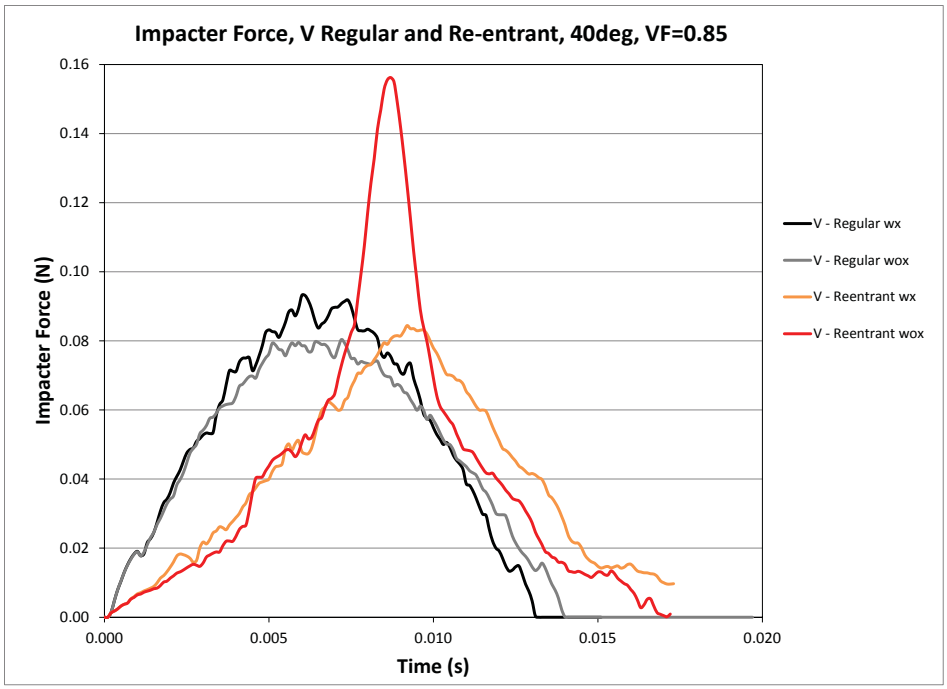

Figure 115: Impact force time histories for vertical impact of a cylindrical impacter of 2m/s on various honeycomb samples with and without X-constraints on the vertical edges.

The trends observed for the conventional material samples are more complicated. First of all, the material samples of lower void fraction, such as 0.5, showed the same trend observed earlier, namely the resistance to the impacter decreased with the increase of angle θ. However, for material samples with higher void fractions, the resistance was initially increased with the increase of angle θ, but then decreased with the further increase of θ when a critical θ value was exceeded. This critical θ value seemed to be a function of the void fraction and the impact orientation.

The variations of the peak impact force with material geometric angle θ for different void factions and impact orientations are summarized in Tables 6 and 7 and in Figures 132 to 137. The percentage differences between the peak forces from the regular and re-entrant material samples are also presented in Tables 6 and 7. These results clearly indicated that for polymer layers with similar aerial density, the magnitudes of the peak forces are heavily influenced by the void fraction. For instance, for small and intermediate material angle θ, the peak forces decreased monotonically with the increase of void fraction. Also for small and intermediate angle θ and for horizontal impact, the re-entrant material samples consistent generate significantly lower peak impact forces than the corresponding regular honeycomb material samples. The levels of the reduction range from 20% to 50%. However, when the material angle θ is large, the peak impact forces in the re-entrant material samples could increase sharply because the local deformations in the material becomes sufficient large to enter the high stiffness region of the stress-strain curve. In these extreme cases, use of re-entrant materials as protective layers may even cause more damage in the substrate.

Table 6: Peak impact force vs. angle θ for vertical impact of a cylindrical impacter of 2m/s on regular and re-entrant honeycomb specimens with various void fractions.

θ (deg)	VF=0.50			VF=0.70			VF=0.85		
	Regular	Re-entrant	%	Regular	Re-entrant	%	Regular	Re-entrant	%
0	0.712	0.712	0.000	0.287	0.287	0.000	0.091	0.091	0.000
10	0.649	0.620	4.468	0.325	0.232	28.615	0.104	0.081	22.500
20	0.592	0.680	-14.865	0.325	0.188	42.154	0.114	0.075	33.947
30	0.515	0.963	-86.990	0.281	0.211	24.911	0.108	0.082	24.167
40	0.480	0.745	-55.208	0.239	0.237	0.837	0.092	0.109	-18.093
50	0.409	1.220	-198.289	0.203	1.180	-481.281	0.076	0.970	-1169.63

Table 7: Peak impact force vs. angle θ for horizontal impact of a cylindrical impacter of 2m/s on regular and re-entrant honeycomb specimens with various void fractions

θ (deg)	VF=0.50			VF=0.70			VF=0.85		
	Regular	Re-entrant	%	Regular	Re-entrant	%	Regular	Re-entrant	%
0	0.700	0.700	0.000	0.238	0.238	0.000	0.075	0.075	0.000
10	0.722	0.577	20.083	0.301	0.209	30.565	0.089	0.063	28.796
20	0.737	0.432	41.384	0.334	0.169	49.401	0.096	0.070	26.951
30	0.692	0.409	40.896	0.293	0.176	39.932	0.101	0.101	0.000
40	0.592	0.343	42.061	0.295	0.190	35.593	0.101	0.132	-30.693
50	0.543	0.343	36.832	0.251	0.151	39.841	0.091	0.273	-200.000

The predicted time histories of the polymer internal energy are presented in Figures 138 to 149. The general characteristics of the predicted time histories of the polymer internal energy are also consistent with the earlier results, which again indicated that the dynamic response of the samples were nearly elastic. The peaks in the internal energy corresponded to the peak impact forces very well.

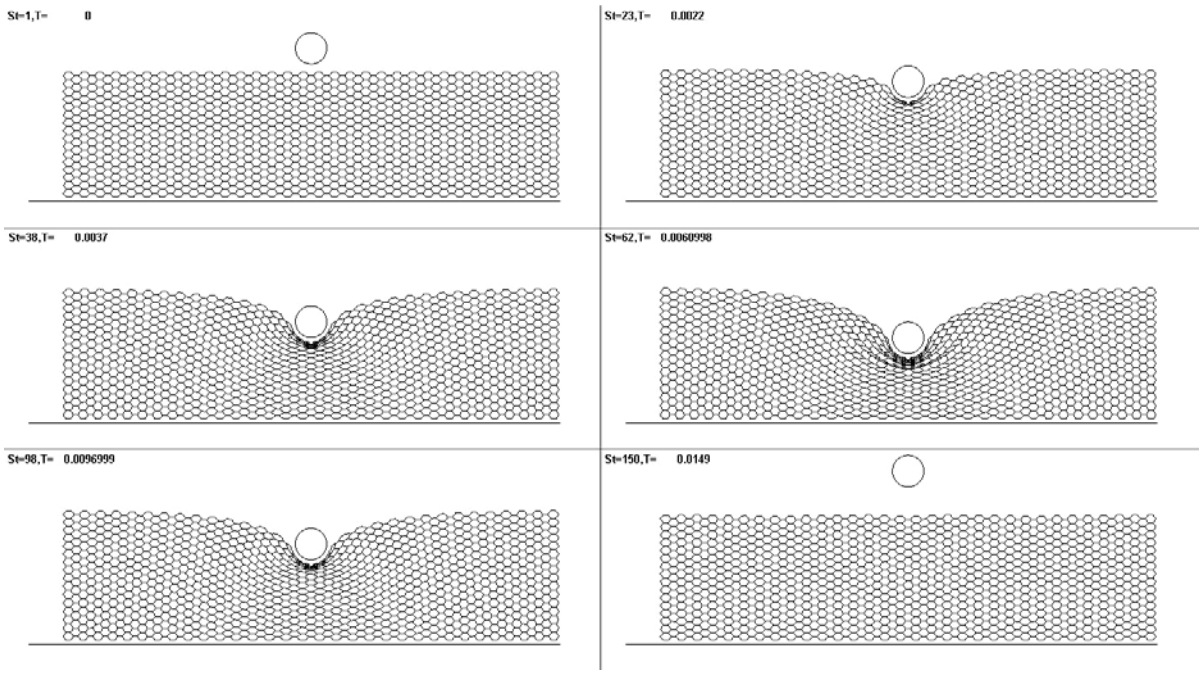

Figure 116: Original and deformed configurations of a regular honeycomb sample (VF=0.85, θ=40^o) with X-constraints subject to vertical impact of a cylindrical impacter at 2m/s.

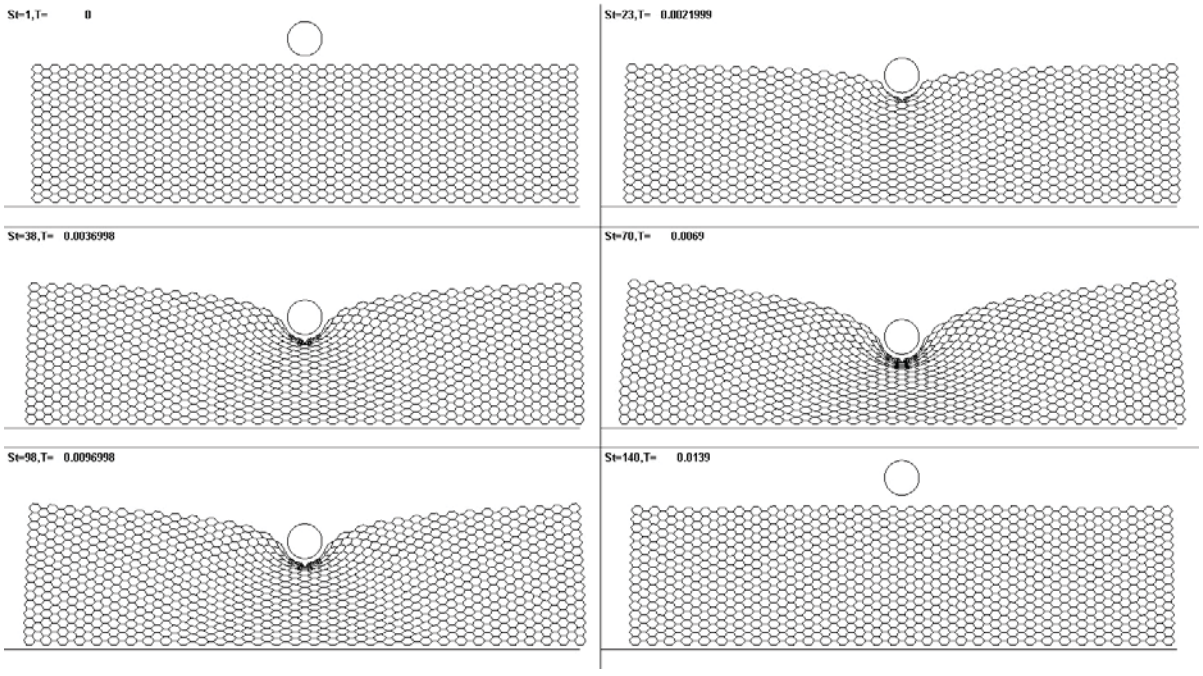

Figure 117: Original and deformed configurations of a regular honeycomb sample (VF=0.85, θ=40^o) without X-constraints subject to vertical impact of a cylindrical impacter at 2m/s.

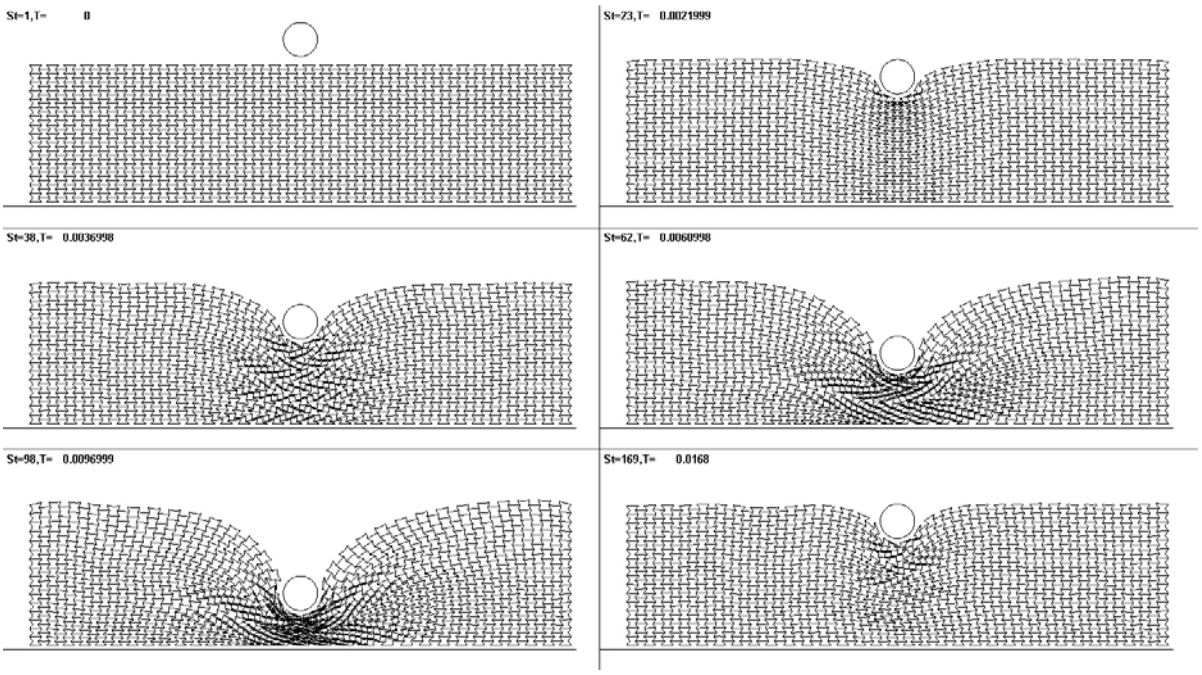

Figure 118: Original and deformed configurations of a re-entrant honeycomb sample (VF=0.85, θ=40°) with X-constraints subject to vertical impact of a cylindrical impacter at 2m/s.

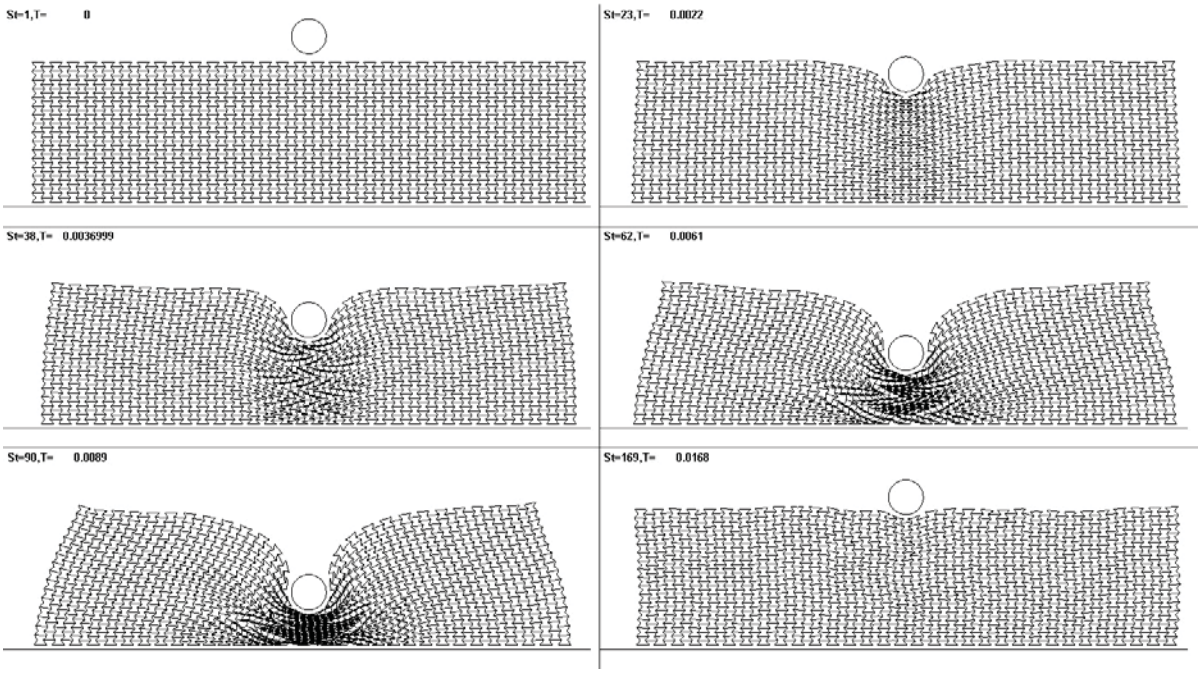

Figure 119: Original and deformed configurations of a re-entrant honeycomb sample (VF=0.85, θ=40°) without X-constraints subject to vertical impact of a cylindrical impacter at 2m/s.

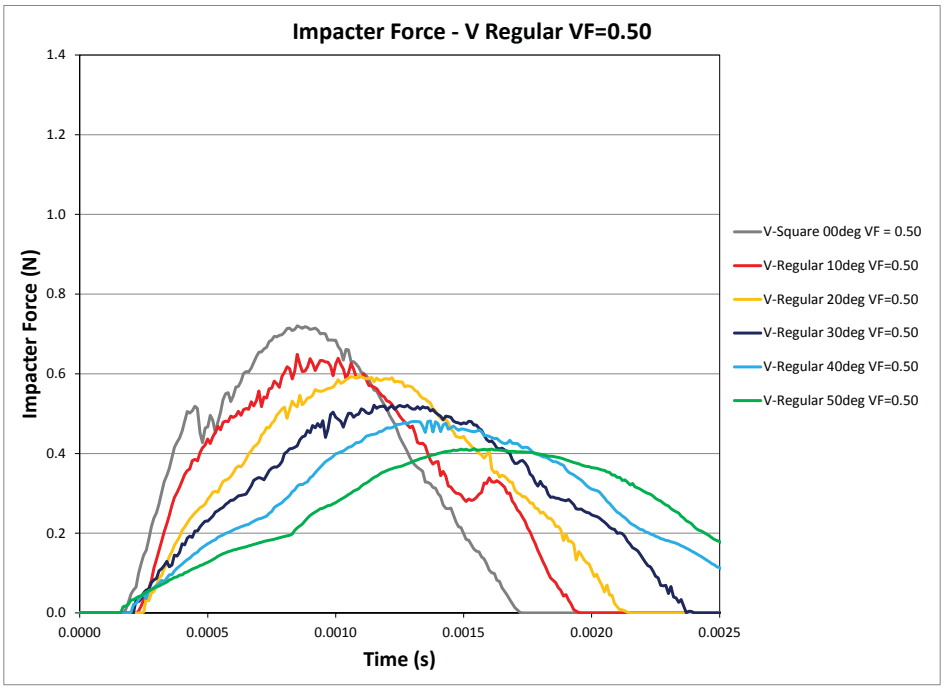

Figure 120: Impact force time histories for vertical impact of a cylindrical impacter of 2m/s on regular honeycomb specimens with void fraction of 0.5 and different angles.

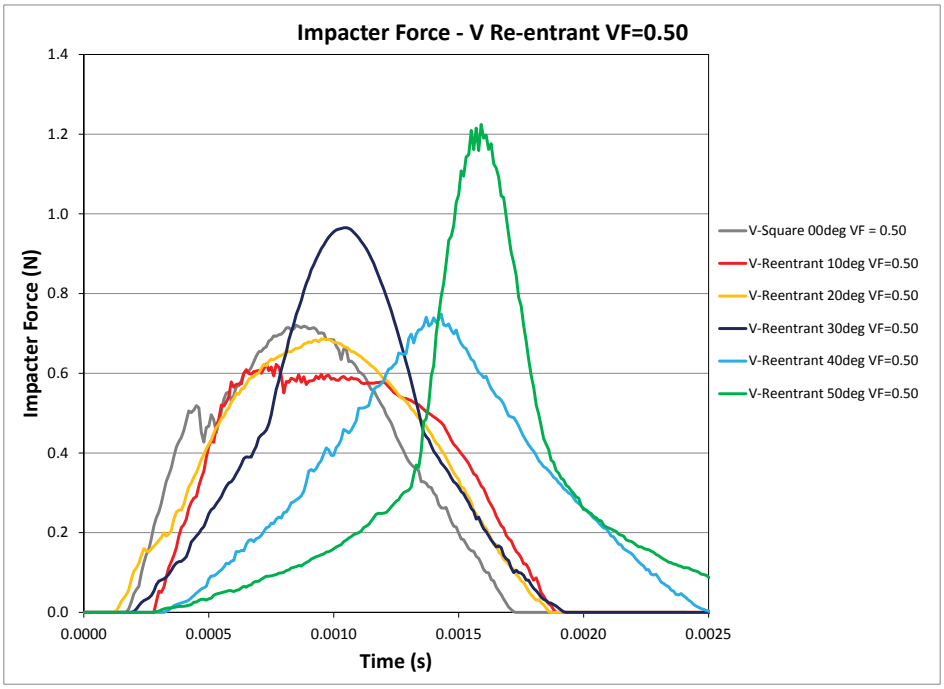

Figure 121: Impact force time histories for vertical impact of a cylindrical impacter of 2m/s on re-entrant honeycomb specimens with void fraction of 0.5 and different angles.

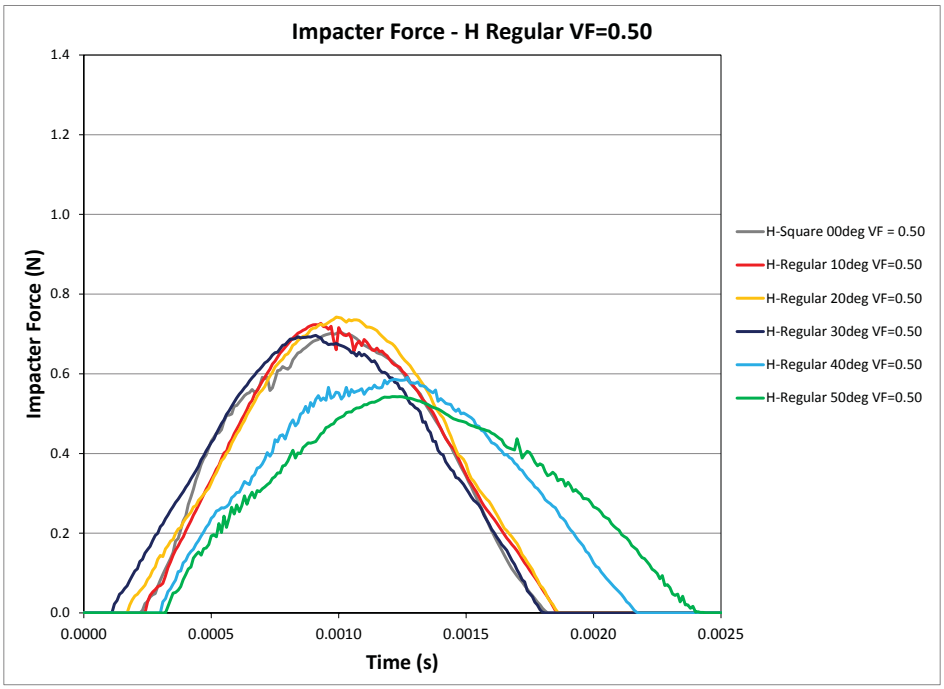

Figure 122: Impact force time histories for horizontal impact of a cylindrical impacter of 2m/s on regular honeycomb specimens with void fraction of 0.5 and different angles.

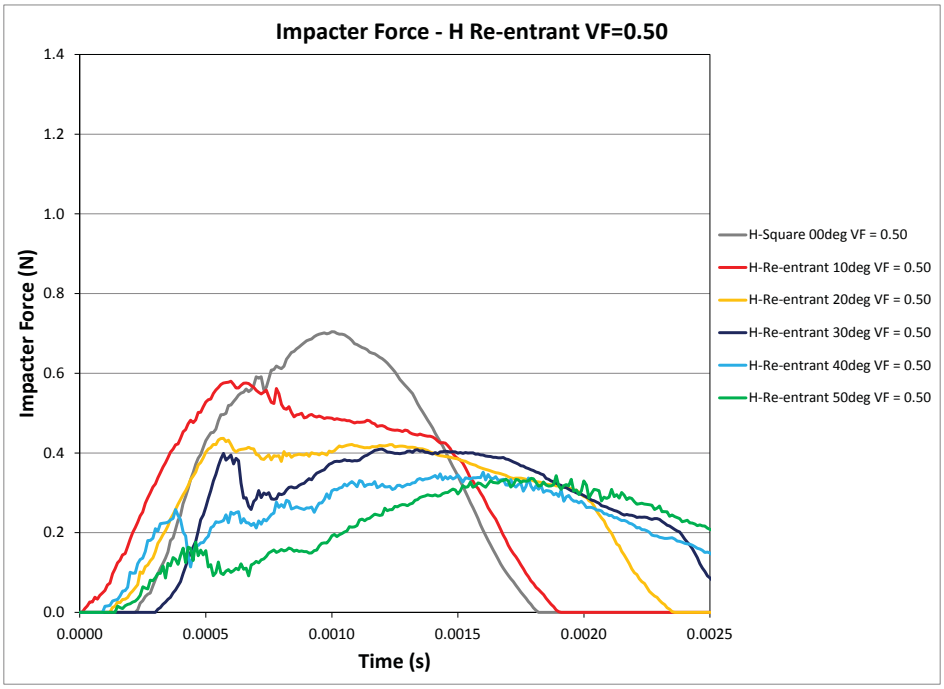

Figure 123: Impact force time histories for horizontal impact of a cylindrical impacter of 2m/s on re-entrant honeycomb specimens with void fraction of 0.5 and different angles.

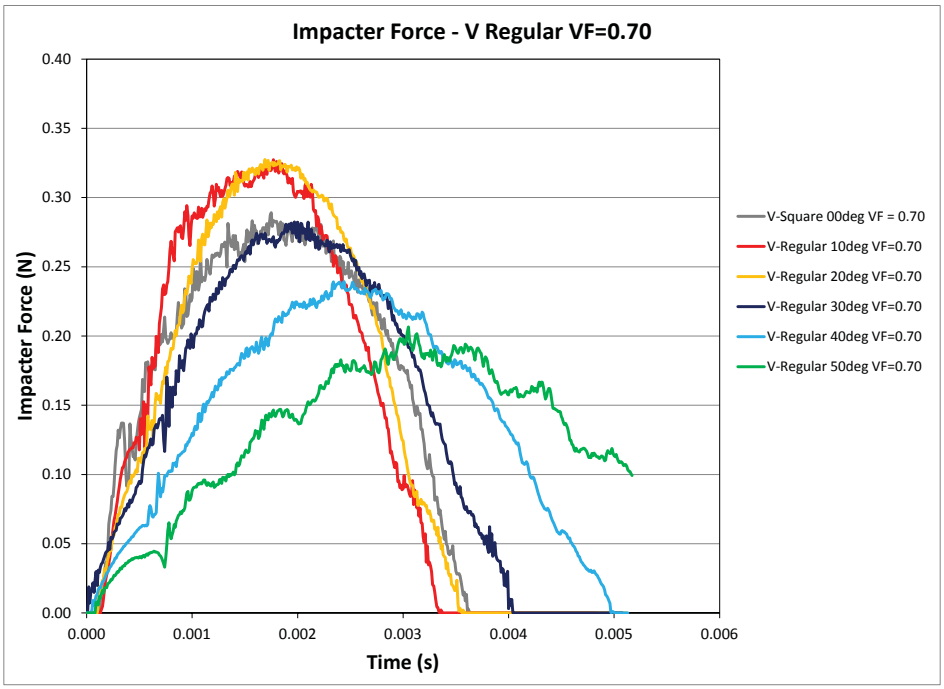

Figure 124: Impact force time histories for vertical impact of a cylindrical impacter of 2m/s on regular honeycomb specimens with void fraction of 0.7 and different angles.

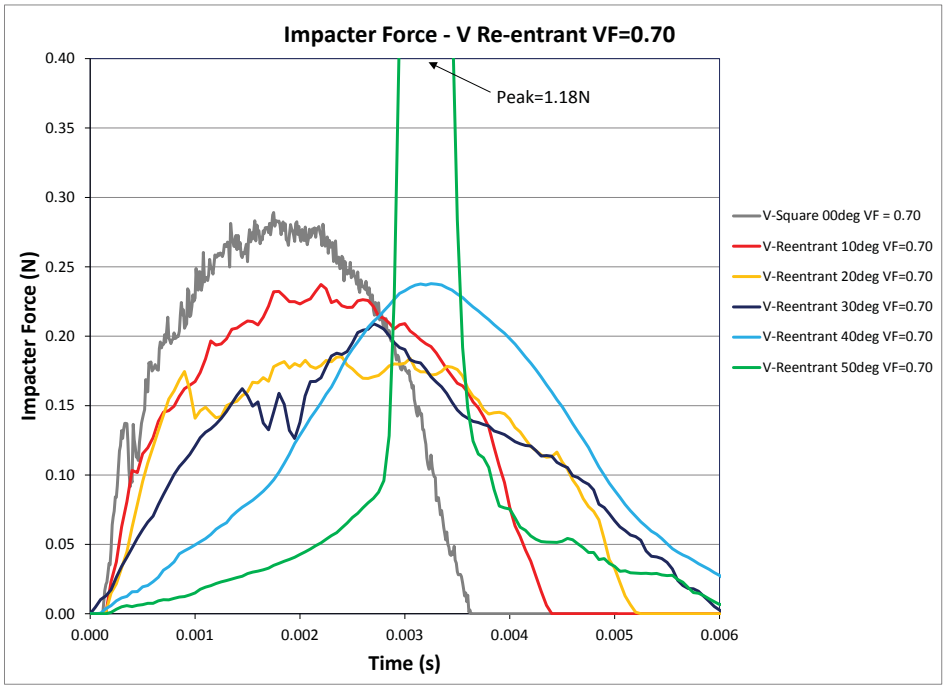

Figure 125: Impact force time histories for vertical impact of a cylindrical impacter of 2m/s on re-entrant honeycomb specimens with void fraction of 0.7 and different angles.

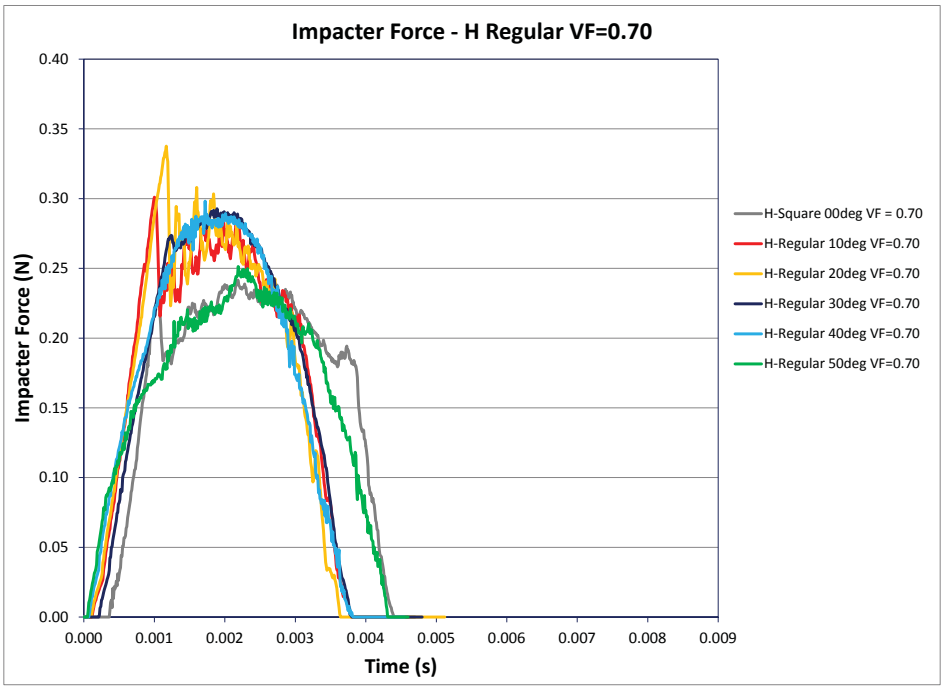

Figure 126: Impact force time histories for horizontal impact of a cylindrical impacter of 2m/s on regular honeycomb specimens with void fraction of 0.7 and different angles.

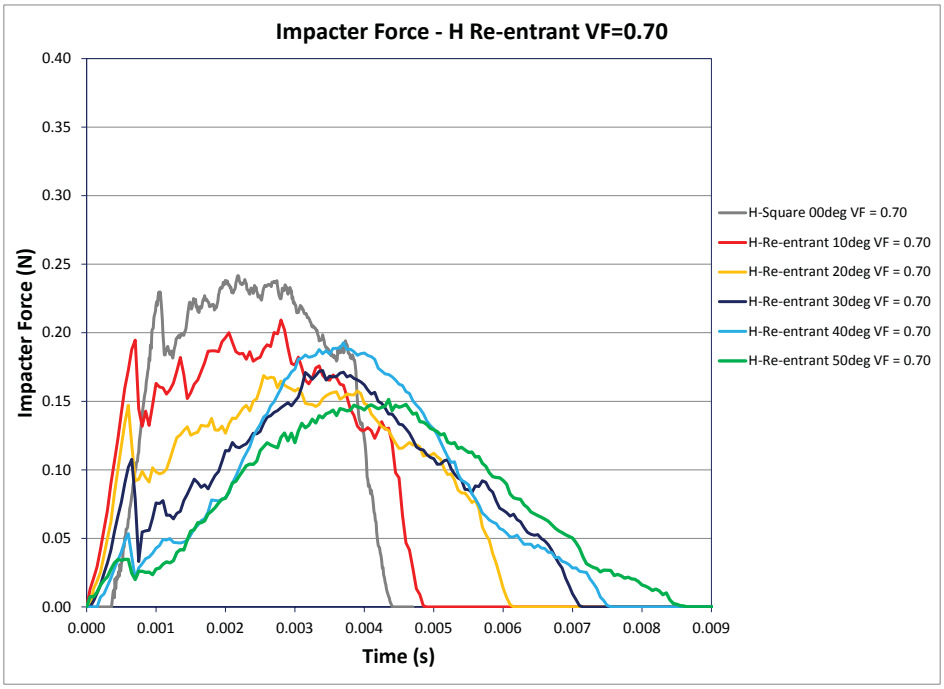

Figure 127: Impact force time histories for horizontal impact of a cylindrical impacter of 2m/s on re-entrant honeycomb specimens with void fraction of 0.7 and different angles.

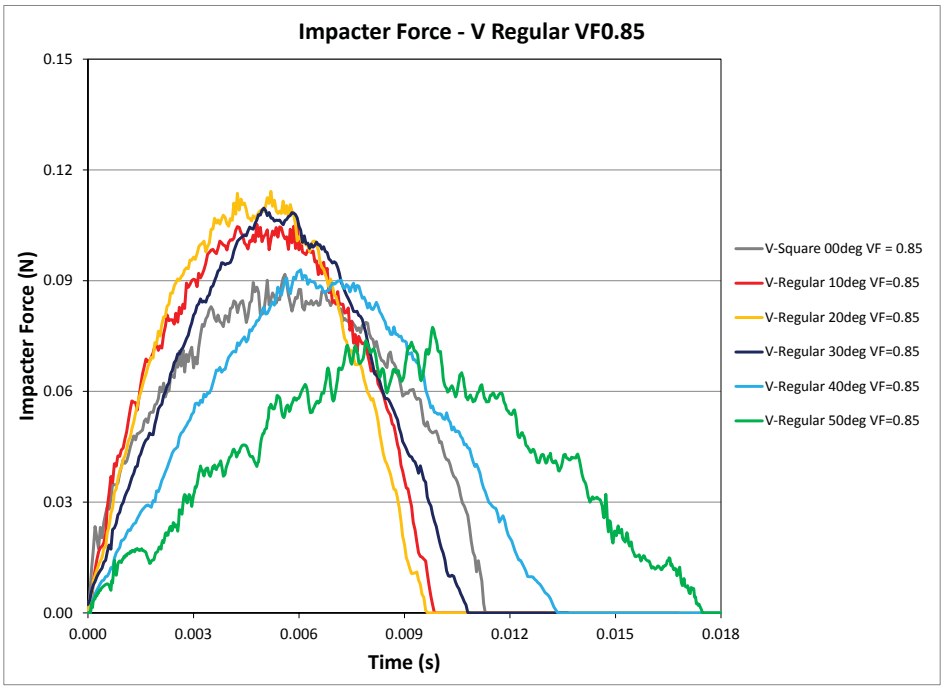

Figure 128: Impact force time histories for vertical impact of a cylindrical impacter of 2m/s on regular honeycomb specimens with void fraction of 0.85 and different angles.

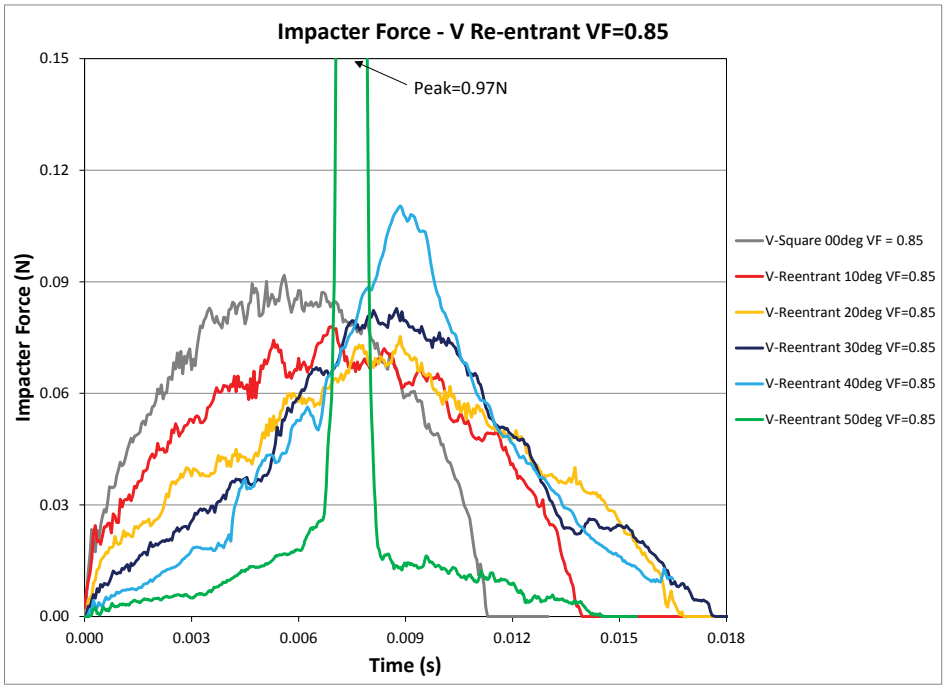

Figure 129: Impact force time histories for vertical impact of a cylindrical impacter of 2m/s on re-entrant honeycomb specimens with void fraction of 0.85 and different angles.

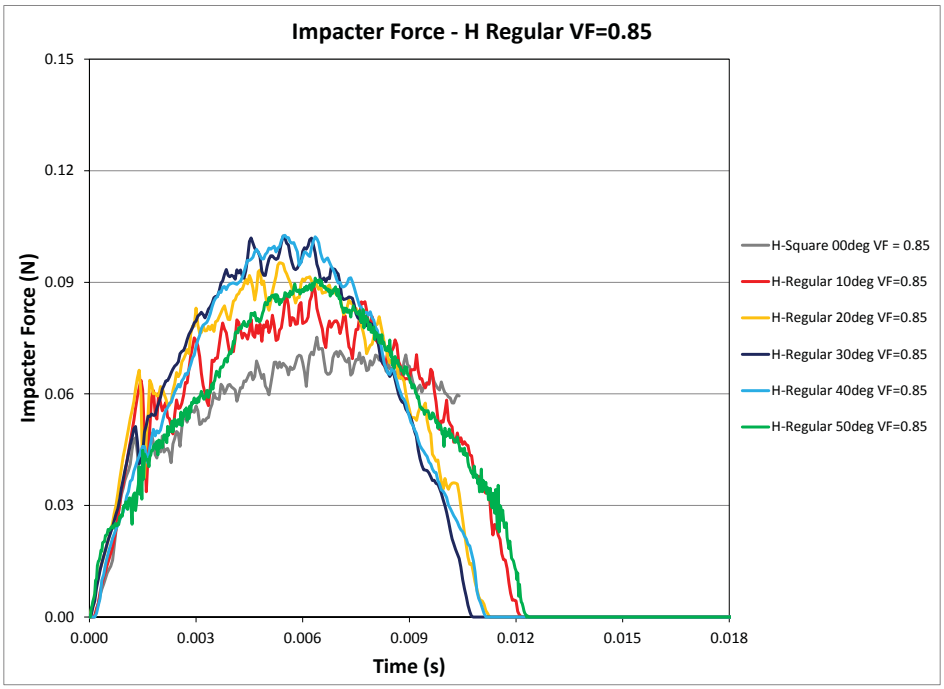

Figure 130: Impact force time histories for horizontal impact of a cylindrical impacter of 2m/s on regular honeycomb specimens with void fraction of 0.85 and different angles.

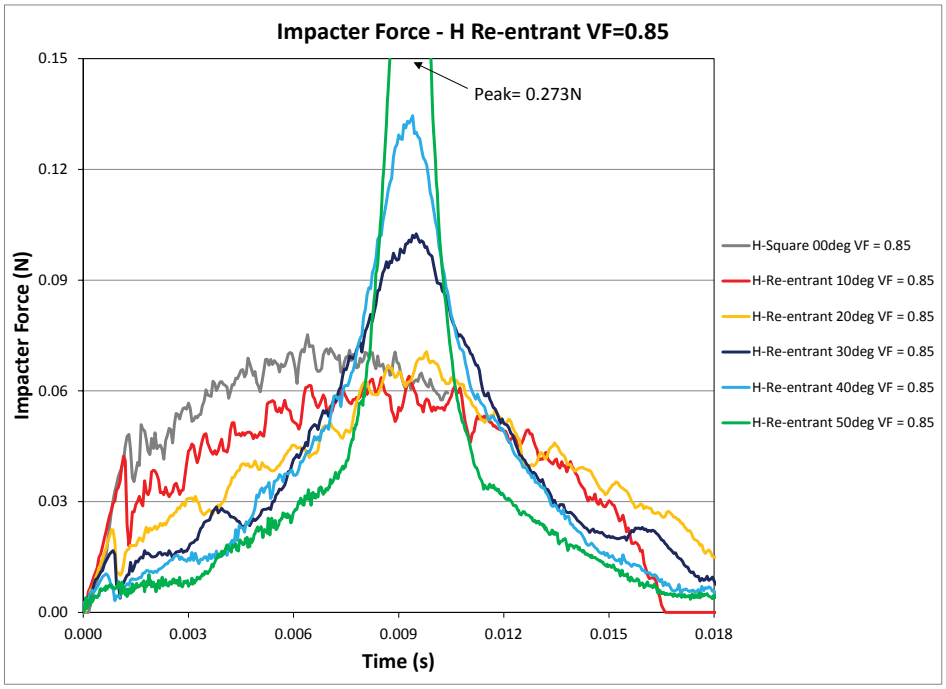

Figure 131: Impact force time histories for horizontal impact of a cylindrical impacter of 2m/s on re-entrant honeycomb specimens with void fraction of 0.85 and different angles.

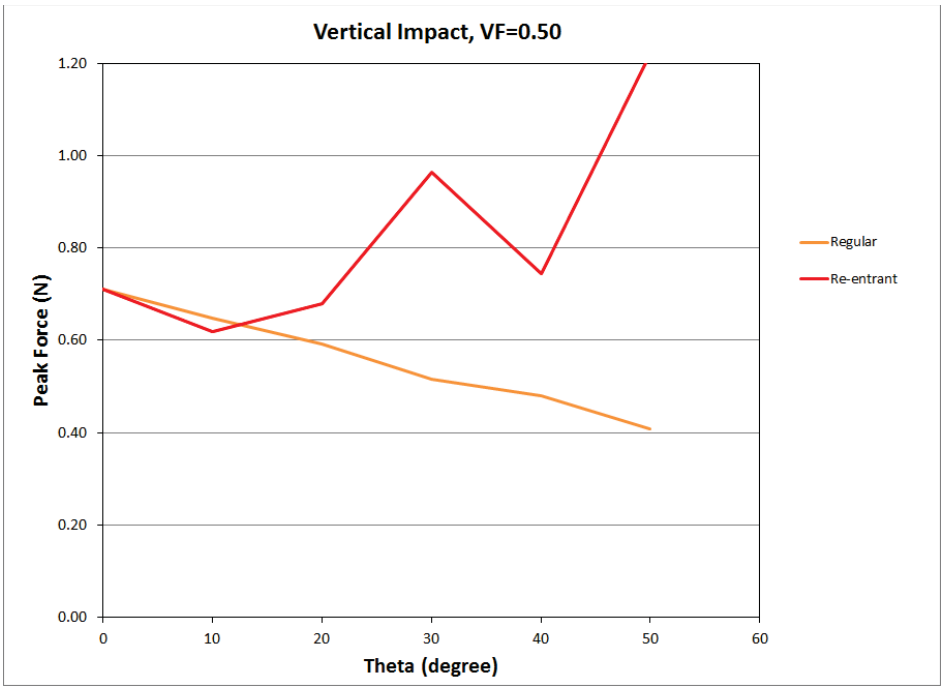

Figure 132: Peak impact force vs. θ for vertical impact of a cylindrical impacter of 2m/s on regular and re-entrant honeycomb specimens with void fraction of 0.5.

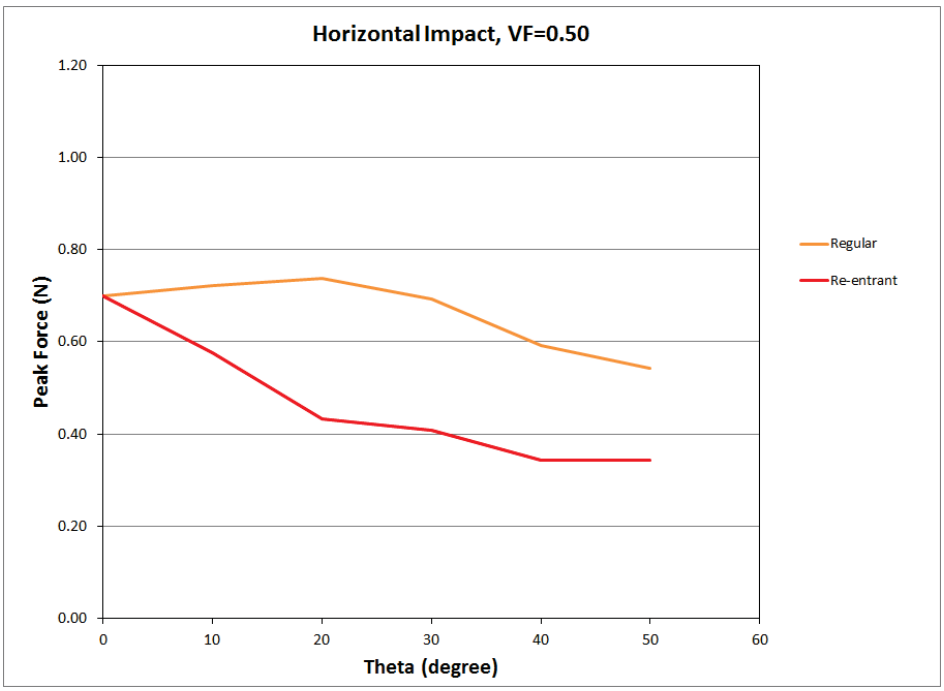

Figure 133: Peak impact force vs. θ for horizontal impact of a cylindrical impacter of 2m/s on regular and re-entrant honeycomb specimens with void fraction of 0.5.

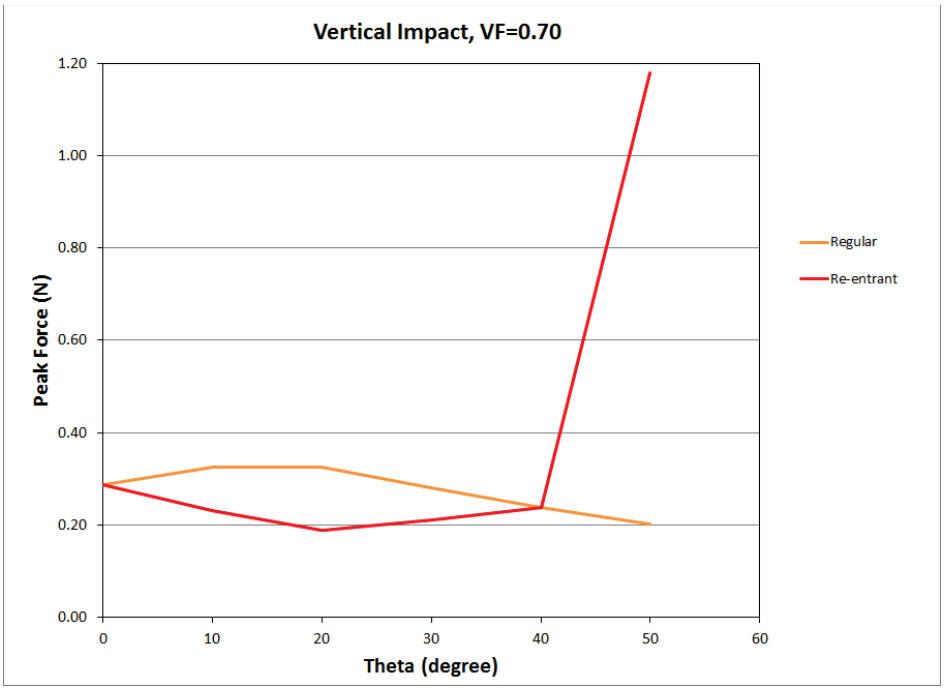

Figure 134: Peak impact force vs. θ for vertical impact of a cylindrical impacter of 2m/s on regular and re-entrant honeycomb specimens with void fraction of 0.7.

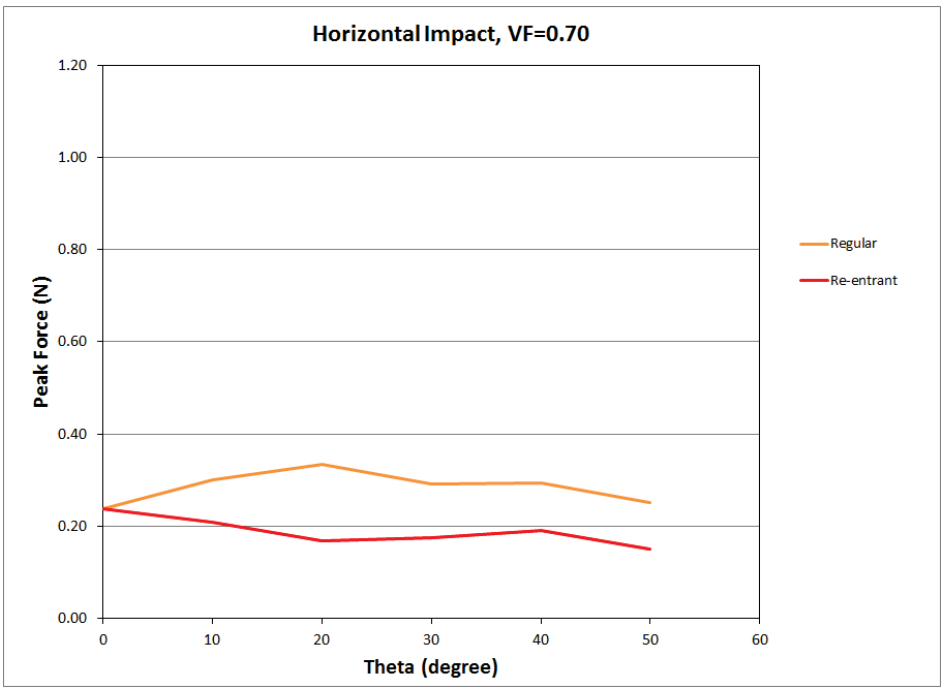

Figure 135: Peak impact force vs. θ for horizontal impact of a cylindrical impacter of 2m/s on regular and re-entrant honeycomb specimens with void fraction of 0.7.

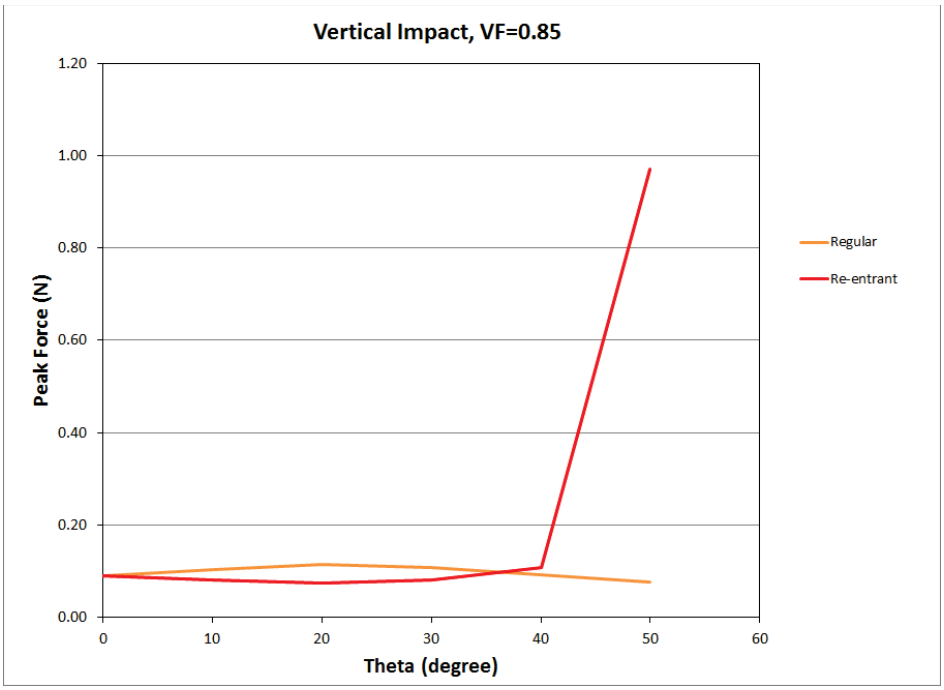

Figure 136: Peak impact force vs. θ for vertical impact of a cylindrical impacter of 2m/s on regular and re-entrant honeycomb specimens with void fraction of 0.85.

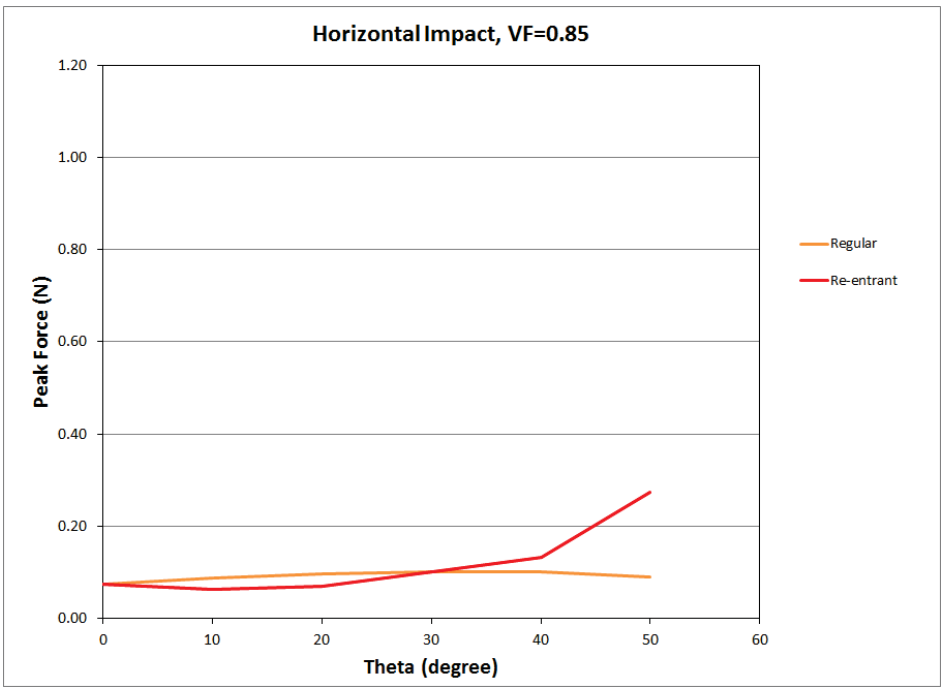

Figure 137: Peak impact force vs. θ for horizontal impact of a cylindrical impacter of 2m/s on regular and re-entrant honeycomb specimens with void fraction of 0.85.

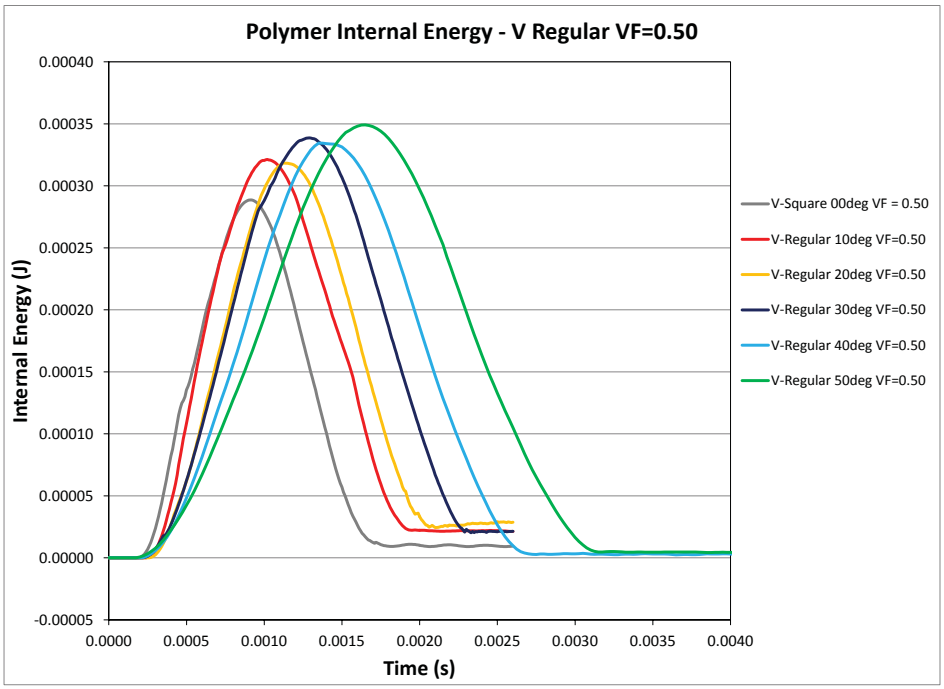

Figure 138: Internal energy time histories for vertical impact of a cylindrical impacter of 2m/s on regular honeycomb specimens with void fraction of 0.5 and different angles.

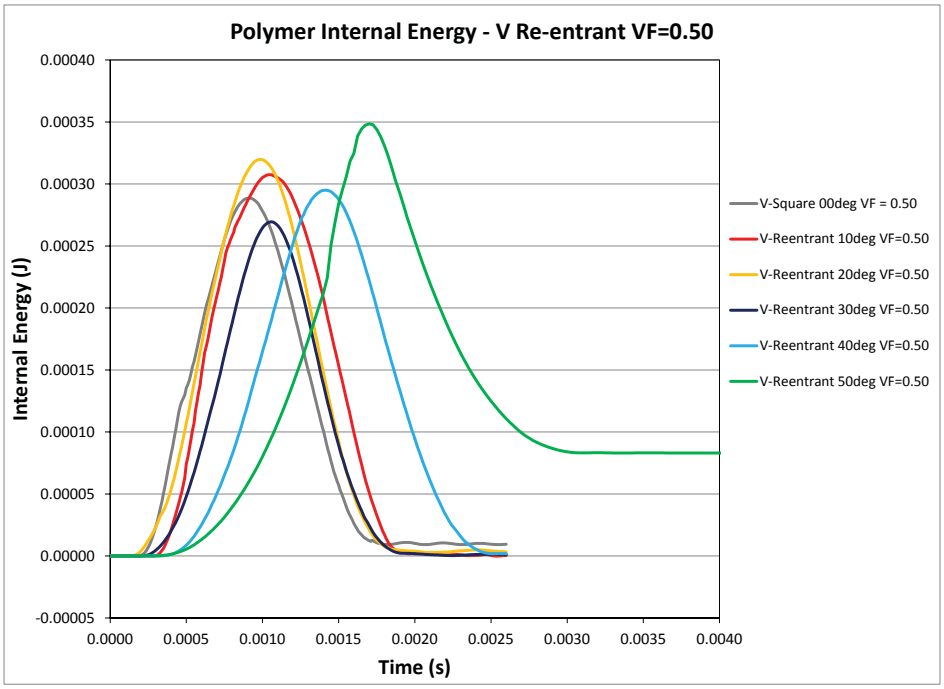

Figure 139: Internal energy time histories for vertical impact of a cylindrical impacter of 2m/s on re-entrant honeycomb specimens with void fraction of 0.5 and different angles.

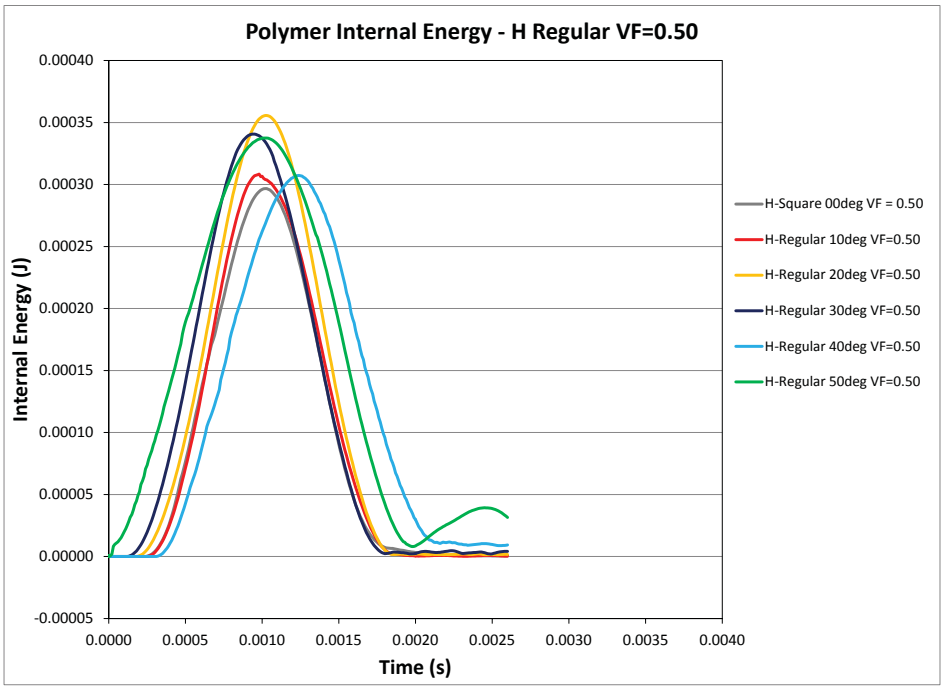

Figure 140: Internal energy time histories for horizontal impact of a cylindrical impacter of 2m/s on regular honeycomb specimens with void fraction of 0.5 and different angles.

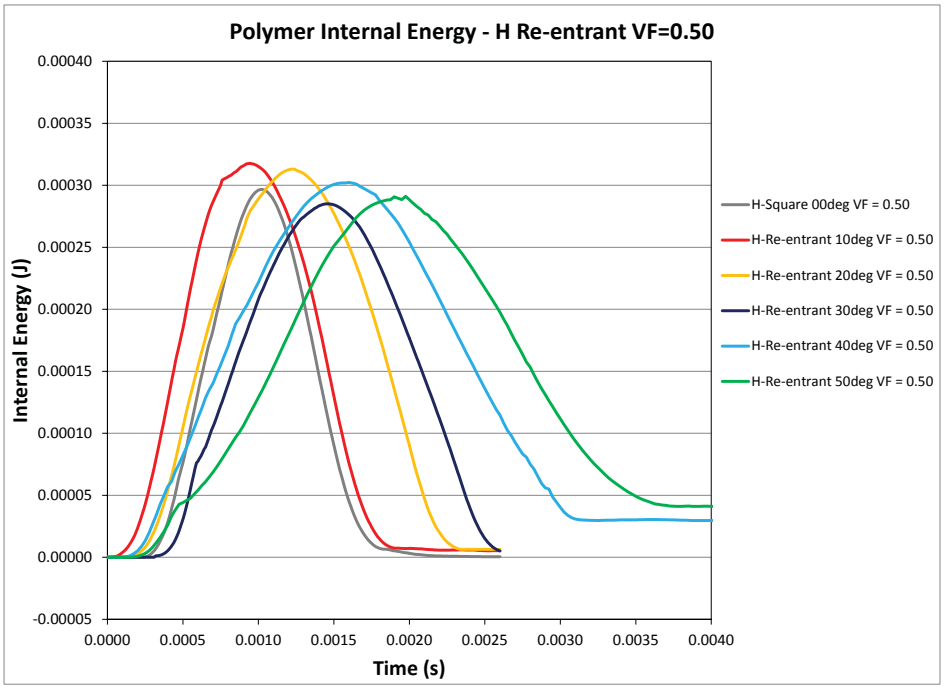

Figure 141: Internal energy time histories for horizontal impact of a cylindrical impacter of 2m/s on re-entrant honeycomb specimens with void fraction of 0.5 and different angles.

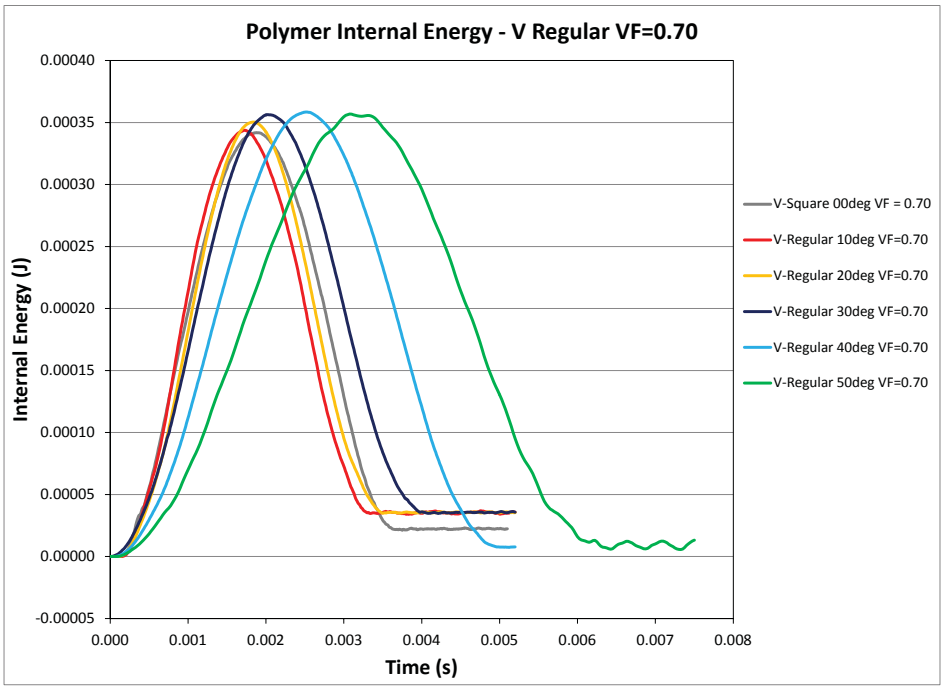

Figure 142: Internal energy time histories for vertical impact of a cylindrical impacter of 2m/s on regular honeycomb specimens with void fraction of 0.7 and different angles.

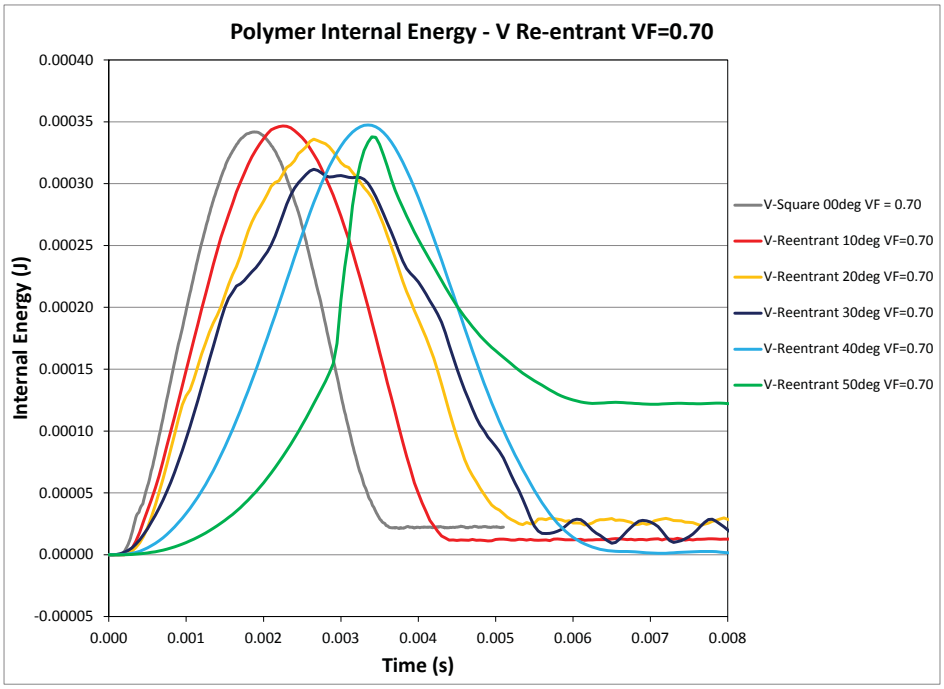

Figure 143: Internal energy time histories for vertical impact of a cylindrical impacter of 2m/s on re-entrant honeycomb specimens with void fraction of 0.7 and different angles.

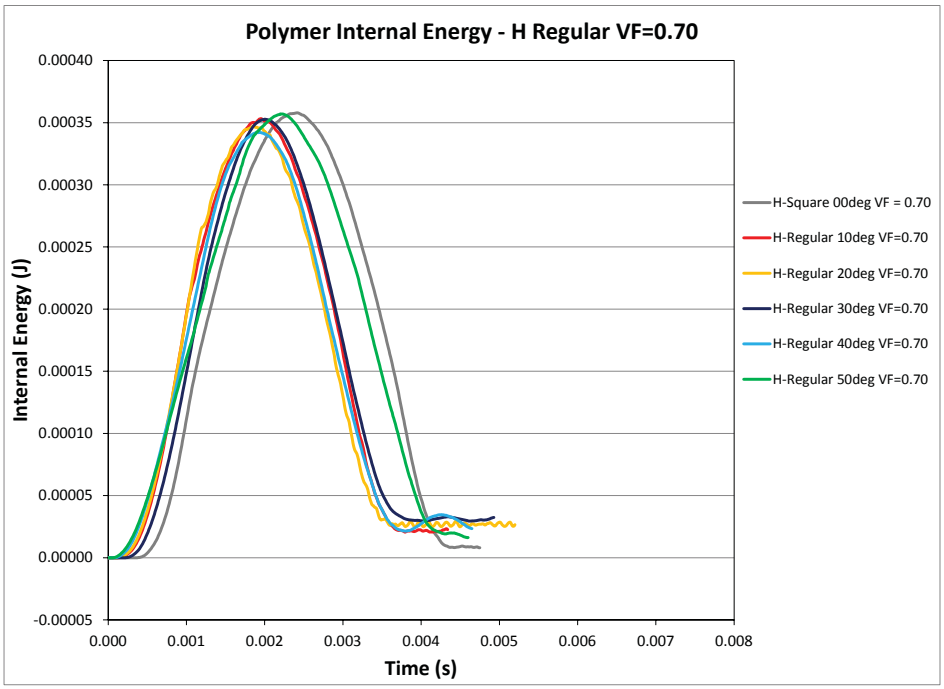

Figure 144: Internal energy time histories for horizontal impact of a cylindrical impacter of 2m/s on regular honeycomb specimens with void fraction of 0.7 and different angles.

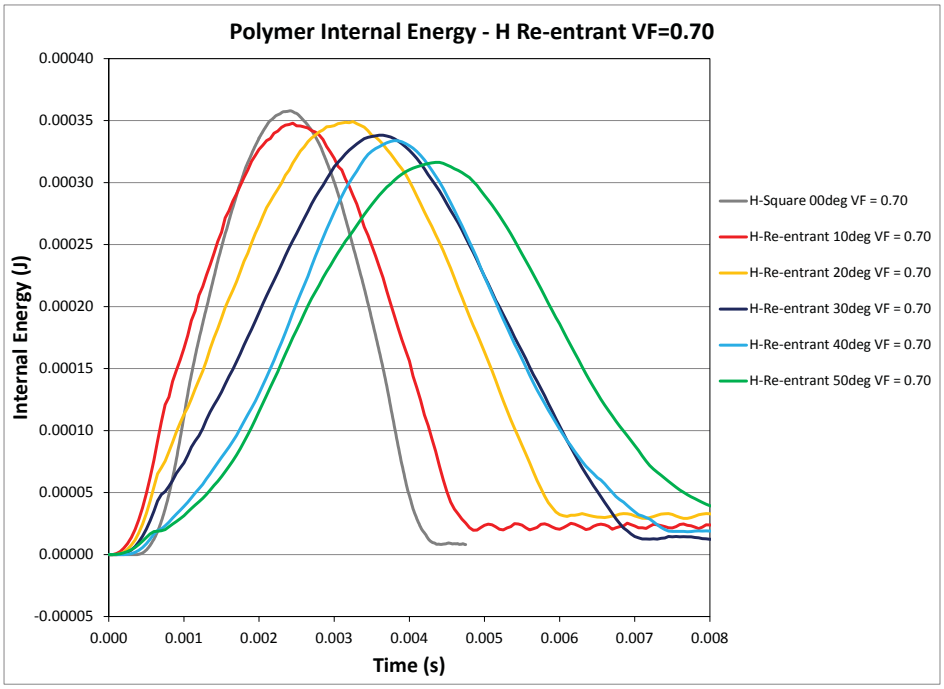

Figure 145: Internal energy time histories for horizontal impact of a cylindrical impacter of 2m/s on re-entrant honeycomb specimens with void fraction of 0.7 and different angles.

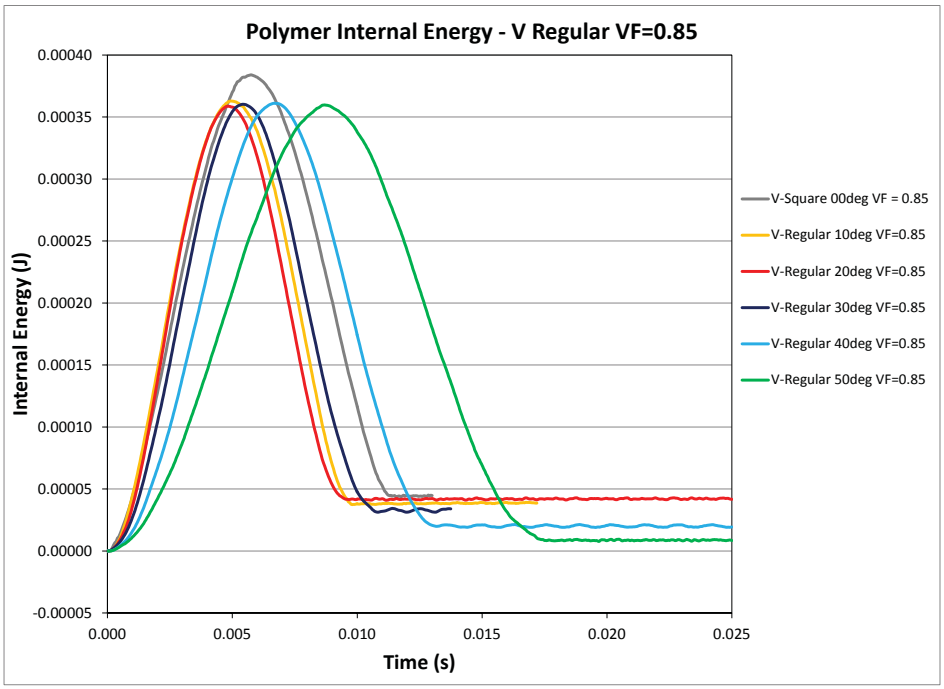

Figure 146: Internal energy time histories for vertical impact of a cylindrical impacter of 2m/s on regular honeycomb specimens with void fraction of 0.85 and different angles.

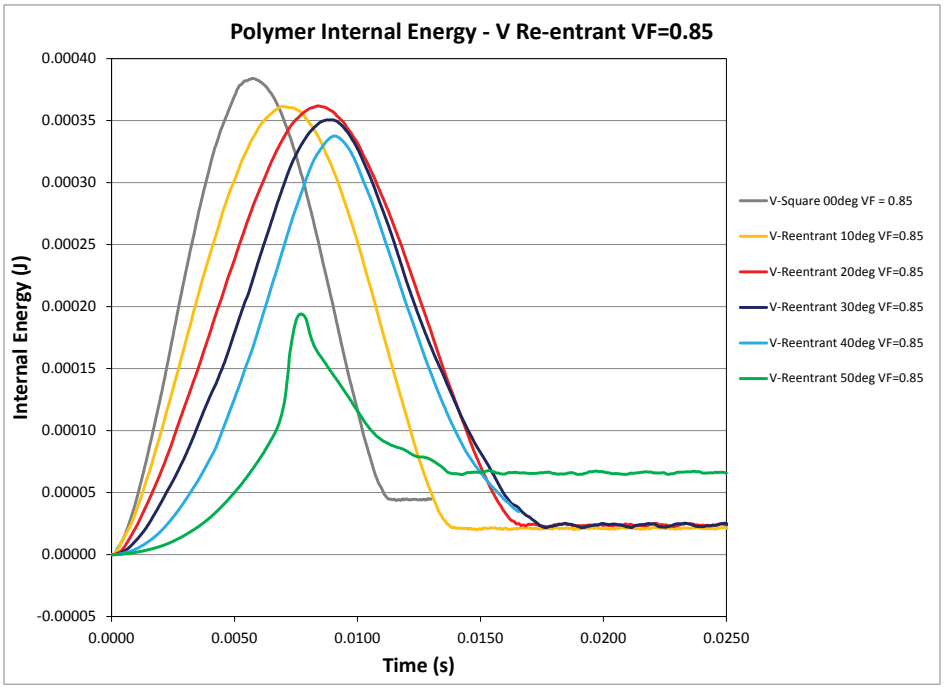

Figure 147: Internal energy time histories for vertical impact of a cylindrical impacter of 2m/s on re-entrant honeycomb specimens with void fraction of 0.85 and different angles.

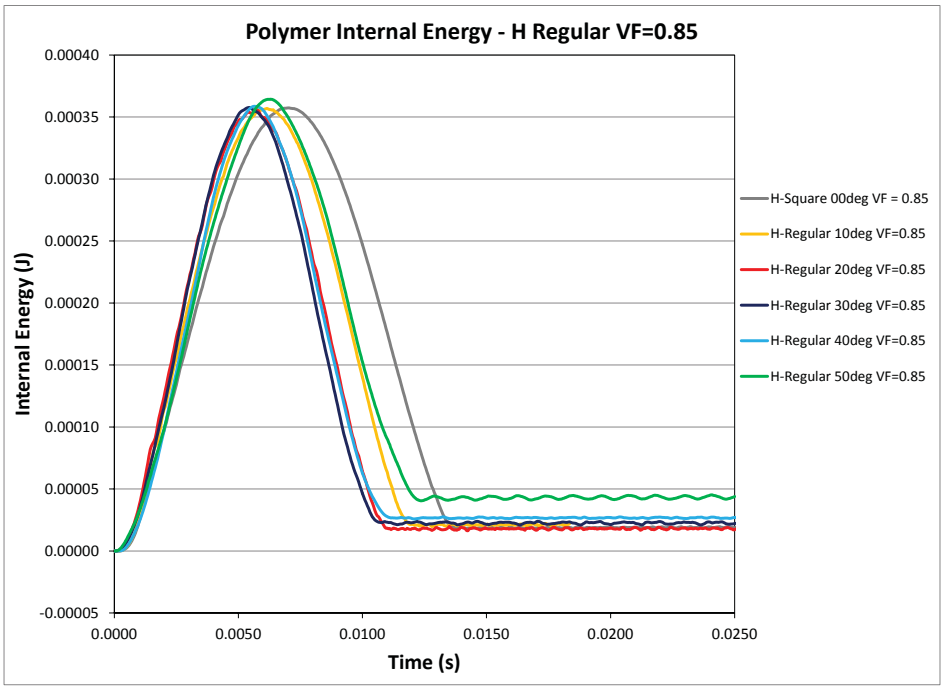

Figure 148: Internal energy time histories for horizontal impact of a cylindrical impacter of 2m/s on regular honeycomb specimens with void fraction of 0.85 and different angles.

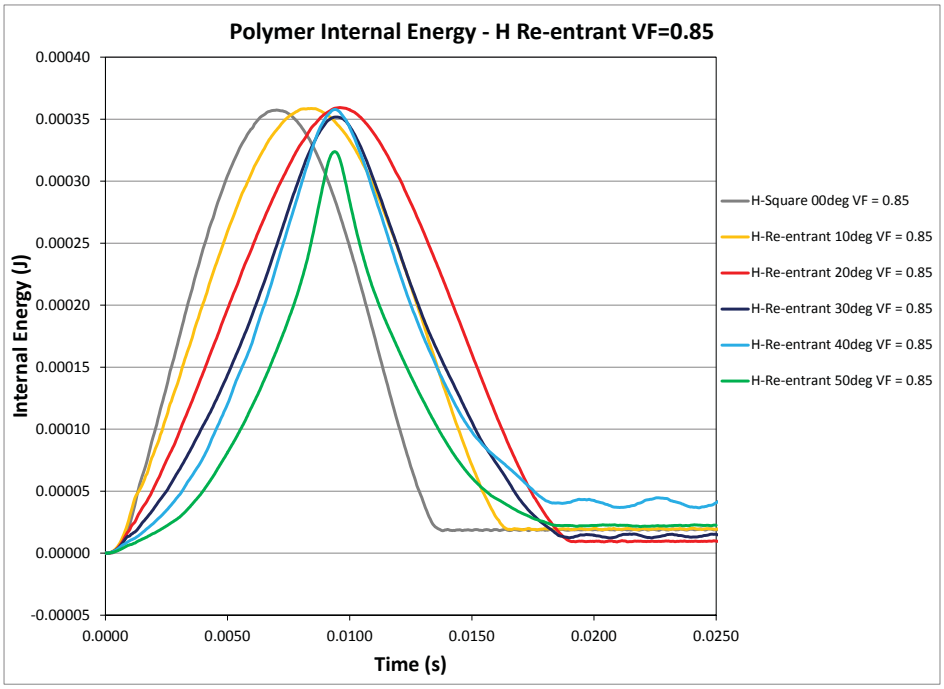

Figure 149: Internal energy time histories for horizontal impact of a cylindrical impacter of 2m/s on re-entrant honeycomb specimens with void fraction of 0.85 and different angles.

6 Parametric Study for Partial Compression of Auxetic Materials on a Substrate

In this chapter, we extended our previous model for local impact study to include a substrate. The purpose of this extension was to investigate the force transmitted to the substrate during the impact event. The layout of the extended model is present in Figure 144. In this model, the cylindrical impacter and material samples were all identical to those in the previous parametric study. However, the rigid constraints applied on the bottom of the sample were replaced by a rigid mass which represented the substrate. This rigid mass was free to move in the vertical (Z) direction. The advantage of this setup was that it permitted direct evaluation of the total force transmitted to the substrate by applying the same procedure used before for obtaining the impacter force. In this procedure, the displacement time history of the rigid impacter was first differentiated twice to obtain the acceleration and the acceleration was then multiplied by the mass to produce the impact force. Because in the current parametric study, the same areal density was used for all material samples, the magnitude of the transmitted force was believed to be an excellent indicator on the relative protective performance of the various conventional and re-entrant material samples.

In the finite element models, the bottom nodes of the material samples were connected to the substrate through multi-point constraints in the Z-direction, but were allowed to slide freely in the X-direction. These boundary conditions were also consistent with those employed in the previous parametric studies.

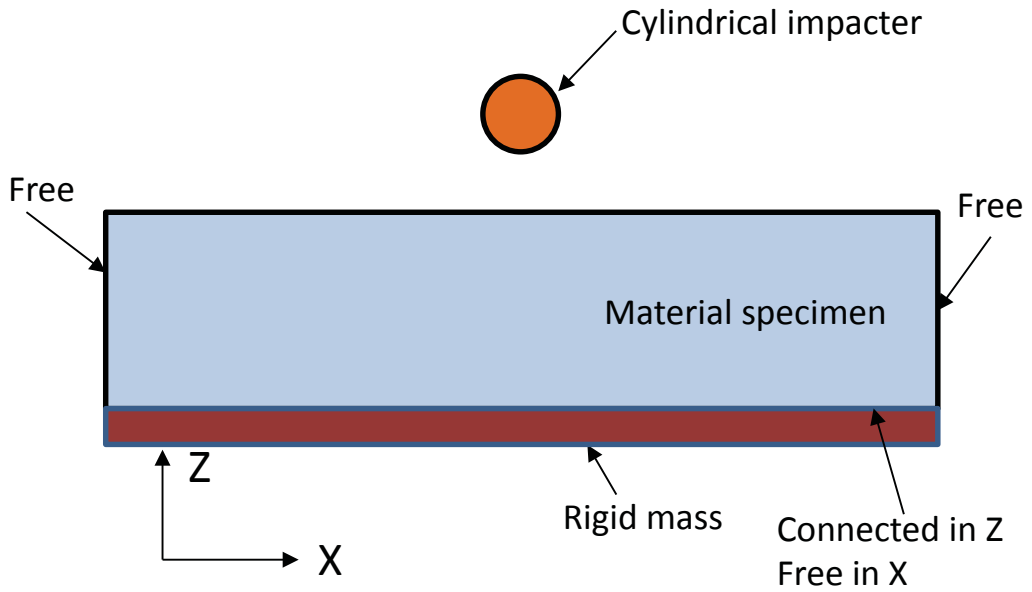

Figure 150: Problem setup for parametric study for partial compression of auxetic materials on a substrate.

Same as the previous parametric study for local impact, the mass of the cylindrical impacter was taken as 10 times of the mass of the material samples. The bottom rigid mass that represented the substrate was set to be 50 times of the sample mass, so that the substrate provided a strong vertical support to the specimens due to its inertial effect. The initial impacter speed of 2 m/s was again applied.

After some verification runs to confirm the validity of the finite element model, a parametric study was conducted to determine the total force transmitted to the substrate for different material samples. The same sample material types were considered in the present parametric study, but only the vertical impact cases were analyzed here.

Upon the completion of the finite element simulations, deformed configurations predicted for all test cases were again examined to ensure the stability of the numerical solutions. The results for two representative cases are presented in Figures 145 and 146. The deformed configurations are very similar to those obtained for the corresponding cases in the previous parametric study, as shown in Figures 117 and 119. The only significant difference was that in the present solutions, the sample materials moved downwards upon the release of the impacter. This is because in the present analyses, the rigid mass attached to the bottom of the material sample was accelerated during the impact event.

The time histories of the impact force and the total force transmitted to the substrate were then formed using the procedure described above and the time histories of the polymer internal energy were extracted using the post-processing capability provided with LS-DYNA. These results are presented in Figures 147 to 164. By examining these results, we realized that the profiles of the impact force predicted in the present parametric study are very similar to those obtained in the previous parametric study in which the material samples were supported by a rigid plate. This agreed with our expectations because the inertial effect of the heavy substrate generated strong supports to the material samples in the vertical (Z) direction.

Comparing the time histories of the impact force and the total force transmitted to the substrate, we noticed that the magnitudes of the forces applied on substrate were very similar to those of the impact forces, but they pointed to opposite directions. The only difference was that the forces on the substrate contained more significant high-frequency noises which were probably caused by the penalty stiffness introduced in the multi-point constraints. The equality between the impacter force and the force acting on the substrate suggested that all the trends observed on the impacter force can be directly applied to form guidelines for identifying the preferred material types as protective layers on substrates. For instance: if re-entrant material layers are to be used to protect the substrate from impact damage, material types with large angle θ, such as 50^{O}, should be avoided as these materials generate less resistance at the beginning of the transient which might result in large peak force on the substrate later. On the other hand, if conventional honeycomb materials are to be used as protective layers, materials with larger angles maybe preferred as they result in lower forces on the substrate, accompanied by longer impact durations.

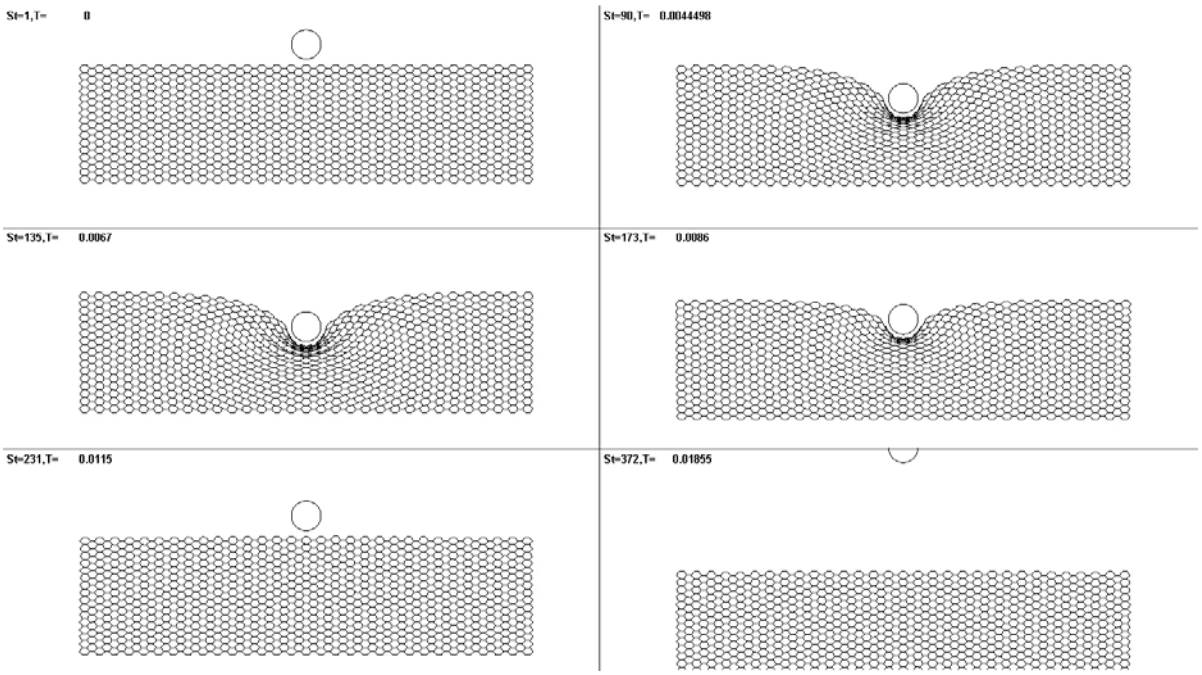

Figure 151: Original and deformed configurations of a re-entrant honeycomb sample (VF=0.85, θ=40^o) on a substrate subject to vertical impact of a cylindrical impacter at 2m/s.

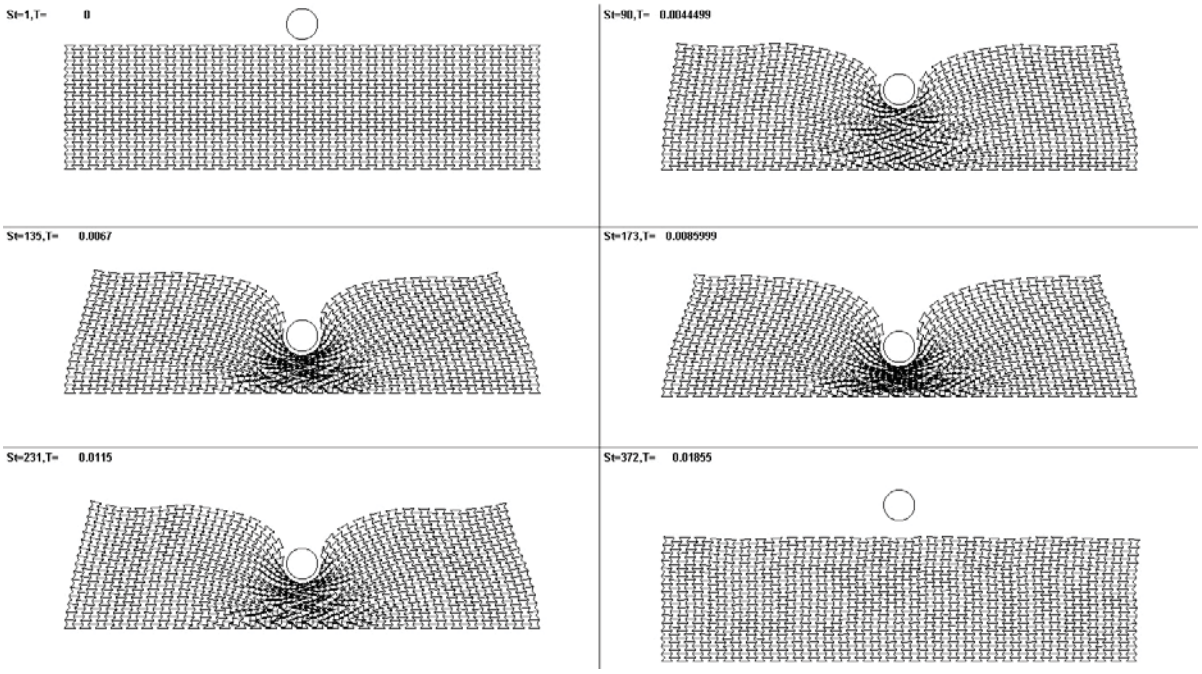

Figure 152: Original and deformed configurations of a re-entrant honeycomb sample (VF=0.85, θ=40^o) on a substrate subject to vertical impact of a cylindrical impacter at 2m/s.

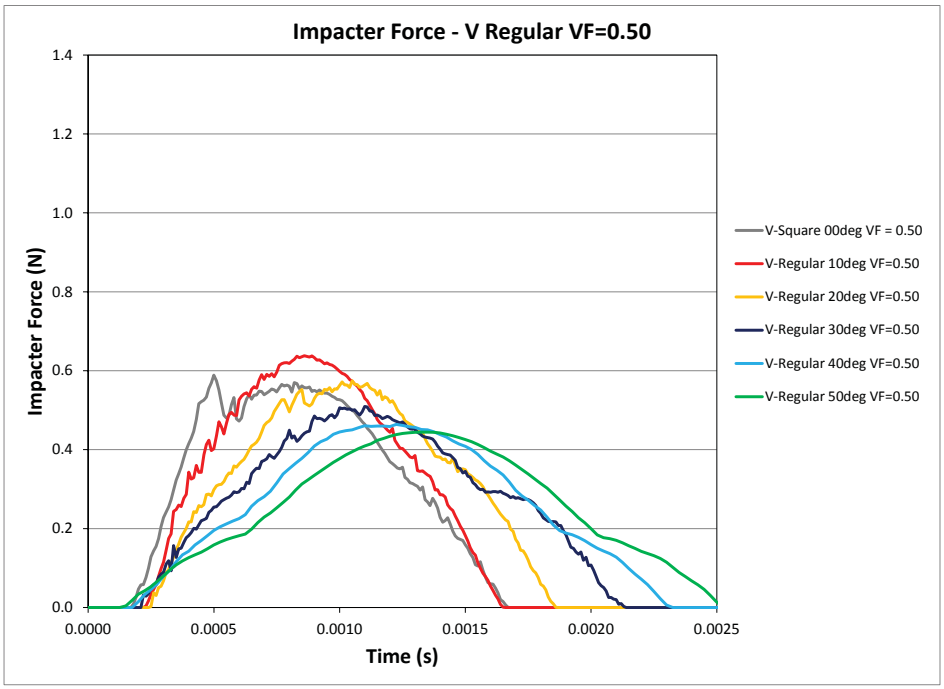

Figure 153: Impact force time histories for vertical impact of a cylindrical impacter of 2m/s on regular honeycomb specimens with void fraction of 0.5 and different angles on a substrate.

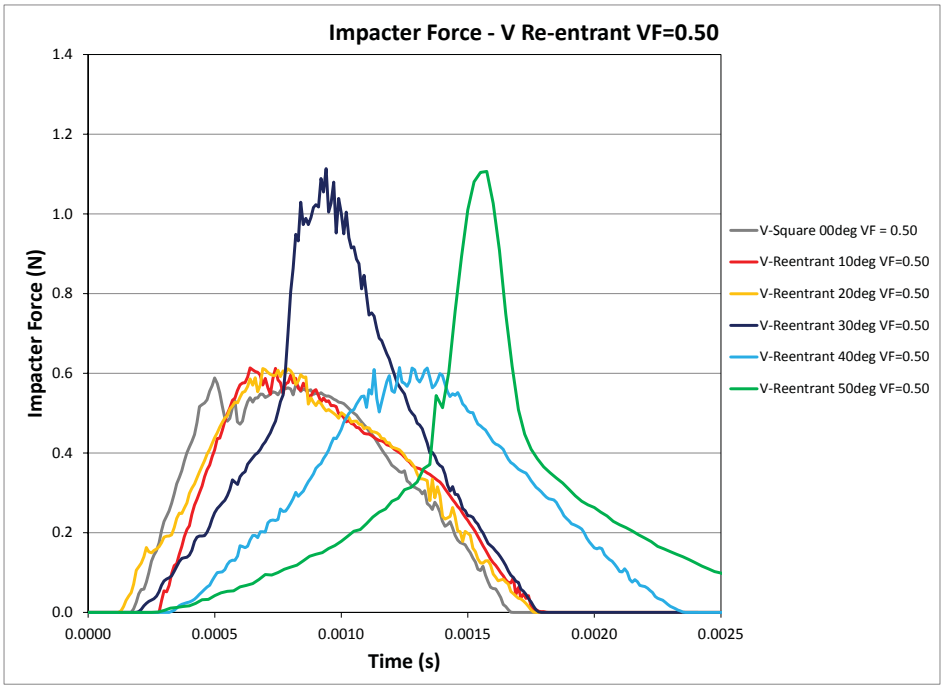

Figure 154: Impact force time histories for vertical impact of a cylindrical impacter of 2m/s on re-entrant honeycomb specimens with void fraction of 0.5 and different angles on a substrate.

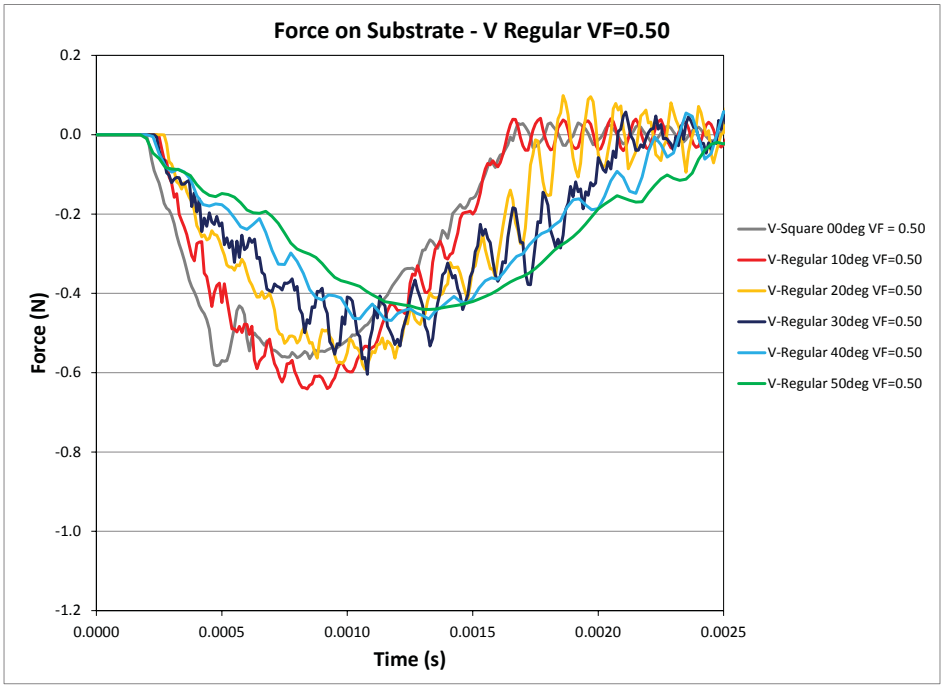

Figure 155: Dynamic force on substrate for vertical impact of a cylindrical impacter of 2m/s on regular honeycomb specimens with void fraction of 0.5 and different angles on a substrate.

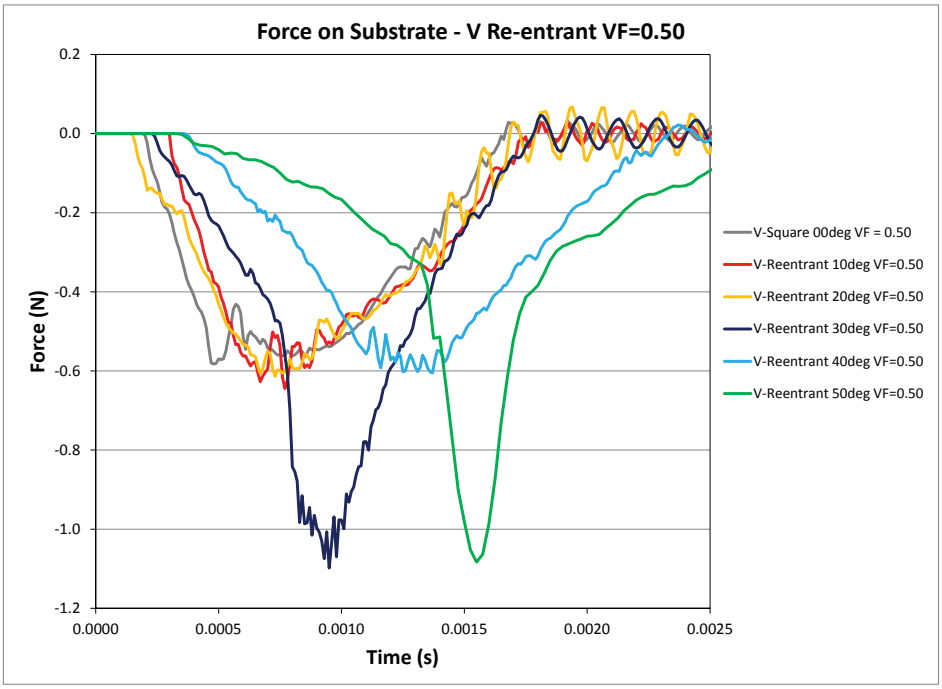

Figure 156: Dynamic force on substrate for vertical impact of a cylindrical impacter of 2m/s on re-entrant honeycomb specimens with void fraction of 0.5 and different angles on a substrate.

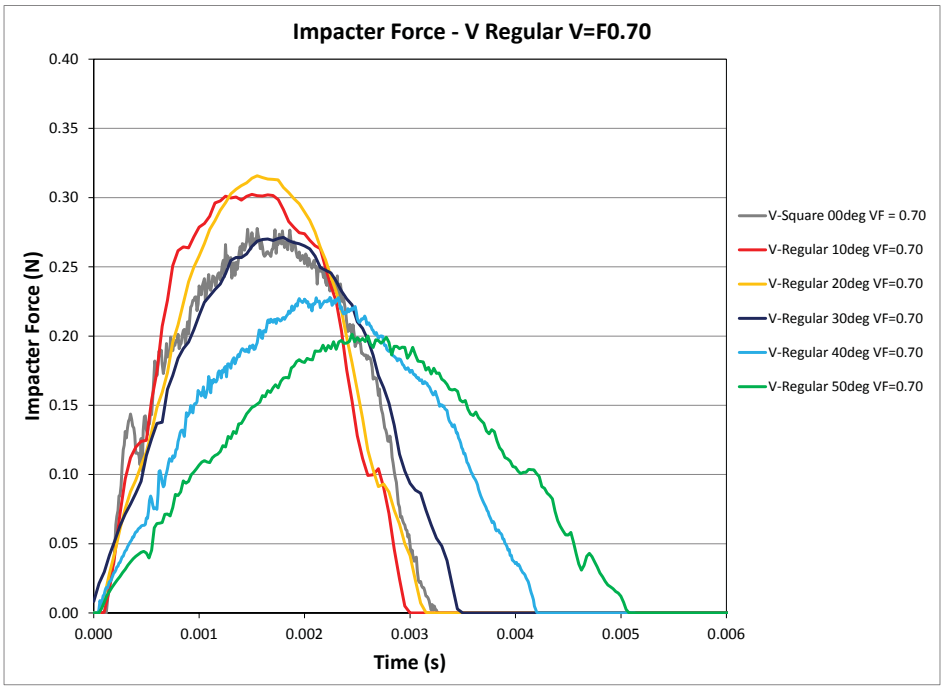

Figure 157: Impact force time histories for vertical impact of a cylindrical impacter of 2m/s on regular honeycomb specimens with void fraction of 0.7 and different angles on a substrate.

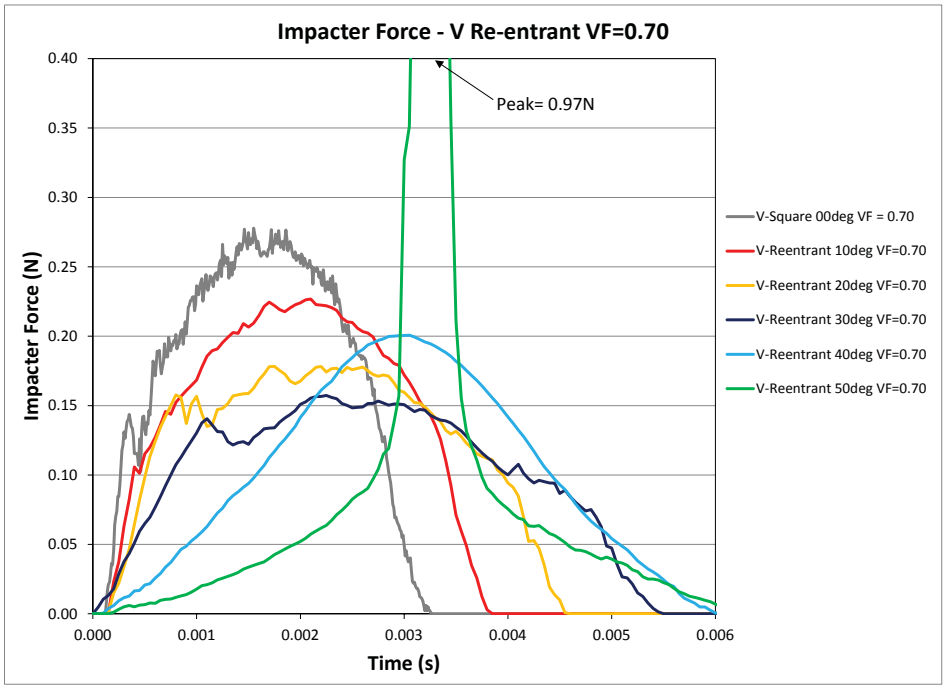

Figure 158: Impact force time histories for vertical impact of a cylindrical impacter of 2m/s on re-entrant honeycomb specimens with void fraction of 0.7and different angles on a substrate.

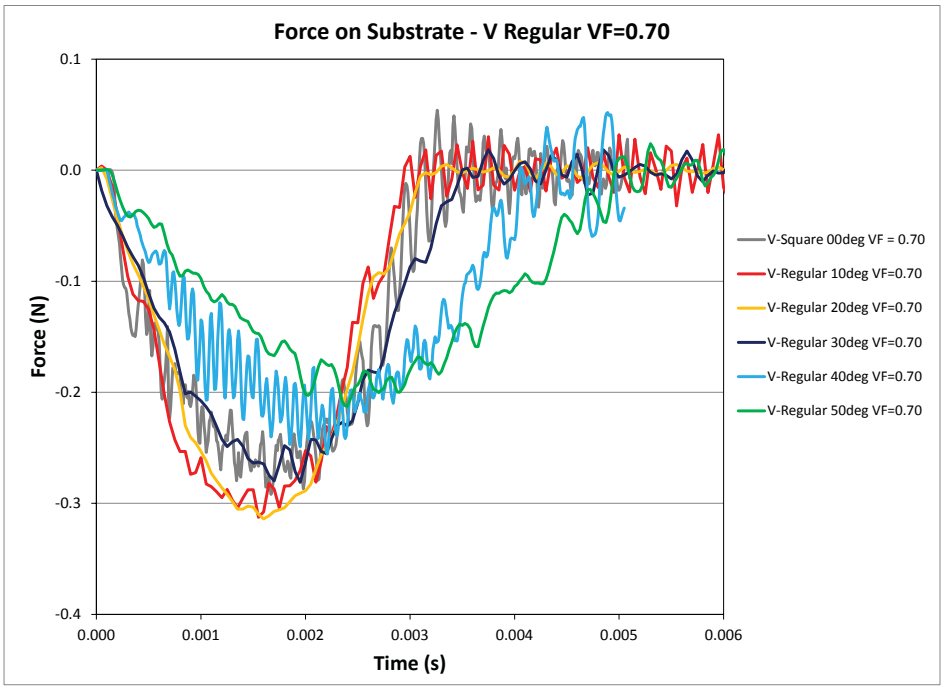

Figure 159: Dynamic force on substrate for vertical impact of a cylindrical impacter of 2m/s on regular honeycomb specimens with void fraction of 0.7 and different angles on a substrate.

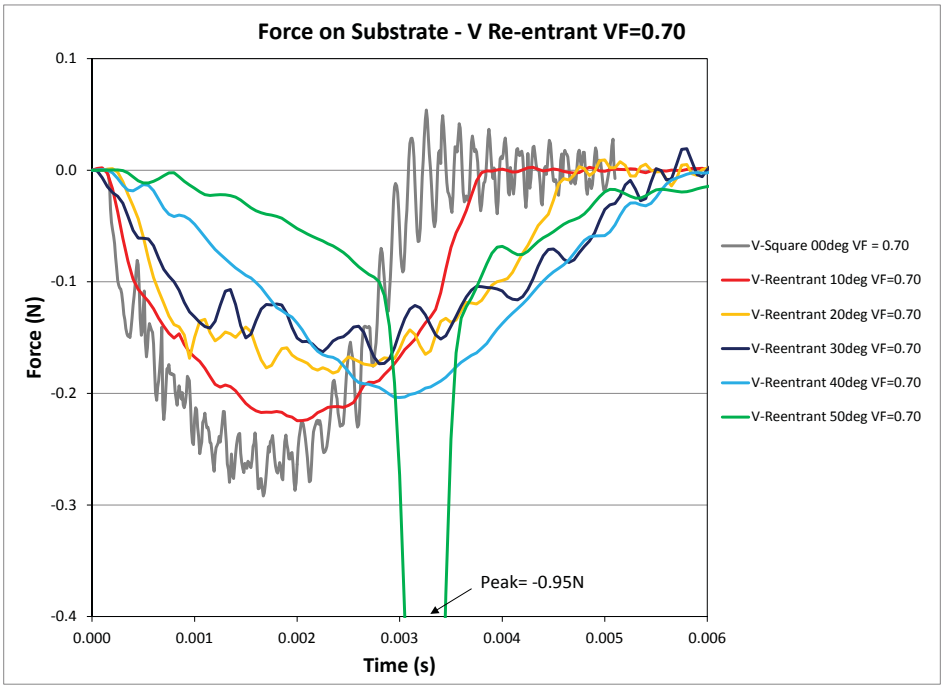

Figure 160: Dynamic force on substrate for vertical impact of a cylindrical impacter of 2m/s on re-entrant honeycomb specimens with void fraction of 0.7 and different angles on a substrate.

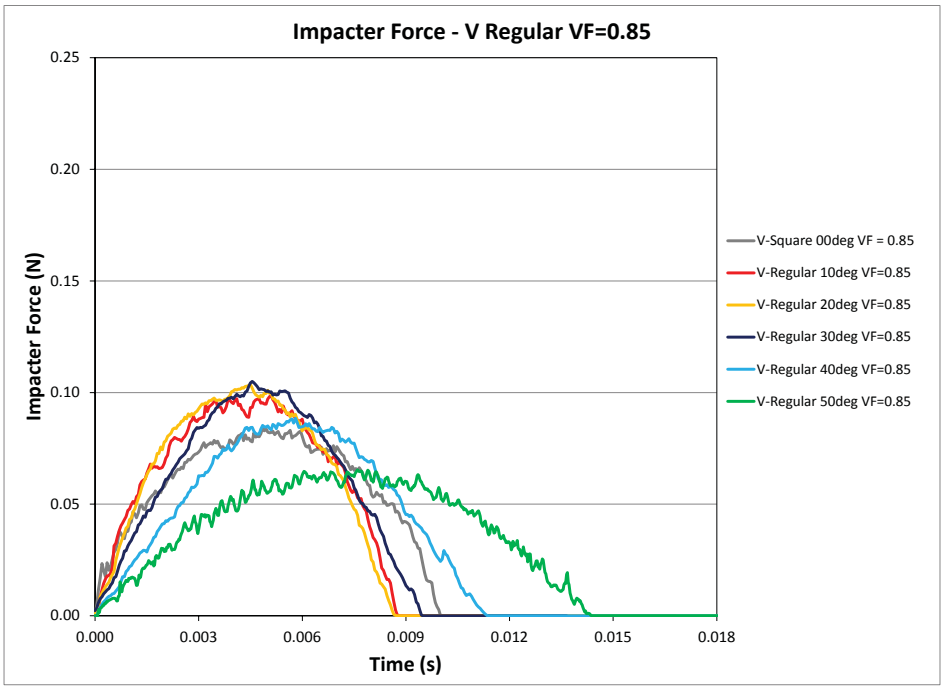

Figure 161: Impact force time histories for vertical impact of a cylindrical impacter of 2m/s on regular honeycomb specimens with void fraction of 0.85 and different angles on a substrate.

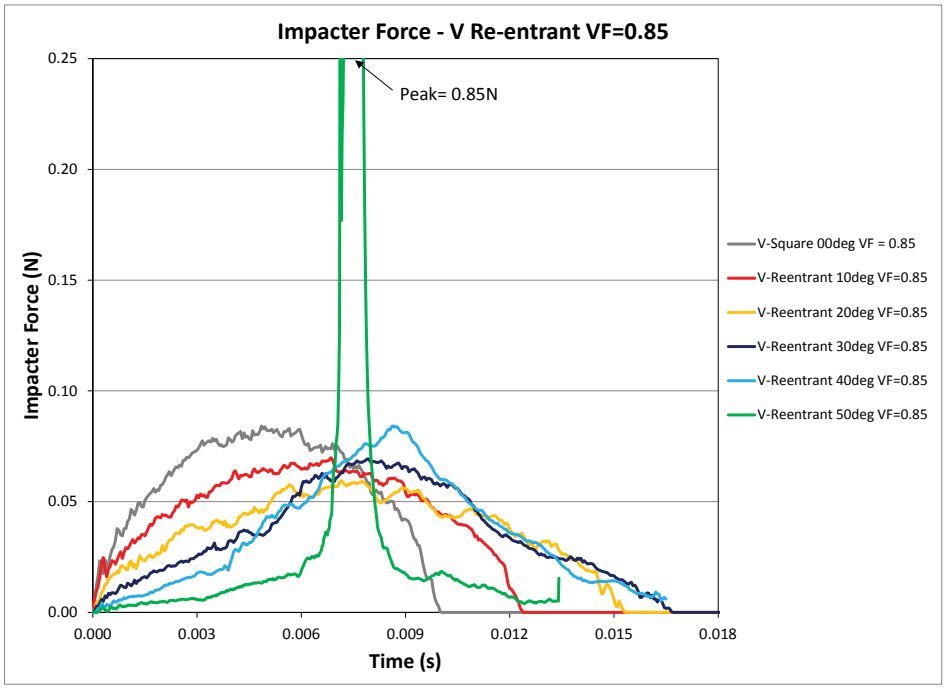

Figure 162: Impact force time histories for vertical impact of a cylindrical impacter of 2m/s on re-entrant honeycomb specimens with void fraction of 0.85 and different angles on a substrate.

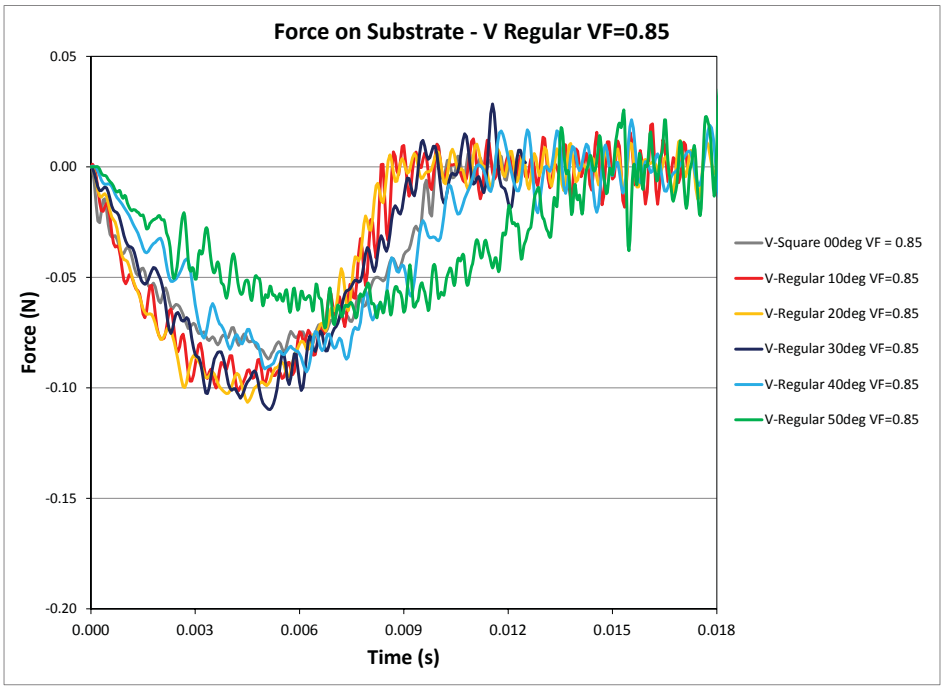

Figure 163: Dynamic force on substrate for vertical impact of a cylindrical impacter of 2m/s on regular honeycomb specimens with void fraction of 0.85 and different angles on a substrate.

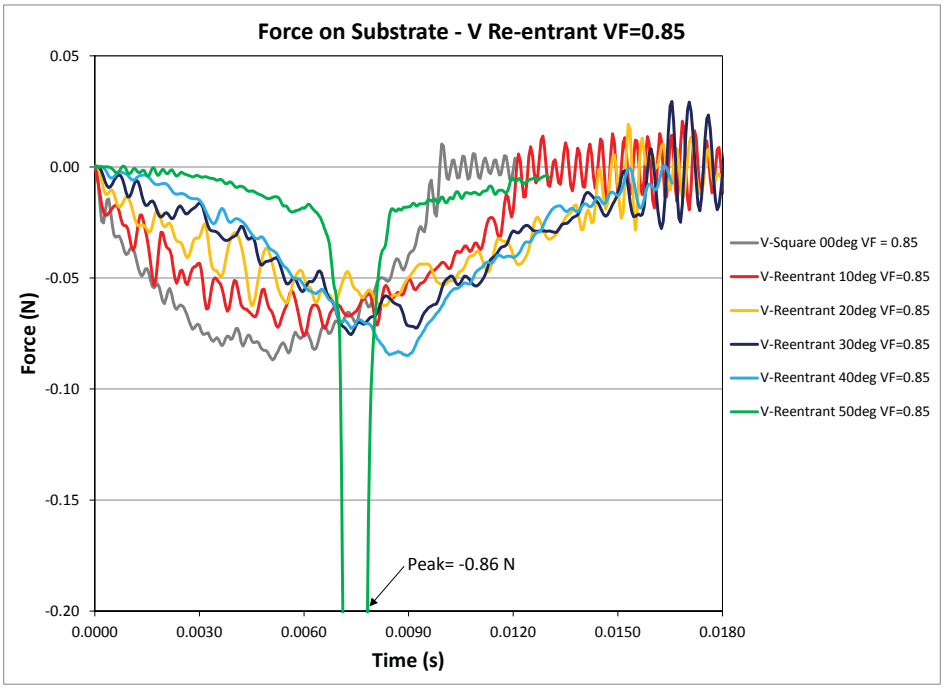

Figure 164: Dynamic force on substrate for vertical impact of a cylindrical impacter of 2m/s on re-entrant honeycomb specimens with void fraction of 0.85 and different angles on a substrate.

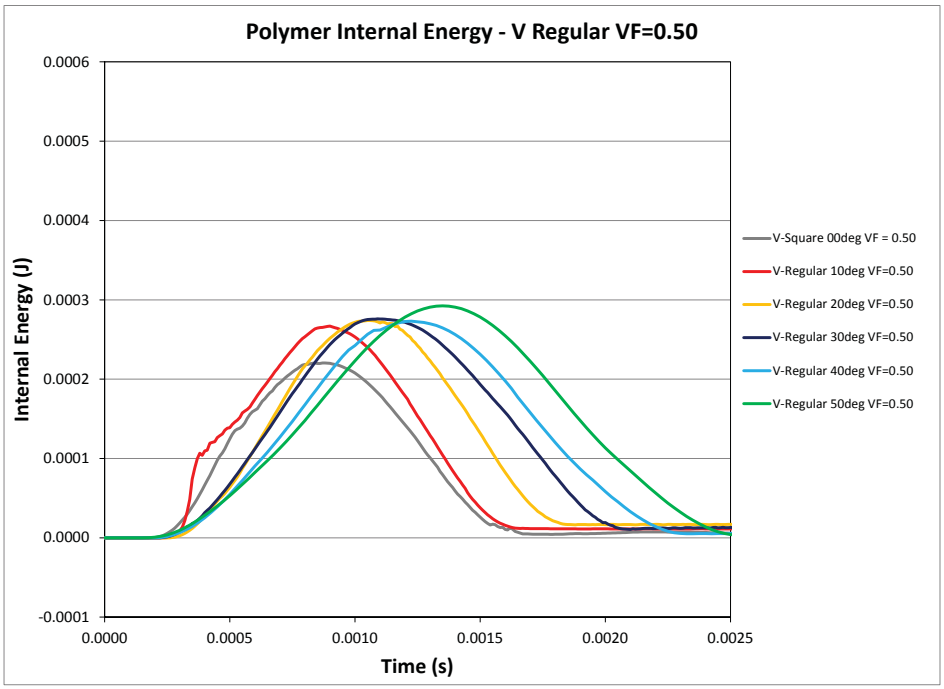

Figure 165: Internal energy time histories for vertical impact of a cylindrical impacter of 2m/s on regular honeycomb specimens with void fraction of 0.5 and different angles on a substrate.

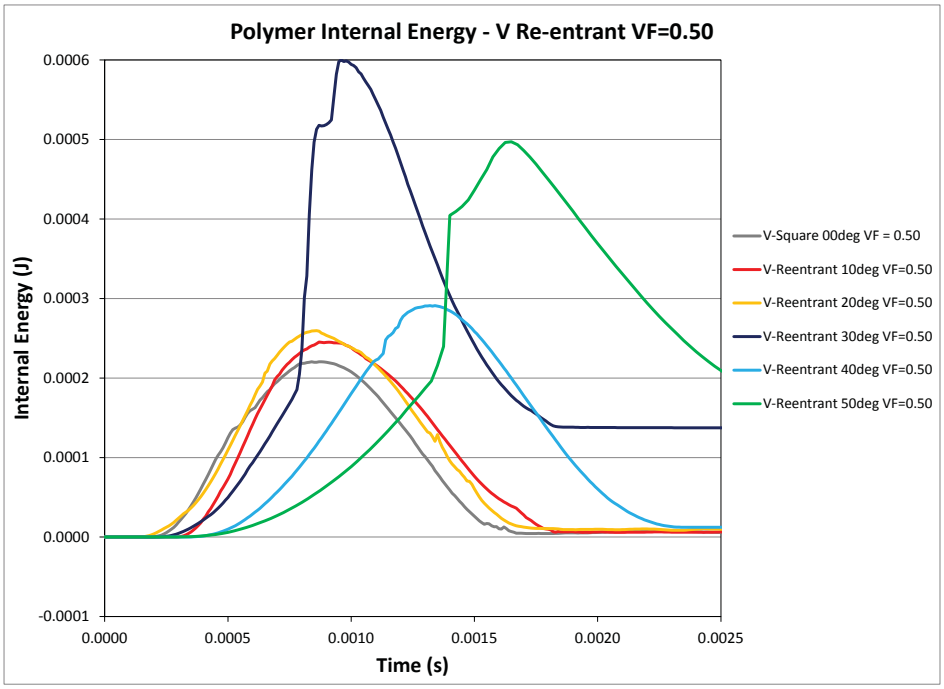

Figure 166: Internal energy time histories for vertical impact of a cylindrical impacter of 2m/s on re-entrant honeycomb specimens with void fraction of 0.5 and different angles on a substrate.

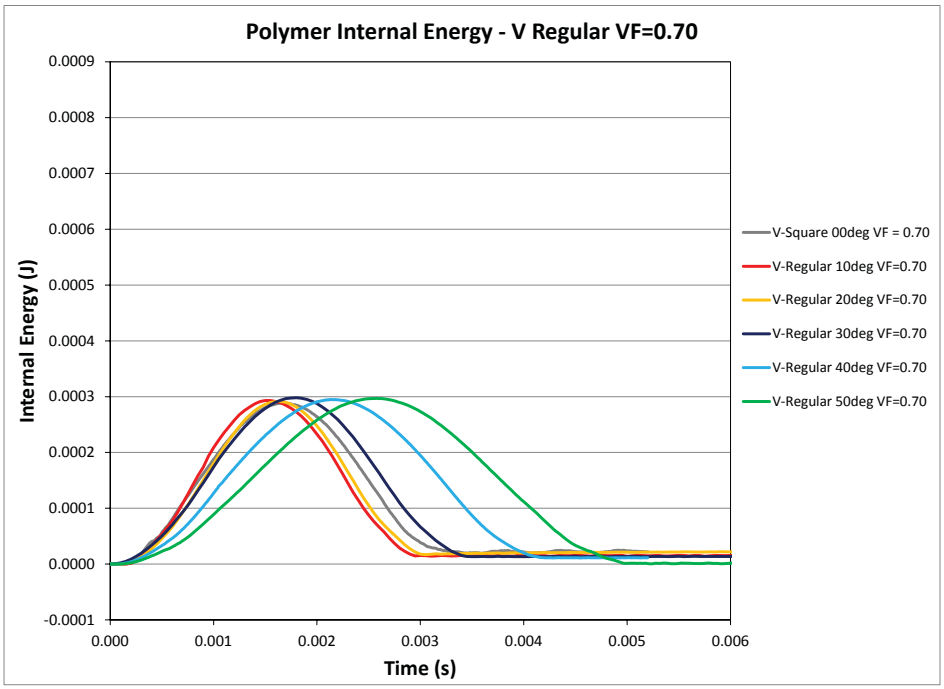

Figure 167: Internal energy time histories for vertical impact of a cylindrical impacter of 2m/s on regular honeycomb specimens with void fraction of 0.7 and different angles on a substrate.

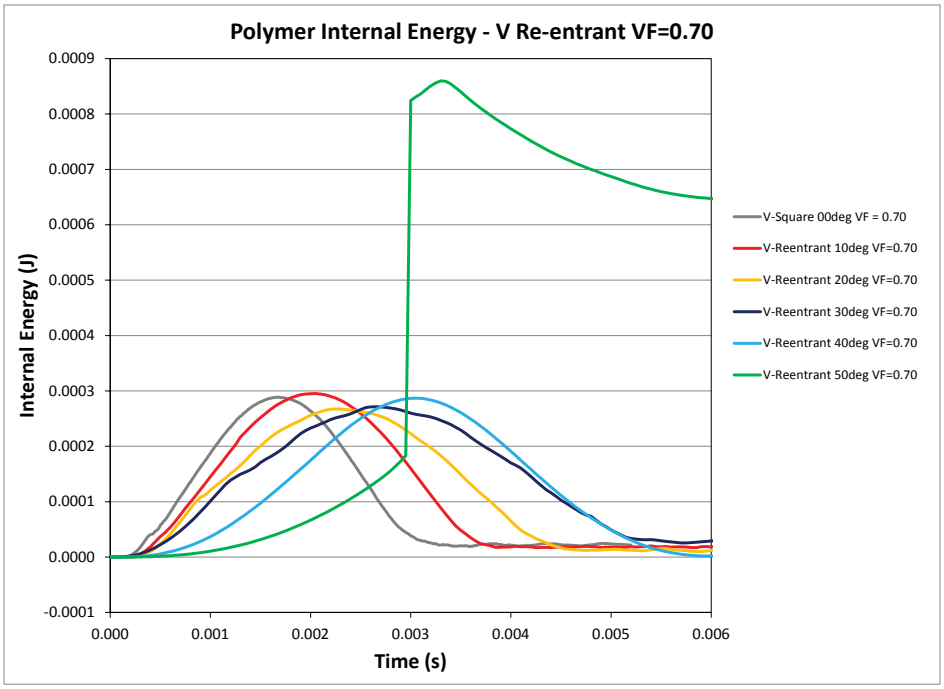

Figure 168: Internal energy time histories for vertical impact of a cylindrical impacter of 2m/s on re-entrant honeycomb specimens with void fraction of 0.7 and different angles on a substrate.

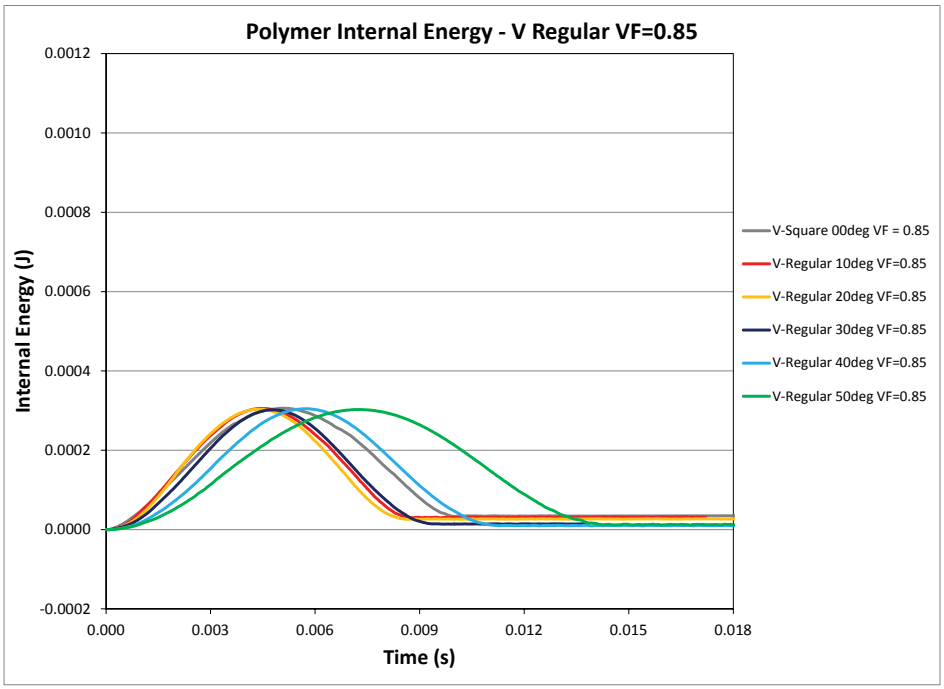

Figure 169: Internal energy time histories for vertical impact of a cylindrical impacter of 2m/s on regular honeycomb specimens with void fraction of 0.85 and different angles on a substrate.

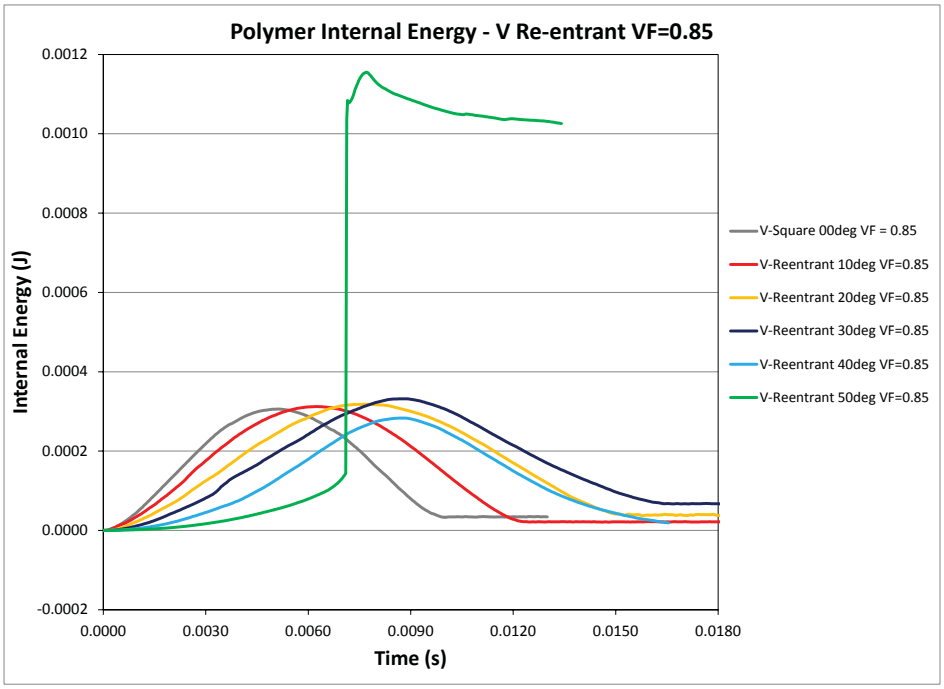

Figure 170: Internal energy time histories for vertical impact of a cylindrical impacter of 2m/s on re-entrant honeycomb specimens with void fraction of 0.55 and different angles on a substrate.

7 Conclusions

In this report, we have described works performed in phase 2 of a recent numerical investigation on impact properties of auxetic materials. Auxetic materials are special materials that have negative Poisson's ratios. This class of materials have received a great deal of attention recently and have been demonstrated to exhibit some unique characteristics that provide advantages over conventional engineering materials for certain applications. The objective of the present study is to investigate the impact properties of the auxetic polymer materials and determine the influence of the geometric parameters associated with the auxetic materials on their protective performance against impact loadings.

In the present phase of the project, the results of a parametric study performed in phase 1 were first verified using a wide variety of numerical techniques. The areas of verifications included the contact algorithms and the element formulations. The former investigation involved repeated solutions of selected test cases using a wide selection of contact algorithms and parameters. This investigation concluded that the *CONTACT_AUTOMATIC_SINGLE_SURFACE option with a reduced penalty stiffness must be utilized to obtain desirable numerical solutions. The later verification was conducted for various test problems, including simple beam and single cell of an auxetic material, and different types of static and dynamic analyses. Through these verifications, a set of solution control parameters, related to shell element formulation, bulk viscosity and solution accuracy, were identified for producing reliable numerical solutions. These verifications also indicated that the rubber-to-rubber friction between the deformed ribs in the auxetic materials had a significant influence on the predicted mechanical behaviour of the materials and need to be included in the numerical solutions. On the other hand, the solid element solutions were found to contain serious hourglass modes and were not suitable for the present analyses.

A total of four parametric studies were performed using the preferred solution control parameters identified through the above verification process. The first parametric study was the same as the one performed in the previous phase of the project, which characterized impacter properties of the auxetic materials up to and beyond the fully compact state. The second parametric study was designed to investigate the impact properties of the materials in their practical deformation range which involved partial compression. This was achieved by using a reduced impact speed which was determined through a separate numerical study.

In both parametric studies described above, the impacter was simulated using a rigid plane, which resulted in nearly uniform deformations in the auxetic material samples. However, in reality, the impacter was normally of finite size and the impact force taken by the material was localized. In order to investigate the material behaviour under local impact, the third parametric study was developed and conducted. Prior to the parametric study, numerical experiments were performed to determine the desired model width, boundary conditions and impact speed. Finally, selected cases from the third parametric study were reanalyzed by including the substrate to the models. In order to permit the total force acting on the substrate be evaluated, the substrate was represented by a rigid mass connected to the sample through multi-point constraints.

Upon the completion of these parametric studies, the deformed configurations for each test case were examined to ensure the stability of the numerical solutions. The impact force time histories were then computed by multiplying the impacter mass and impacter acceleration obtained by

differentiating the displacement time histories. For the last parametric study, the time histories of the total force transmitted to the substrate were obtained by following the same procedure. To reduce the high-frequencies noises in some solutions, data smoothing algorithm has been applied. These results were presented in this report.

The results from all parametric studies showed highly consistent trends on the impact properties of both the conventional and re-entrant material samples and all together, provided a clear picture on the mechanical responses of these materials to impact loading. For instance, all parametric studies indicated that material samples with larger geometric angle θ generated less resistance to the impacter at the beginning of the transient. In addition, for given void fraction and geometric angle θ, the conventional materials provided more resistance to the impacter than the re-entrant materials. Both of these trends were consistent with the effective elastic moduli of the honeycomb structures presented in the phase I report [1].

Under relatively high impact speed, the impact force time histories consistently contained a phase of low impact force and a phase of rapid increase in impact force. The former was dominated by bending deformations in the ribs, whereas the latter occurred when the voids in the materials were being eliminated. This mechanical behaviour was a direct consequence of the nonlinear stress-strain property of typical auxetic materials, which contained distinct low stiffness and high stiffness phases. For impacts at lower speed, use of stiffer materials, such as those with smaller angle θ, would generate sufficient resistance to the impacter, so the material responses would be limited to the low stiffness phase of the stress-strain curve, resulting in smooth impact force time histories. However, for softer materials, such as those with larger angle θ, the low stiffness of the materials was unable to generate sufficient resistance to the impacter to decelerate it effectively, so the material response was pushed into the high stiffness phase in the effective stress-strain curve, causing large peaks in impact force time histories.

Due to the high local strain rates and the rubber-to-rubber friction between the deformed ribs inside the material samples, nearly elastic responses of the material samples were predicted in all parametric studies. This could be confirmed by examining the deformed configurations and the time histories of the internal energy absorbed in the material sample. The former indicated that the material samples almost always recovered its original height after the release of the impacter, whereas the later showed that the internal energy was almost fully released at the end of the impact event. This nearly elastic response was believed to represent the physical mechanical behaviour of the auxetic polymer foams reasonably well.

Finally the last parametric study confirmed that the impact force and the force transmitted to the substrate were of the same magnitudes. This was due to the relatively small inertial effects of the material samples. Because of the equality of the impact force and the force transmitted to the substrate, all the observations made on the impacter force could be readily utilized to determine the optimal auxetic foam for certain applications. For instance, if re-entrant material layers are to be used to protect the substrate from impact damage, material types with large angle θ, such as 50^{O}, should be avoided as these materials generate less resistance at the beginning of the transient which might result in large peak force on the substrate later. On the other hand, if conventional honeycomb materials are to be used as protective layers, materials with larger angles are preferred as they result in lower forces on the substrate, accompanied by longer impact durations. In general, no clear benefits were found on using re-entrant materials as protective layers to reduce impact force in the substrates.

References

[1] Jiang, L., Pearson, D. and MacKay, K. (2013). Modeling of impact properties of auxetic materials, Martec Technical Report TR-13-36, July 2013.

[2] Young W.C. and Budynas, R.G. (2002). Roark's Formulas for Stress and Strain (Seventh Edition), McGraw Hill, New York.

[3] Gibson, L.J., Ashby, M.F., Schajer, G.S. and Robertson, C.I. (1982), The mechanics of two-dimensional cellular materials, Proceedings of the Royal Society of London, A382: 25.

[4] Masters, I. and Evans, K. (1996), Models for the elastic deformation of honeycombs, Composite Structures, 35 (4): 403-422.

[5] http://www.engineeringtoolbox.com/friction-coefficients-d_778.html

[6] Scarpa, F., Ciffo, L. and Yates, J. (2004), Dynamic properties of high structural integrity auxetic open cell foam, Smart Materials and Structures, 13: 49.